UNIVERSITY OF OKLAHOMA

GRADUATE COLLEGE

TOWARDS A BETTER UNDERSTANDING OF THE RELATIONSHIP BETWEEN MOLECULAR FORCE AND HYDROCARBON RECOVERY

A DISSERTATION

SUBMITTED TO THE GRADUATE FACULTY

in partial fulfillment of the requirements for the

Degree of

DOCTOR OF PHILOSOPHY

By

Mohamed Mehana
Norman, Oklahoma
2019

TOWARDS A BETTER UNDERSTANDING OF THE RELATIONSHIP BETWEEN MOLECULAR FORCE AND HYDROCARBON RECOVERY

A DISSERTATION APPROVED FOR THE
MEWBOURNE SCHOOL OF PETROLEUM AND GEOLOGICAL ENGINEERING

BY

Dr. Mashhad Fahes, Chair

Dr. Liangliang Huang, Chair

Dr. Curtis Whitson

Dr. Xingru Wu

Dr. Zulfiquar Reza

Dr. Catalin Teodoriu

Dr. Kurt Marfurt

Dedication

To my family and friends

To all the peaceful souls bringing joy and happiness to the world

Acknowledgements

First and above all, I praise God, Almighty, for providing me this opportunity and granting me the capability to proceed successfully. This dissertation appears in its current form due to the assistance and guidance of several people. I would like to offer my sincere thanks to all of them.

I would like to express my sincere gratitude to my advisors Dr. Mashhad Fahes and Dr. Liangliang Huang for their continuous support and knowledge. Also, I am grateful to my committee members, Dr. Curtis Whitson, Dr. Xingru Wu, Dr. Zulfiguar Reza, Dr. Catalin Teodoriu and Dr. Kurt Marfurt for their encouragement and practical advice.

A very special thanks to my family for their love and support. My parents have always been my biggest fans. I truly appreciate their encouragement throughout my education journey and ingraining the love for education in me. As life marches on and changes on every turn, I am certain that my sister will always be there for me. Thanks to my mom, the most strong and sage woman I have ever met. I owe her a lot.

I am indebted to my friends for providing the support and friendship needed. I was fortunate to taste the true friendship. Special thanks to my childhood friends in my village El-hosseini and Osama; to my college friends Mansi and Ahmed Hassan; to my Oklahoma friends Shams, Rida, Tarek, and to my internships friends Sassan,

Prasanna, Peter, Ye, Minwei and Tomas. Wholehearted thank you goes to Aya for all the help, advice, and laughter.

My deep appreciation goes to Dr. Seyyed Hosseini for his wonderful mentoring during my summer internship at Gulf Carbon Capture Center (GCCC). With his expertise, discipline and patience, he introduced me to a completely new field for me. Also, thanks to Dr. Abbas Firoozabadi for providing an opportunity to intern with Reservoir Engineering Research Institute. His passion for scientific research and immense knowledge are remarkable. Through our interactions, I came to know what it takes to produce worthy research contributions. I also like to extend my sincere gratitude to my academic mentors Dr. Farrokh Mistree, Dr. Janet Allen and Dr. Hussein Hoteit

I want to express my gratitude to Mewbourne School of Petroleum and Geological Engineering family. Most of my theoretical foundations were built here. Special thanks to Dr. Jeffrey Callard for his guidance during our collaboration and for his tips during our tennis matches and training. Also, I would like to thank all the Petroleum Engineering staff for all their help and kindness.

I am also grateful for Society of Petroleum Engineers (SPE) for rewarding me the Nico van Wingen Memorial graduate fellowship. Thank you for your generosity and support. It is a great honor to receive this prestigious fellowship and I hope I will be able to give back to my SPE community. I also want to acknowledge the Petroleum Engineering Department at Suez University for approving my educational vacation to pursue my graduate study and for all the help and support.

All the computations were performed at the OU Supercomputing Center for Education & Research (OSCER) at the University of Oklahoma (OU). I thank the support team for their generous support, extraordinary service, and the wonderful spirit through which they help with the utmost patience and dedication.

The journey was fantastic. I did enjoy all the adventures, meetings and sleepless nights. I do appreciate all the amazing people I came to know, work and learn from them. The journey was "transformational" where I learned priceless life lessons. What I appreciate more, is the opportunity to discover my true values.

Contents

List of Tables

List of Figures

Abstract

The optimization of hydrocarbon recovery is the core of petroleum engineering. Experiments are always the go-to approach to reveal mysterious observations and verify new theories. However, recent advances on our understanding of the matter have led to the development of computational approaches to track the evolution of its microscopic constituents. The microscopic modelling of the matter can be considered to be a computational experiment. These computational experiments are capable of exploring unknown-physics territories and providing validation to to the hypotheses and theories proposed from macroscopic observations. Coupling the complexity of the subsurface reservoirs with the heterogeneity of hydrocarbon systems, molecular simulation finds a fertile field to offer unmatched insights. The goal of this dissertation is to bridge the gap between theoretical research and field applications facilitating physics-based approaches to augment any observed empirical correlations. In our lab, I have noticed some puzzling observations where experiments are not capable of decoupling the competing factors towards explaining the behavior. For this reason, I designed computational microscopic experiments to unravel previous experimental results.

The density behavior of the CO_2/hydrocarbon mixture was my first project. While most of the gases used in the field for Enhanced Oil Recovery (EOR) result in a reduction in density when it mixes with the oil, experiments show that Carbon Dioxide (CO_2) can result in an increase of the density. In addition, field operations

report an early breakthrough for CO_2 flooding, related to gravity segregation due to the abnormal density behavior. However, the molecular interactions that have an impact on the observed macroscopic behavior are poorly understood. I used molecular simulation to study methane, propane and carbon dioxide mixtures with octane, benzene, pentane and hexadecane up to the miscibility limit at temperatures up to 260 °F (400 K), and pressures up to 6000 psi (400 bar). The values of density obtained through molecular simulations validate those obtained through experimental work and Equation of State (EoS) methods. Oil-CO_2 mixtures sustain their density to a higher gas mole percent compared to other gases, with the density in some cases exceeding the pure liquid hydrocarbon density even when gas density at those conditions is lower. Our results have demonstrated that the intermolecular columbic and induced dipole interactions, and the stretching of the alkane molecules, the proposed mechanisms in literature, might not be the key to understand the oil-CO_2 density behavior. However, I find that the molecular size of the gas play an important role in the density profile observed.

Another serious concern for designing a development plan for oil reservoirs is the stability of the asphaltene molecules. I performed molecular simulation to investigate the dynamic behavior of asphaltene during gas flooding, validating the results with experimental observations. I used two structures representing the archipelago and continental types whose aggregation and interactions are studied in methane (C1), propane (C3), carbon dioxide (CO_2), heptane (C7) and toluene as pure solvents, binary mixtures of toluene and either C1, C3 or CO_2, and a representative oil composition. A continental structure is used afterwards to evaluate the impact of temperature, pressure, and resin content on the aggregation dynamics in CO_2 mixtures. Interestingly, the solvating power of CO_2 is dependent on the asphaltene structure where inhibitor-like behavior is observed for continental structure and

precipitator-like behavior is observed for archipelago structure. The solvent quality is highly correlated with the solvent's ability to replace the interactions among asphaltene molecules with interactions between asphaltene and solvent. The aggregate size is reduced by temperature and enhanced by pressure in CO_2. The aggregation of asphaltene is impacted by the physical state of CO_2 as its solvating power to asphaltene is significantly enhanced in its supercritical state.

In another dimension, I investigated Double Layer Expansion (DLE), which is proposed as one of the mechanisms responsible for Improved Oil Recovery (IOR) during Low-Salinity Waterflooding (LSW). I performed molecular simulation to study this phenomenon with both kaolinite and montmorillonite substrates contacting water with a varying concentration of monovalent and divalent ions. My results confirm that the location of the adsorption planes is independent of the ionic strength. However, the electric potential developed on these surfaces and how it decays depends on both the ionic strength and ion nature. A shrinkage is observed in the double layer for the case of low salinity, supported by both film thickness estimations and interaction energy analysis. This shrinkage, which contradicts the prevailing assumption, is consistent with molecular simulation studies reported in the literature, and casts some doubts on the efficiency of double layer expansion as a mechanism for explaining improved oil recovery observed during low-salinity waterflooding. This brings into question the role of double layer expansion in enhancing oil recovery, and raises the need to investigate other mechanisms that could be responsible for the experimental and field observations made in this area.

Chapter 1

Introduction

1.1 Motivations and Objectives

Computational geoscience has provided unmatched insights to the current body of knowledge. Molecular simulation is considered as a computational approach that finds application in geoscience, biology and chemistry. The theoretical foundations is what distinguishes this approach from the other modelling approaches. This theoretical foundations enables molecular simulation to explore unknown physics areas.

Molecular simulation allows inaccessible experimental conditions. These conditions could be high pressure, high temperature or even toxic environment. Another merit is the ability to attribute the observations to the molecular forces and structures. In petroleum engineering, we have several areas where little is known about the underlying physics.

The estimation of the phase equilibrium and properties of the oil mixtures is critical to any successful development plan. This estimation usually requires an experimentation stage to collect the parameters to which the EoS is tuned. This

experimentation stage is constrained by the accessibility of the physical conditions, pressure and temperature, and the uncertainty involved in oil composition estimation. In addition, both EoS performance and applicability depends on the kind of the interactions considered between the mixture constituents. Molecular dynamics (MD) based on computational chemistry provides access to unreachable experimental conditions and serves as a diagnosis tool to decouple the multiple molecular interactions present among the mixtures constituents.

I exploit this feature to study the physical properties of CO_2/oil mixtures where the interaction energy can be decoupled. Experimentally, a slight increase in the CO_2/oil mixture density is observed as the CO_2 concentration increase. This slight increase was conceptually attributed to the coulombic interactions present in CO_2 mixtures. Surprisingly, similar interaction are observed in both CO_2 mixtures and C3 mixtures, both CO_2 and C3 have similar density at the defined conditions. Herein, my initial objective is to evaluate the performance of MD estimations of the mixture density compared to the EoS and experimental data. Then, I investigate the close packing observed in CO_2 mixtures and ascribe this behavior to the molecular structures and forces.

Another area is the deposition of asphaltene which could seriously damage both well and field productivity. The self-assembly could drive the asphaltene molecules to adopt a more ordered configuration which might lead to the aggregation and precipitation of asphaltene molecules. Despite the macroscopic nature of consequences of asphaltene precipitation on the fluid flow and reservoir productivity, the initial cause of this phenomenon needs to be probed microscopically. In addition, the aggregate dimensions and characteristics could be assessed. The asphaltene aggregation is triggered by disturbing the equilibrium through the physical conditions or compositions. Miscible gas flooding operations usually induce compositional changes

which might trigger the asphaltene deposition. My objective is to investigate the aggregation of asphaltene molecules in oil systems experiencing gas flooding and provide a better understanding of the relationship between the morphology of the aggregate and the molecular forces.

Furthermore, I found a contradiction in the literature about one of the proposed mechanisms of Low-Salinity Waterflooding (LSW). Apart from the inconsistent experimental results observed for LSW, I observed a conflict between the impact of the water salinity on the double layer characteristics induced over the mineral surface. Classical thermodynamics predicts a decrease in the thickness of the double layer as the salinity increases. On the other hand, statistical thermodynamics, molecular dynamics, exhibited the opposite. In simple words, the double layer is an imaginary layer induced over the interfaces like solid/brine or brine/oil. The overlap between the double layers induced over those interfaces could lead to the expansion of those layers. This expansion could be translated at the macroscopic scale to a shift in the wettability state of the surface. This mechanism, called double layer expansion, is based on the classical DLVO theory and supported by Zeta potential measurements. At the same time, some concerns have been raised about the efficiency of this mechanism which have received little support from the MD studies. Therefor, my objectives include designing molecular simulation systems to further investigate this mechanism and extracting the exact distribution of the molecular species and the electric field around the interfaces.

1.2 Literature Review

In this section, we present a concise review of the main MD research articles related to my research objectives.

1.2.1 The Density of Carbon dioxide/Oil Mixture

Lansangan and Smith (1993) measured the viscosity, density, and composition of CO_2/West Texas Oil Systems [1]. They observed a monotonic decrease in the viscosity and increase in the density as the CO_2 concentration increased. They attributed this behavior to the coulombic forces experienced in CO_2/oil mixtures.

Ahmed et al. (2012) investigated the complex flow and composition path during CO_2 injection [2]. They upscaled the impact of the unusual density of CO_2/oil mixtures to the reservoir scale where a better recovery factor is observed when this density behavior is considered. In addition, they observed an unstable displacement front. They suggested that the density behavior is due to the coulombic forces enjoyed by CO_2.

Kariznovi et al. (2013) studied the phase composition and saturated liquid properties in binary and ternary systems containing carbon dioxide, n-decane, and n-tetradecane at 323.2 K [3]. They suggested that the increase in the density of CO_2/hydrocarbon mixture is due to coulombic interactions. In addition, they tuned the Equation of State (EoS) binary parameters to experimental data where they found that better liquid density could be predicted when volume translation is employed for both hydrocarbons and CO_2. Nourozieh et al. (2013) used the same methodology. However, their experiments were conducted at 373.2 K [4].

Zhang et al. (2013) used Monte Carlo simulation to study the solubility of CO_2 in octane and the swelling behavior [5]. They employed TraPPE (united) force field for hydrocarbons and EMP2 is used for CO_2. They observed the increase in the CO_2 solubility as the pressure increases and temperature decreases. In addition, the swelling factor is linearly correlated to the CO_2 solubility. In addtion, they suggested that the interactions between CO_2 and octane are the reason behind octane swelling.

Liu et al. (2015) studied the volume swelling of CO_2-alkane systems [6]. They used COMPASS force field where 150 alkane molecules are used to represent the hydrocarbon phase. The alkanes studied include decane, octane, hexane and cyclohexane. They attributed the volume swelling to the CO_2-alkane interactions (dispersion) and the stretching of the alkane molecules in the presence of CO_2. In addition, they observed more swelling for lighter straight alkanes.

1.2.2 Asphaltene Aggregation

Takanohashi et al. (2003) used molecular dynamics to investigate the heat-induced relaxation of asphaltene aggregates [7]. They investigated the stability of three-molecule asphaltene aggregates in vacuum for 100 ps. They observed that aromatic stacking is stable at higher temperature, 673 K, compared to the hydrogen bonding. Besides, they observed that a toy model without the aliphatic chains and heteroatoms would dissociate at lower temperature which lends support to the conclusion that both aliphatic chains and heteroatoms contribute to the aggregate stability.

Takanohashi et al. (2004) studied the structural relaxation behaviors of three different asphaltene structures using MD [8]. They investigated the aggregate stability of each kind. They suggested that the impact of heat and solvent treatment on the stability of the aggregate is different. Whereas the aggregate of one kind sustained its stability at higher temperature compared to the other two, it dissociated relatively at lower temperature compared to the other two when solvent treatment was applied.

Carauta et al. (2004) modeled solvent effects on asphaltene dimers [9]. They studied the aggregation of two asphaltene molecules in toluene, heptane, n-butane

and iso-butane for 100 ps. They reported the minimum distance between the asphaltene molecules which was 3.6 Å in the case of heptane, almost 5 Å in the case of toluene and around 4.5 Å for both isobutene and n-butane. In addition, they observed a decrease in the solubility of asphaltene as the temperature increased.

Mercado et al. (2006) mesoscopically simulated the aggregation of asphaltene and resin molecules in crude oils [10]. They modeled asphaltene as a seven-center molecule, resin as a single sphere and crude oil as a continuum (using Hamaker constant and dielectric constant). In addition, they investigated the impact of temperature, pressure and resin content on the aggregation using Canonical Monte Carlo simulation. Besides, they correlated the aggregation behavior of asphaltene with the refractive index of the medium.

Boek et al. (2008) studied the deposition of asphaltene in capillary flow using both experiments and mesoscopic simulation [11]. They used Stochastic Rotation Dynamics (SRD) where the asphaltene molecules are modelled as colloidal particles and the solvent molecules are modelled as a continuum phase. Observing the pressure drop across the capillary, they suggested that the deposition is initially steady, followed by full local blockage and sharp increase in the pressure. In addition, they observed faster deposition for high flow rates. Besides, they compared simulation results to experimental data where the permeability values obtained from experiment and simulation are matched.

Boek et al. (2009) developed algorithm to generate Quantitative Molecular Representation (QMR) of asphaltene and tested one of the developed structures to perform molecular dynamics [12]. Headen et al. (2009) using QMR structures provided evidence for asphaltene nanoaggregation in toluene and heptane from molecular dynamics simulations [13]. They used QMR procedure to develop one resin and two asphaltene structures. The simulation system contained 6 asphaltene molecules

making up 7 wt.% where OPLS-AA force field was used in a 20-ns-simulation. They observed that asphaltenes do aggregate in toluene and heptane. However, aggregates formed in heptane are long-lived compared to those in toluene. In addition, they estimated the free energy of dimerization in both toluene and heptane which ranges from -6.6 to -12.1 KJ mol^{-1}. Besides, they observed that resin molecules do not aggregate in toluene and slightly aggregate in heptane.

Headen et al. (2011) used molecular dynamics of asphaltene aggregation in supercritical carbon dioxide with and without limonene [14]. They used continental structure to compare the aggregation of asphaltene in supercritical CO_2 to the aggregation in both heptane and toluene. The simulation system contained six asphaltene molecules representing 7 wt.% of the system where EMP2 force field is used for CO_2 and OPLS-AA for asphaltenes in a 20-ns-simulation. They observed a complete and stable aggregation in the case of CO_2. In addition, they reported a nonmonotonic impact for both temperature and pressure on the aggregation of asphaltene. Besides, they observed promising results when 50 wt.% limonene was mixed with supercritical CO_2 where a reduction in the aggregate size is perceived.

Sedghi et al.(2013) investigated the impact of the structure of asphaltene on the aggregation behavior using molecular dynamics [15]. They related the asphaltene structure to the free energy of association which was estimated using the umbrella sampling. They supported the modified Yen model where the proposed aggregation stages are observed (Molecule, Nanoaggregate and Clusters). They observed that the more aromatic rings the asphaltene structure has, the higher the association energy it possesses. In addition, they observed that the hetero-atoms located in the asphaltenes aromatic core are affecting the association energy more than those located on the aliphatic chains.

Jover et al. (2014) discussed the aspects of asphaltene aggregation obtained

from coarse-grained molecular modeling [16]. They developed a coarse grain model using C6 as a bead for both the aromatic and aliphatic constituents to match the liquid density values measured experimentally. In addition, they reproduced the asphaltene solubility behavior in both toluene and heptane.

Wang and Ferguson (2016) simulated asphaltene aggregation at a mesoscale scale [17]. They developed a coarse grain force field by matching the Potential of Mean Force (PMF) curves derived from atomistic simulation. They used the developed model to investigate the aggregation of asphaltene in both toluene and heptane. They supported Yen-Mullins as a conceptual model to describe the growth of asphaltene aggregation and precipitation. In addition, they observed that the longer the aliphatic chain, the harder it is to form nanoaggregate clusters. Besides, they observed that the fractal dimension of the asphaltene is around 2.

Sedghi and Goal (2016) studied the dispersion of asphaltene aggregation by limonene and PVAc polymer during CO_2 flooding [18]. They used two asphaltene structures with and without a hydroxyl group to investigate the effect of hydrogen bonding. Their simulation system contains 200 asphaltene molecules making up 4 wt.%, and is simulated for 80 ns at 308 K and 300 bar. They used TRAPPE force field for CO_2 and OPLS-AA for both asphaltene molecules and the polymers. While limonene by itself could be sufficient to disperse aggregates of asphaltene without hydrogen bonding, 5 wt.% of PVAc must be present for limonene to disperse the aggregates with hydrogen bonding.

Headen et al. (2017) discussed asphaltene aggregation through molecular dynamics where they reported the insights and limitations [19]. They used five different asphaltene structures to investigate the dynamics of asphaltene in heptane and toluene. Their simulation system contains 27 asphaltene molecules which make up 7 wt.% of the system and is simulated for 80 ns at ambient conditions. They reported

a diffuse nature for the asphaltene aggregate with a spherical shape that tends to be prolate for the archipelago structures and oblate for the continental structures. In addition they shed light at the shortcomings of atomistic simulation of the equilibrium properties of the asphaltene aggregate in heptane where they reported a 0.5 μs-simulation run which failed to reach equilibrium.

Yaseen and Mansoori (2017) used molecular dynamics to study the interaction between asphaltenes and solvents [20]. They studied the interaction of a single asphaltene molecule (three different structures) in water and ortho-xylene where they used OPLS_AA force field for asphaltene and SPC/E for water. They reported that pressure has limited impact on the potential energy compared to temperature.

Fang et al. (2017) studied asphaltene precipitation in CO_2 flooding from the molecular dynamics perspective [21]. They investigated the aggregation of asphaltene over a silica surface where CO_2 was observed to extract both non-polar and light hydrocarbons and lead to the formation of the asphaltene aggregate. In addition, they studied the impact of pressure on both the asphaltene aggregation and the adsorption of the aggregate to the silica surface.

1.2.3 Low-salinity Waterflooding

Bourg and Sposito (2011) studied the electric double layer on Smectite surfaces contacting concentrated mixed electrolyte (NaCl-$CaCl_2$) solutions using molecular dynamics [22]. They used Clayff force field for Smectite and SPCE for water. They observed adsorption planes whose location is not affected by neither the ion concertation nor type. In addition, they observed a charge inversion in the diffuse layer, which questions the applicability of Electrostatic Double Layer (EDL) models which assume a monotonic decrease in the charge.

Myint and Firoozabadi (2015) provided a condense literature review of the current knowledge about low-salinity waterflooding in both sandstone and carbonates where they discussed the role of thin liquid films in improved oil recovery from low-salinity brine [23]. They identified the following areas for development: experimental measurement of the water film thickness under different compositions, temperatures and pH values, molecular simulation for the film thermodynamics and disjoining pressure, and finally thermodynamic modelling of both oil/brine and brine/rock interfaces.

Underwood et al. (2015) used molecular dynamic to investigate the impact of salinity on the interactions between montmorillonite and organics to provide a better understanding of the salinity impact on improved oil recovery [24]. They used Clayff force fields for Montmorillonite, CHARMM36 for organics (decane) and TIP3P for water. They investigated Double Layer Expansion (DLE), Multicomponent Ionic Exchange (MIE) and pH effects as possible mechanisms accompanying low-salinity waterflooding. They reported limited impact for DLE, where electric field strength did not vary much with the change in salinity. In addition, they observed bulk behavior beyond 2 nm from the surface. For pH effects, they argued that the change in pH changes could result in protonation of the organics and, subsequently, an increase in the ion bridging and oil wettability. For MIE, the cation bridging is observed only for initially oil-wet clay. In addition, the stern layer cations are not impacted by the bulk solution salinity. Therefore, they suggest that cation bridging is independent of salinity. Moreover, they highlighted the importance of the charge balancing cation on the wettability of clay minerals.

Underwood et al. (2016) studied the wettability and molecular adsorption at hydrated Kaolinite clay mineral surfaces [25]. They used Clayff force field for Kaolinite, CHARMM36 for organics (decane, decanoic acid and decanamine) and TIP3P

for water. They observed that the organic affinity to the kaolinite surfaces depends on the pH and the functional group present in the organics. Meanwhile, both decane and decanoic acid adsorbed to the silicate surface, decanoate ions adsorb to the hydroxyl surface through anion exchange mechanism. On the other hand, for both decanamine and decanamine ions, equal preference for both surfaces is observed. While the mediating interactions are VDW and hydrogen bonds for the neutral molecule, they were ionic for the charged ones.

Jimenez-Angeles and Firoozabadi (2016) investigated the contact angle and interfaces in oil-brine-substrate sytsems [25]. They used Muscovite mica as a substrate over which a cylindrical droplet of model oil (decane) is placed (OPLS-UA is used for organics). They reported a decrease in the contact angle of the oil droplet as the NaCl concentration increases which was consistent with the experimental data available. They observed higher ion adsorption away from the oil droplet compared to the one underneath the droplet. In addition, they presented a monotonic increase in the thickness of the water layer underneath the oil droplet as NaCl concentration increases.

Jimenez-Angeles and Firoozabadi (2016) studied the ability of a thin water layer to tune substrate wettability [26]. They employed the same setup [27] except that they used a complex oil where a surfactant is added to the oil droplet. They observed that the oil contact angle is different than the one observed for the simple oil. While a monotonic decrease in the contact angle of the simple oil is observed as the NaCl bulk concentration increases, a nonmonotonic trend is observed for the complex oil. They correlated this nonmonotonic behavior with both the step increase in the film thickness and the surfactant-ion adsorption. They also concluded that the ion adsorption to the substrate is electrostatically driven. Meanwhile, the surfactant is coordinated with the substrate through hydrogen bonding with intermediate water.

Greathouse et al. (2017) studied the impact of both temperature and salinity on the adsorption of aqueous crude oil components on the basal surfaces of clay minerals [28]. They used Density Functional Theory (DFT) to estimate the binding energy between organics and mineral surfaces and also, to validate the MD results. Minerals include Kaolinite and Pyrophyllite and Na-Montmorillonite modelled using Clayff force field and CVFF for organics. They reported limited impact for temperature on the adsorption of the organics onto the surface. In addition, they observed limited impact for charge on the adsorption of organics to both Montmorillonite and Pyrophyllite. Most organics adsorb to the hydrophobic surface except anionic resin which exhibits preference for the hydrophilic surface where ion pairing is possible.

Tian and Wang (2017) used Molecular dynamics to study ion-tuned wettability in oil/brine/rock systems [29]. They used SPC force field for water, OPLS-AA for organics (decane and decanoic acid) and CHARMM for quartz. In addition, They measured the contact angle of an oil cylinder placed on top of a partially charged quartz substrate. They reported a slight decrease (less than 5°) in the contact angle as KCl concentration decreases (from 1 to 0.05 molar). They compared their data to both the DLVO theory and the experimental data available.

Zeitler et al. (2017) studied the adsorption of resins at Kaolinite edge sites using molecular dynamics simulation, where they investigated the effect of surface deprotonation on the interfacial structure [30]. They used Clayff force field for Kaolinite and CVFF for organics. They observed a higher tendency for organics anions to coordinate with divalent cations Ca^{2+} rather than monovalent ions Na^{+} which supports the MIE mechanism. In addition, they reported limited impact for the ionic strength on the adsorption in the case of Na^{+} where small clusters of the organic anions readily form.

1.3 Molecular Simulation and Petroleum Engineering

The optimization of the hydrocarbon recovery is the core of the petroleum engineering. Given the heterogeneity of the oil composition and the complexity of the porous media, this optimization becomes a challenging task where empirical parameters are usually needed to enhance the accuracy of the models. Subsequently, the universality of the model is traded for accuracy. In addition, the scale involved necessitates a continuum consideration of the matter where the accessible computational resources could manage a numerical simulation of the recovery process. With this in mind, several concerns could be raised about the feasibility of molecular dynamics in petroleum engineering. However, the number of scholarly papers that combine both "molecular dynamics" and "petroleum engineering" have been constantly increasing in the past twenty years as shown in **Figure 1.1**.

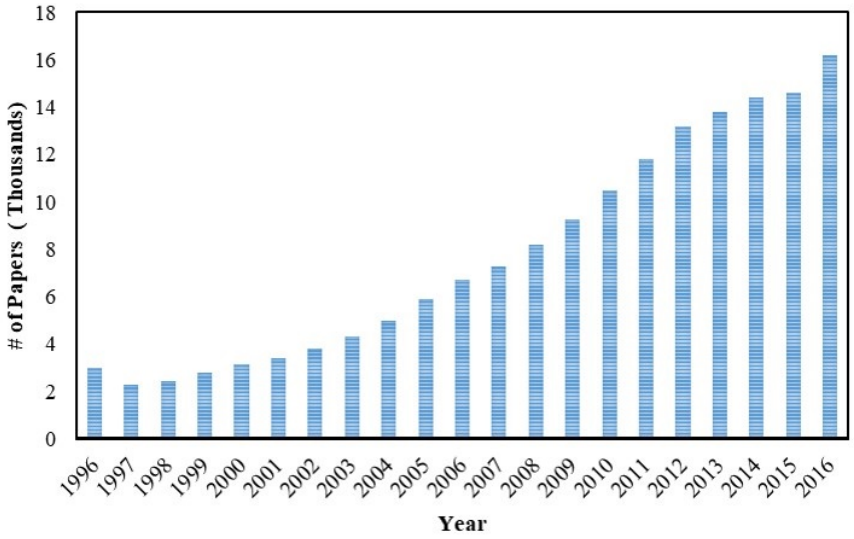

Figure 1.1: The number of the scholarly papers that include Molecular Dynamics and Petroleum Engineering over the past twenty years.

Adding to the areas considered here, several studied have utilized molecular simulation in petroleum engineering where unmatched insights were obtained. Among these, Zhehui and Firooabadi (2013) studied the adsorption of both methane and CO_2 in clay pores [31]. In 2014, they extend their study to evaluate the impact of water presence on the adsorption characteristics [32]. In 2015, they studied the flow of methane in shale pores [33]. In 2016, they investigated the effect of confinement on the phase behavior [34, 35].

Additionally, Hu et al. (2013) studied the dynamics of the slick water using molecular dynamics in a way to reveal the fate of the fracturing fluid [36]. They also extend their simulation to study the water dynamics in kerogen pores in a way to probe the impact of the wettability on the fluid dynamics [37]. In the same vein, Yang et al. (2017) investigated the fast imbibition of orgnics in nanopores. Recently, Li et al. (2017) studied the capillary pressure in the nanopores where they observed a deviation from the macroscopic Young-Laplace relationship [38]. In 2016, Kou and Akkutlu utilized molecular dynmics to estimate the shale permeability. In 2015, Bui and Akkutlu studied the impact of the wall interactions on the surface tension of the methane. These are some of the dimensions where MD could be utilized in petroleum engineering research.

1.4 Thesis Design

Molecular simulation presents itself as a robust tool to investigate some of the challenges encountered in petroleum engineering research. After we have introduced our research objectives and literature review in the current chapter. We structured the rest of the dissertation as follows:

Chapter 2 presents the theoretical foundations of the modelling approach where

an overview of the required inputs and possible outputs. We also presents the softwares used for simulation, analysis and visualization. Finally, we analyze the microscopic observations and how it could be used to derive macroscopic recommendations.

Chapter 3 discusses the impact of molecular forces and structures on the density behavior of CO_2/hydrocarbon mixtures. CO_2 flooding as an Enhanced Oil Recovery (EOR) techniques has several merits that include viscosity reduction, volume swelling and sweep efficiency. However, the density behavior of CO_2/oil mixtures is controversial where slight increase in the mixture density is observed as the concentration of CO_2 increase. This behavior have been attributed to the coulombic interactions present in CO_2 mixtures. This behavior complicates the displacement process where unstable fronts might be induced. We started by investigating how the density of the CO_2 mixture is different from the ideal mixing behavior. Then, we checked the applicability of molecular dynamics to reproduce the density behavior of CO_2 mixture. The impact of CO_2 on the molecular structure of solvent molecules is also reported. After that, we decoupled the density behavior to identify the key factors

Chapter 4 discusses the stability of asphaltene molecules in crude oil. The complexity originates from the heterogeneity of the oil system, the wide-span of operating conditions and the inherited ambiguity associated with the asphaltene molecular structure. The study of asphaltene stability during gas flooding adds another degree of complexity to the challenge. We started by discussing the molecular structures and force fields available in the literature to study the aggregation of asphaltene. Then, we studied the aggregation characteristics of asphaltenes in pure gases and mixtures of toluene and gases. Next, we tried to explain the aggregation in different solvents through the intermolecular interactions at the play. Later, We investigated

the impact of the physical conditions and the resins on the asphaltene dynamics. Finally, we studied the asphaltenes aggregation in a representative oil composition to which we inject similar percentages of methane and CO_2 [39].

Chapter 5 discusses one of the mechanisms associated with Low-salinity waterflooding (LSW). LSW has gained a lot of momentum in the past two decades as a technique lacking fundamental understanding. Consequently, our understanding of the mechanisms associated with the Improved Oil Recovery (IOR) accompanying LSWF has developed. Double layer expansion (DLE) is one of the main proposed mechanisms which have been settled in the petroleum literature. However, recent molecular simulation studies have questioned the efficiency of DLE. In this chapter, we discuss the current understanding of DLE as a mechanism for IOR in LSWF. then, we design a molecular dynamics model to investigate DLE at the molecular level [40].

Chapter 6 summarizes the main finding and provides an outlook for future work.

Chapter 2

Molecular Dynamics

In this chapter, background about molecular simulation and the properties estimated are presented.

2.1 Molecular Simulation

The selection of the modelling scale usually is based on the characteristics of the phenomenon and the computational resources. While sub-sub-nanoscale deals with the interactions between the subatomic particles, the continuum scale treats the matter as a continuous matter ignoring its molecular nature; however, enabling larger time and length scales as presented in **Figure 2.1**. Recently, petroleum engineering developed large interest in the sub-nanoscale, nanoscale and mesoscale approaches. This interest is driven by both the insights provided by these scales and the advances in the computational power. It is worth noting that except for the continuum scale, all other scales do consider the molecular structure of the matter.

We will focus our discussions to the nanoscale approach which is the scale utilized in the dissertation. Molecular simulation (atomistic) relies on the Born-

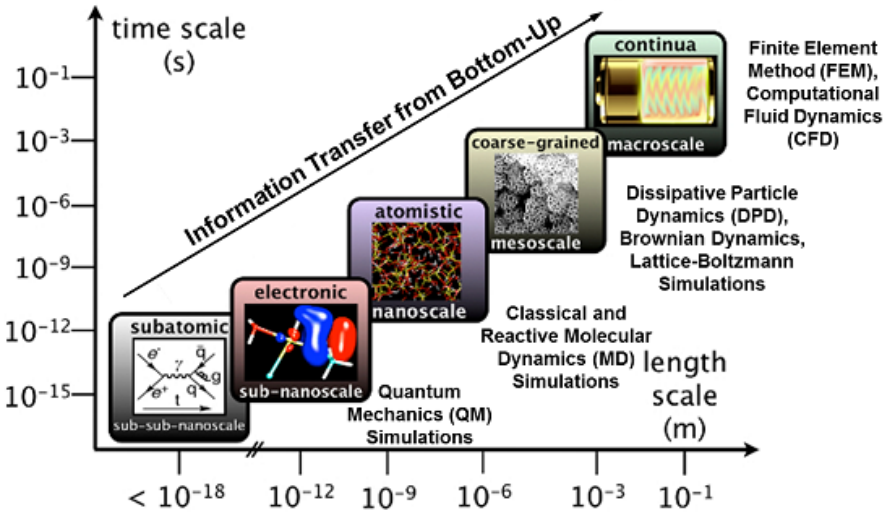

Figure 2.1: Multi-scale framework relating both time and length scale to the simulation scale [41].

Oppenheimer approximation where the electronic and atomic nuclei movements were decoupled. This approximation enabled treating the motion of the atomic nuclei classically, while the effect of electron cloud is explicitly included by partial charges placed on the molecular structure. With the force field parameters describing the intermolecular and intramolecular interactions, the total energy could be estimated. There are two distinct methods of performing molecular simulations: The Molecular Dynamics (MD) approach and the Monte Carlo (MC) approach. While the system evolution in MD simulations is a time dependent process controlled by Newton 's equation of motion, MC simulation is optimized through the Markov chain to achieve more than a 50% acceptance rate for the system configuration states [42].

2.1.1 Molecular Dynamics

Molecular dynamics deals with the dynamics of the atoms whose motion are described classically using Newton 's equations of motion. Given that the force acting

on the atom is the negative derivative of its potential energy, the total potential energy for each atom is updated every time step. Having the initial locations of the atoms, the potential energy could be estimated by summing the molecular interactions. With that, the force acting on the atom could be calculated and, subsequently, its velocity. Then, the new location of the atom could be estimated knowing the old location of atom, velocity and time step.

2.1.2 Force Fields

For potential energy estimation, the molecular interactions among the atoms must be defined through a force field. The force field is a set of equations optimized to reproduce the molecular structure and its properties. For atomistic simulation, the classical force field would include both bonded and non-bonded terms. Whereas the non-bonded parameters describe the intramolecular interactions and include bond, angle, dihedral and improper terms, the bonded interactions describe the intermolecular interactions and include both the Van Der Waals (VDW) and the coulombic interactions as shown in **Figure 2.2**.

In this context, VDW forces is a general term that describes the interactions between uncharged particles. These interactions include a repulsive component arising from Pauli principle, induction component resulting from the interactions of the permanent multipole and the dispersion component which account for the interactions between the instantaneous multipoles. Lennard-Jones potential is one of the widely used potentials in the molecular simulation to describe the interactions between neutral particles. This potential relies on three parameters; ϵ which describes the strength of the interactions and called the depth of the potential well; σ which represents the distance at which the potential is zero and r_m which repre-

sents the distance at which the potential reaches its minimum. Experimental data or quantum chemistry calculations are usually needed to derive those parameters.

On the other hand, the coulombic interactions describe the interactions between charged particles. These interactions would be attractive between identically-charged atoms and repulsive between oppositely-charged particles. They are linearly proportional to the magnitude of the charge and inversely with the distance separating them. In contrast to the VDW interactions, coulombic interactions are long range interactions.

The intramolecular interactions are responsible of maintaining the molecular entity of the structure. They include the bond interactions between two atoms, the angle interactions between three atoms and dihedral interactions between four atoms. Bond and angle potential are usually modelled through the harmonic potential where r_o is the equilibrium distance, θ_0 is the equilibrium angle, k_b is the bond coefficient and k_a is the angle coefficient. On the other hand, dihedral potential could be modelled through opls potential where k_ϕ is the dihedral coefficient and the ϕ is the phase angle.

It is worth noting that force field development is one of the active research topics in computational chemistry science which results in the introduction of reactive force fields [43] and polarizable force fields [44, 45]. The force calculation is considered the heart of the molecular dynamics and usually takes up most of the simulation time.

Over the course of this study, I have used all-atom and united atom force fields. All-atom force fields use all atoms present in the molecular structure as interaction sites with both bonded and non-bonded parameters. On the other hand, united atom force fields lump few interaction sites to a united site where the force field parameters are tuned to properly model the molecular structure and the molecular

interactions. While united atom force fields are more computational efficient, they overlook molecular details that in some cases might be indisputable. Both Transferable Potentials for Phase Equilibria (TraPPE) [46, 47], Optimized Potentials for Liquid Simulations (OPLS) [48] have a united atom and all-atom versions. However, both GROningen MOlecular Simulation (GROMOS 54A7) [49], Clayff [50] are considered all-atom force fields. In addition, several models have been proposed for the water where the model applicability is determined by the phenomenon in question. These models include SPC, SPCE and TIP3P [51, 52].

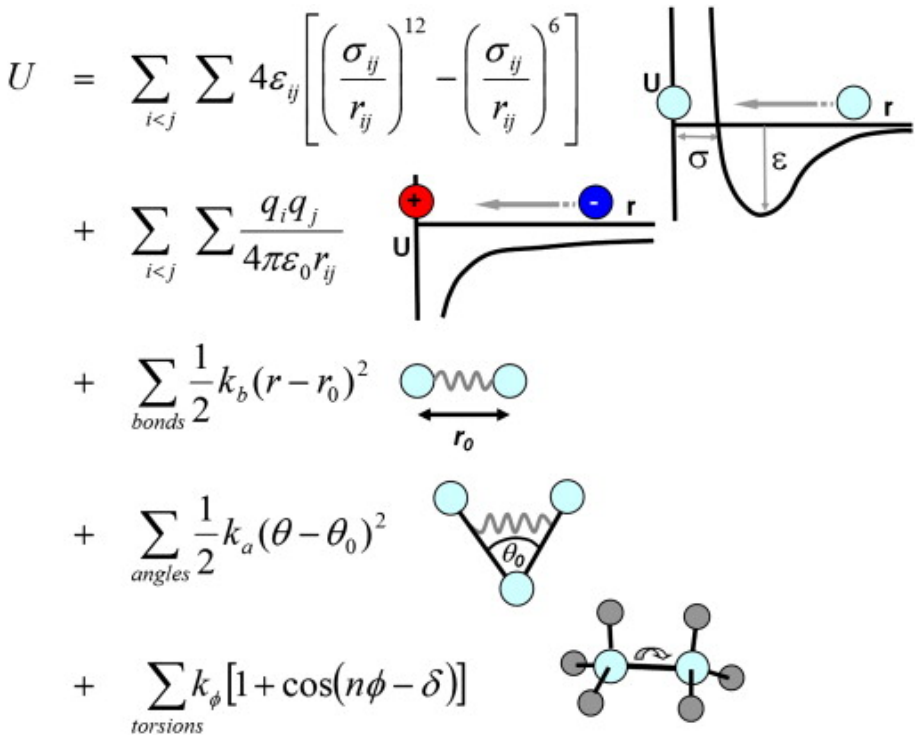

Figure 2.2: Classic force field equations [53].

The estimation of atomic interactions needs 0.5N(N-1) force calculations where N is the number of the atoms in the system. However, given the nature of interatomic forces which significantly decrease with distance between atoms, VDW for instance, constraining the interatomic forces to a cut-off distances could be warranted. This

truncation could be implemented by simply truncating the potential at a certain distance, shifting the potential so that it would be zero at a certain distance, or introducing a transition zone at which the potential would smoothly shift to zero at the cut-off.

With the truncation of the potential, there is no need to estimate the interactions outside the cut-off radius. Therefore, neighbor lists are constructed having only the atoms that are within the cut-off radius. With the neighbor list updated occasionally and the pair interactions constrained to the atoms in the neighbour list, the number of calculation required would decrease by a factor of N. Verlet lists and linked lists with cellular division are the kinds of neighbor lists proposed in the literature.

The correction for the contribution of long range interactions depends on the nature of these interactions. For interactions that phase out quickly like VDW, the correction could be estimated assuming that the distribution beyond the cut-off value is uniform. However, for long range interactions like coulombic interactions, special methods are required to estimate the corrections. These methods include the well-known Ewald summation, Fast Multipole and Particle Cell methods.

2.1.3 Simulation Ensembles

The ensemble represents the state variables that are constrained during the simulation. These state variables include the number of molecules, temperature, pressure, volume and energy. The combination of any two of these variables, in addition to the number of molecules, constitute a simulation ensemble. These ensembles include the canonical ensemble (NVT) where system temperature, volume and number of molecules are kept constant and isobaric isothermal ensemble (NPT) where the system temperature, pressure and number of molecules are kept constant.

The basic MD ensemble is constant energy (nVE). However, natural phenomena require controlling the physical conditions of the system (temperature and pressure). This control could be preformed using either stochastic, strong-coupling, weak-coupling methods or extended system dynamics. While stochastic methods directly constrain a system parameter to a specified value, both strong- and weak-coupling involve scaling a system parameter, extended system dynamics consider the state variables as degrees of freedom. Both strong- and weak-coupling are the commonly used approaches to control the system variables. Whereas Strong-coupling scales the system variable to obtain an exact value, weak-coupling only scale the system variable in the direction of the required value.

Several thermostats and barostats are proposed in the literature. Whereas thermostats scale velocity, barostats scale dimension. Nose-Hoover thermostat is a week-coupling thermostat where a heat bath is introduced to scale the velocity [54]. Whereas Berendsen thermostat and barostat are strong-coupling methods [55], Nose-Hoover thermostat [54] and Parinello-Rahman barostat [56] are weak-coupling methods. It worth noting that weak-coupling methods are more suitable for equilibrium simulation and strong-coupling methods enjoy faster and smoother approach to the equilibrium [57].

2.1.4 Simulation Algorithm

Verlet algorithm is one of the most common algorithms used in molecular dynamics. This algorithm starts with calculating the force acting on an atom through the negative derivative of the potential energy. According to Equation (2.1) (Newton 's second law of motion), the force equals to the mass of the atom multiplied by the acceleration. Employing the Taylor expansion, the positions of the atoms are

estimated at both t + Δt and t - Δt times. Summing both Equation (2.2) and (2.3), the new position could be estimated as a function of the old and current location and the acceleration according to Eq. (2.4). After that, the velocity of the atoms is estimated based on the old and new locations and the time step according to Eq. (2.5). The steps of the Verlet algorithm are presented in **Figure 2.3**. It is worth noting that other algorithms like leap-frog and velocity Verlet have been proposed. For the avid readers about molecular simulation algorithms, we refer them to the book by Frenkel and Smith (chapter 4 and appendix E and J) [58].

$$f_i = m_i \frac{\partial^2 r_i}{\partial t^2} = -\left(\frac{\partial U(r_1, r_2, ...r_N)}{\partial r_i}\right) \tag{2.1}$$

$$r(t+\Delta) = r(t) + \Delta v(t) + \frac{1}{2}(\Delta t)^2 a(t) + ... \tag{2.2}$$

$$r(t-\Delta t) = r(t) - \Delta v(t) + \frac{1}{2}(\Delta t)^2 a(t) - ... \tag{2.3}$$

$$r(t+\Delta) = 2r(t) - r(t-\Delta t) + (\Delta t)^2 a(t) \tag{2.4}$$

$$v(t) = \left(\frac{1}{2\Delta t}\right)[r(t+\Delta t) - r(t-\Delta t)] \tag{2.5}$$

Where for the i-th particle, m_i is the mass, r_i presents the coordinates, f_i is the force, v is the velocity and a is the acceleration.

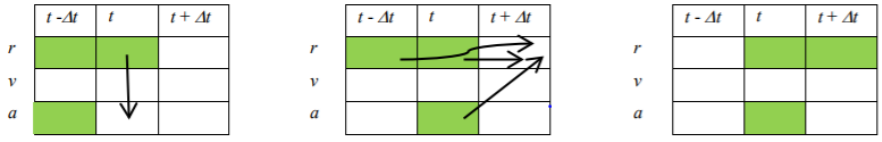

Figure 2.3: Verlet algorithm for updating the atomic positions and velocities [59].

2.1.5 Boundary Conditions

The edge effect is mitigated by utilizing a Periodic Boundary Condition (PBC). The periodic conditions eliminate the surfaces inside the simulation box and allow deriving bulk properties from a system with a finite size (hundreds of molecules). PBC is constructed by repeating the simulation box in all directions so that the atoms crossing a boundary, enter back from the opposite boundary as shown in **Figure 2.3**. However, in this case, the minimum image convention must be employed, i.e., a given particle interacts with another particle only once (either the particle itself or its image). Note that it is not allowed for any particle to travel more than twice the system size during the time step. This situation could raise from bad dynamics during the initialization of the system and/or overlapping of atomic positions.

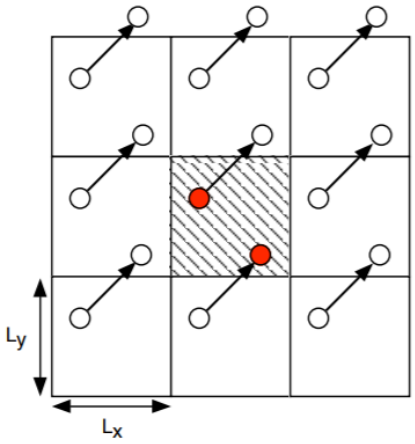

Figure 2.4: Schematic presenting the periodic boundary conditions with imaginary cell repeats and a change in the representative atom as it crosses the boundary [60].

2.1.6 Software Packages

Molecular dynamics codes are the engine that perform the simulation. However, these codes require initial atomic positions to output the time-evolution of atoms

trajectory. Therefore, pre- and post-analysis packages are required to prepare the system, construct the molecular structure and turn the output trajectory into thermodynamic properties and visualization states. There are several open-source codes that have been developed and optimized to perform molecular dynamics. Among these, Large-scale Atomic/Molecular Massively Parallel Simulator (LAMMPS) [61] and GROningen MAchine for Chemical Simulations (GROMACS) [62] are the most commonly used softwares. The molecular structure could be constructed using Avogadro package [63]. In addition, the simulation system could be constructed using Packmol package which allows random placement of the molecules in the simulation system. For visualization, both Open Visualization TOol (OVITO)[64] and Visual Molecular Dynamics (VMD)[65] could be used to both visualize the system evolution and prepare snap shots.

2.2 Simulation Outputs

Through the time-evolution of the system, various non-equilibrium and equilibrium properties could be derived. The simulation time and length for molecular dynamics are at the Nano-scale. However, the ergodic nature of the system, where both the ensemble average and the time average are equivalent, warrants the derivation of macroscopic properties from microscopic simulation. Some of these properties used in this work are described in this section.

2.2.1 Radial Distribution Function

The radial distribution function, or the correlation function, is one of the main tools used in molecular simulation to diagnose the structure of the system. It presents the relative density of atoms as a function of distance where the local density within a

given radius is normalized by the average density of the system. It should converge to unity at longer distances for both liquids and gases as shown in **Figure 2.5**.

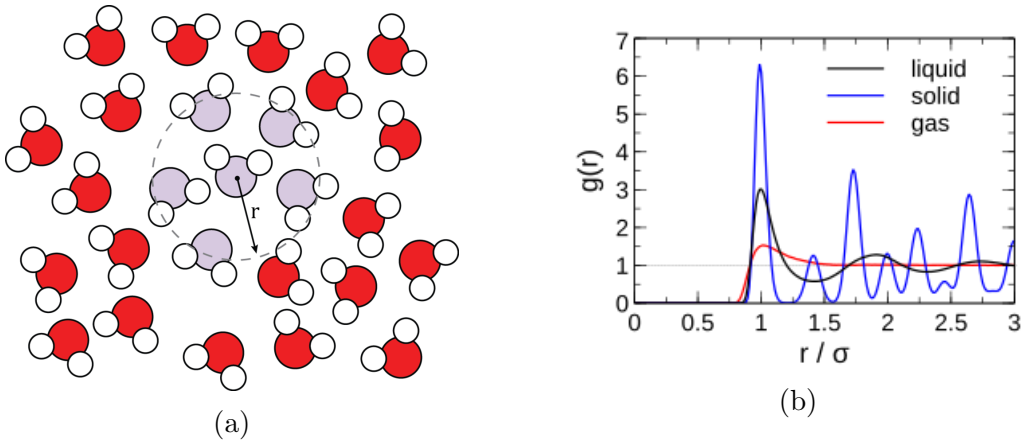

(a) (b)

Figure 2.5: RDF calculation: a) the schematic representation of RDF calculation b) typical example for RDF in liquids [66].

2.2.2 Density

The density of the system is the mass of a unit volume which is usually estimated according to Equation (2.6).

$$\rho = \frac{N_m M}{N_A V} \tag{2.6}$$

Where the N_m is number of the molecules in the system, M is the molecular weight of the molecule, N_A is Avogadro 's number and V is the system volume.

2.2.3 Viscosity

The viscosity is a fluid property which quantifies the ability of the fluid to oppose its motion or the motion inside it. Macroscopically, it could be quantified by the drag force experienced by a moving plate separated from a stationary plate by a

layer of the fluid according to Equation (2.7).

$$\tau = \frac{F}{A} = \eta \frac{A.u}{h} \tag{2.7}$$

Where τ is the shear stress, F is the drag force, A is the surface area of the moving plate, u is the speed of the moving plate, h is the distance between the plates and η is the fluid viscosity.

In molecular simulation, viscosity could be estimated using the Green-Kubo formalization (Equation (2.8)) or Einstein-Helfand relations.

$$\eta = \frac{V}{K_B T} \int_0^\infty \langle P_\alpha \beta(t) . P_\alpha \beta(0) \rangle dt \tag{2.8}$$

Where V is the system volume, K_B is the Boltzmann constant, T in the Temperature and $P_{\alpha\beta}$ is the off-diagonal term of the stress tensor.

2.2.4 Aggregation Number

The average aggregation number is a parameter used to describe the aggregate size. A molecule could be considered as a part of the aggregate if the distance between the molecule and aggregate is less than a defined cutoff.

The size of the aggregate could be estimated experimentally using Nuclear Magnetic Resonance (NMR) [67], Direct-Current Electric Conductivity(DC) [68], Small-Angle Neutron Scattering (SANS) [69, 70] and Small-Angle X-ray Scattering (SAXS) [69, 71]. Aggregation numbers measured using both SANS and SAXS, have a larger and a wider range compared to the values obtained by both NMR and DC methods [19].

2.2.5 Radius of Gyration

The Radius of gyration (R_G) represents a shape-independent measure of the aggregate size. It could be estimated using the gyration tensor where it equals the square root of the summation of the principal moments according to Equation (2.9).

$$R_G = \sqrt{\lambda_x^2 + \lambda_y^2 + \lambda_z^2} \tag{2.9}$$

Where λ_x, λ_y and λ_z are the principal moments and the Eigen values of the gyration tensor. In addition, the ratios (Equation (2.10) and (2.11)) of the Eigen values could be used to describe the sphericity of the aggregate where $\lambda_x > \lambda_y > \lambda_z$.

$$r_1 = \frac{\lambda_x}{\lambda_y} \tag{2.10}$$

$$r_2 = \frac{\lambda_y}{\lambda_z} \tag{2.11}$$

Whereas an aggregate with $r_1 = r_2 = 1$ would have a spherical shape, aggregates with $r_1 = 1$ tend to have an oblate shape and those with $r_2 = 1$ tend to have a prolate shape. In addition, R_G could be measured experimentally using SANS where values between 3.7 and 7.7 nm are observed [72].

2.2.6 Interaction Energy

The interaction energy represents the non-bonded interactions, which include both the VDW and coulombic forces. This energy could be decoupled to diagnose the interactions between the system constituents.

2.2.7 Charge Distribution

The charge distribution is estimated by discretization of the system into small bins, then summing all the charges present in that bin. These charges include both the charges present on the charged ions and the partial charges present on the neutral molecules. The charge distribution calculation is performed to quantify the disturbance induced to an aqueous solution near a surface as shown in chapter 5. Also, the charge distribution is used to estimate both the electric field and potential according to the Poisson-Boltzmann equation which in one dimension has the form presented in Equation (2.12).

$$\Delta^2 = \frac{\partial^2 \psi}{\partial x} = \frac{-\rho_e}{\epsilon_r \epsilon_0} \tag{2.12}$$

Where ψ is the electric potential, ρ_e is the local charge density, ϵ_r is the relative permittivity and ϵ_0 is the permittivity of the free space.

2.2.8 Electric Field

Charged particles induce electric fields which could be estimated by integrating the charge distribution near them as shown in Equation (2.13). Microscopically, the water contribution to the electric field is usually considered using a dielectric constant which results in a monotonic decay of the electric field away from the charged surface. However, microscopically, when the water contribution is considered explicitly, an oscillatory behavior, representing the layering of the water molecules near the charged surface, is observed. This observation is further discussed in chapter 5 where the electric field near the clay minerals surface is estimated.

$$E(x) = \frac{1}{\epsilon_0} \int_0^x \rho_e(x) dx \tag{2.13}$$

Where ψ is the electric potential (V), ρ_e (C/m^3) is the local charge density, ϵ_r is the relative permittivity and ϵ_0 (8.85×10^{-12} F/m) is the permittivity of the free space.

2.2.9 Electric Potential

The electric field is accompanied with an electric potential which is estimated by integrating the electric field or double integrating the charge distribution as shown in Equation (2.14).

$$\psi(x) = -\int_0^x e(x) = -\frac{1}{\epsilon_0}\int_0^x \rho_e(x).(x - x')dx \tag{2.14}$$

Chapter 3

The Density of Oil/Gas Mixtures

3.1 Introduction

Molecular simulation was introduced to the petroleum industry in the early 1990s as a physics-based computational chemistry approach. With the capabilities of this approach, the heterogeneous oil composition was studied at the molecular level at unreachable experimental conditions of pressure and temperature. Karaborni et al. studied the oil solubilization of surfactant solutions [73]. Van Buuren et al. studied the structure of water and decane molecules at their interface [74]. The adsorption of hydrocarbons in silicate was the focus of Dumont and Bougeard [75]. Ungerer et al. proposed a pseudo ensemble to estimate the bubble point while imposing the liquid composition, temperature and global volume [76].

The shale boom started with economical hydrocarbon production from the nanopores [77, 78, 79]. This boom raised lots of questions concerning the physics of fluid transport [80, 81], the phase definition under confinement at the Nano-scale [82, 83], and the geochemical phenomena associated with the choice of fracturing fluid composition [84, 85]. With limited physical experimental approaches to in-

vestigate these phenomena, molecular simulation came to the scene with insights ranging from validating capillary condensation in nanopores and kerogen maturation calculations [86] to investigating the fate of the fracturing fluid [87, 88]. Ungerer et al. discussed the capability of molecular simulation to estimate the phase equilibria and properties for pure hydrocarbons along with their derivative properties [89]. Ungerer et al. comprehensively categorized the main applications of molecular simulation in petroleum engineering to phase equilibria estimation, adsorption kinetics and transport properties [90].

As a thermodynamics model relating the state variables of the system and describing the system energy, the Equation of State (EoS) was developed in order to address a variety of applications. These state variables are the partial derivatives of system energy. Using this equation, the ideal system phase equilibria and properties could be calculated (ideal gas law). However, the non-ideality of the real system requires the introduction of component-dependent parameters where the universality was traded for accuracy. Van der Waals proposed his equation with two substance-specific parameters accounting for both the molecular volume and the physical intermolecular forces in 1873 [91]. Since then, various versions of equations of state have been proposed. With the cubic ones recognized as computation-efficient and accuracy-feasible, they became the most commonly used in the petroleum industry [92]. With the association energy considered, the cubic plus association equation was developed with one more substance-specific parameter [93]. With two additional substance-specific parameters, the PC-SAFT took into account the non-spherical nature of the molecules [94].

Despite the theoretical foundations for the equations of state, they are not a stand-alone approach for estimating system properties. Considering the cubic equation of state, both the binary interaction coefficients and the mixing rules for the un-

like components need to be fitted to the experimental data provided all the specific-substance parameters are available [95].

Carbon dioxide has gained negative attention in the recent decades as a greenhouse gas affecting global warming. Several active research groups are studying carbon dioxide sequestration prospects, and others are investigating its potential for enhanced oil recovery operations [96, 97, 98, 99]. Lansangan and Smith reported an increase in the density at constant temperature and pressure with the increase in carbon dioxide concentration [1]. This experimental finding explained the early CO_2 breakthrough reported by Johnston [100]. They attributed this increase to the columbic forces between the CO_2 molecules and the induced dipoles in oil molecules which resulted in a condensed phase.

The main gases used for EOR are carbon dioxide, nitrogen and methane. Various studies have reported the superiority of carbon dioxide over other gases in terms of the recovery factor [101]. However, the resulting density after mixing carbon dioxide with oil is usually higher compared to other gases. These density variations across the reservoir might induce a non-uniform displacement front due to gravity segregation. Various studies reported the impact of this segregation on oil recovery [2, 101].

These macroscopic experimental results were the focus of several molecular simulation studies. Zhang at al. used Monte Carlo simulation to study CO_2 solubility in octane and reported its impact on the density and swelling factors [5]. However, their density increase was attributed to the increase in pressure. The osmotic ensemble used is not suitable to study the increase in the density at a constant pressure and temperature. The impact of the structure of alkane molecules on the swelling factor of the CO_2-alkane systems was the focus of Liu et al.[6]. They used decane, octane, hexane and cyclohexane where both the chain length and structure were

studied. Their key findings are that the dispersion forces and the stretching of the alkane molecules are the main factors controlling the swelling behavior and in turn the density of the mixture.

In this chapter, we investigate the variation in density for CO_2-hydrocarbon systems and we compare this behavior to other gas-hydrocarbon systems. The rest of this chapter is organized as follows: the simulation approach section discusses the basics of molecular simulation and simulation details, results are presented on a comparison between EoS and MD results, a discussion follows on the key parameters influencing the density behavior of various mixtures and then conclusions summarizing the main findings from this work are outlined.

3.2 Simulation Approach

3.2.1 Molecular Simulation

Molecular simulation relies on the Born-Oppenheimer approximation where the electronic and atomic nuclei movements was decoupled. This approximation enabled treating the motion of the atomic nuclei classically, while the electron cloud effect was explicitly represented by partial charges on the molecule structure. With the force field parameters describing the intermolecular and intramolecular interactions, the total energy could be estimated. There are two distinct methods of performing molecular simulations. The Molecular Dynamics (MD) approach and the Monte Carlo (MC) approach. While the system evolution in MD simulations is a time dependent process controlled by Newton 's equation of motion, MC simulation is optimized through the Markov chain to achieve more than a 50 % acceptance rate for the system configuration states [42].

MD is the simulation method adapted in this work. Through time evolution of the system, various non-equilibrium and equilibrium properties could be derived. The simulation time and length for molecular dynamics are at the Nano-scale. The ergodic nature of the simulation system, where both the ensemble average and the time average are equivalent, is the basis for deriving the macroscopic properties from microscopic simulation. The edge effect is mitigated by utilizing a periodic boundary condition.

3.2.2 Simulation Details

The Large-scale Atomic/Molecular Massively Parallel Simulator (LAMMPS) was used to perform the MD simulations [61]. System setup starts with random placement of a thousand-octane molecule followed by the corresponding number of the solute molecules. The simulation runs for 2 ns with 1 fs as time step where the first ns was disregarded from estimating the equilibrium properties. Isothermal Isobaric ensemble is used where 12 Å is used as a cut-off for Leonard Jones (LJ) and 15 Å for coulombic interactions. While LJ interactions are shifted smoothly to zero at the cut-off, long rang coulombic interactions are treated through the Ewald summation. The total potential energy of the system was estimated using Eq. 3.1, where bonded energy represents the intramolecular interactions and the non-bonded energy represents the intermolecular ones. The intramolecular interactions are the interactions within the molecule and include the interactions due to the bond, angle and torsion. The intermolecular interactions are the interactions among different molecules and include both the Van der Waals and coulombic interactions. The van der Waals interactions are modelled using pair wise-additive Lenard Jones (LJ) $12-6$ potential where ϵ_{ij} and σ_{ij} are the LJ well depth and LJ radius respectively. Cross

interactions are estimated using Lorentz-Berthelot combination rule. The coulombic interactions correction is estimated through the Ewald Summation [102] where q_i and q_j are the partial charges, ϵ_0 is the dielectric constant of the medium and r_{ij} is the separation. Optimized Potentials for Liquid Simulations (OPLS) force field parameters are utilized for hydrocarbon molecules[103] and a flexible force field was used for CO_2 [104]. The detailed parameters are presented in Table 3.1. System equilibrium was achieved for all the systems studied where the system energy and properties are monitored with time. The simulation was performed for 2 ns with a 1 fs time step. The volume of the simulation box was not constrained. The number of gas molecules, referred to as the solute, is estimated for a given mole percentage considering that the number of heavy hydrocarbon molecules, referred to as the solvent, is at 1000 for all the systems simulated. **Figure 3.1** presents snap shots of the systems studied at the end of the simulation time. Note that the shape of the molecules and the length of the bond are exaggerated for visualization purposes, which is a common practice in such visualizations.

$$
\begin{aligned}
E &= E_{Bonded} + E_{Non-Bonded} \\
E_{Bonded} &= E_{bond} + E_{Angle} + E_{Torsion} \\
E_{Non-Bonded} &= E_{VDW} + E_{Coulombic}
\end{aligned}
\tag{3.1}
$$

Note that the simulation results presented in this chapter are based on a United-Atom (UA) simulation for the hydrocarbon molecules, and an All-Atom (AA) simulation for solute molecules. In order to validate some of the conclusions, some results for AA simulation of hydrocarbon molecules are presented. Such results are clearly marked to distinguish between the two models. In order to compare and validate

Table 3.1: Force field parameters (data optioned from Jorgensen, Maxwell and Tirado-Rives [103] and Cygan, Romanov and Myshakin [104])

Atom	ε	σ	q	Equation
C-CO_2	0.0537	2.8	0.6512	$E_{VDW} = 4\varepsilon\left[\left(\frac{\sigma_{ij}}{r_{ij}}\right)^{12} - \left(\frac{\sigma_{ij}}{r_{ij}}\right)^{6}\right]$
O-CO_2	0.157	3.05	-0.3256	
CH3-Alkane	0.175	3.905	0	
CH2-Alkane	0.118	3.905	0	
CH4	0.2914	3.73	0	
C in CH2/C in CH3	0.066	3.5	-0.12/-0.18	$E_{coulombic} = \frac{q_i q_j}{4\pi\epsilon_0 r_{ij}}$
C in Benzene	0.07	3.55	0.115	
H in Benzene	0.03	2.42	-0.115	
H	0.03	2.5	0.06	
Bond	k	r_0	Harmonic	
C=O	2108	1.16	$E_{Bond} = \frac{1}{2}k(r - r_0)^2$	
CH3-CH2/ CH2-CH2	268	1.529		
C-C in Benzene	469	1.4		
C-H in Benzene	367	1.08		
Angle	k	θ_0	Harmonic	
O=C=O	108	180	$E_{Angle} = \frac{1}{2}k(\theta - \theta_0)^2$	
C-C-H	35	120		
C-C-C	63	120		
CH3-CH2-CH2/ CH2-CH2-CH2	58.35	112.7		
Torsional	v_1	v_2	v_3	v_4	OPLS
CH3-CH2-CH2-CH2/ /CH2-CH2-CH2-CH2	1.3	-0.05	0.2	0	$E_{torsion} = \frac{1}{2}v_1(1+\cos\varphi) + \frac{1}{2}v_2(1-\cos 2\varphi) + \frac{1}{2}v_3(1+\cos 3\varphi)\frac{1}{2}v_4(1+\cos 4\varphi)$
C-C-C-C/C-C-C-H/ /H-C-C-H (Benzene)	0	7.25	0	0	

the work, Peng Robinson (PR) equation of state is used to estimate both the phase behavior and the density using CMG-Winprop [105]. Default values are used for the component properties. Regardless how rough the values are, the ability of this EoS to predict the trend is evident [106].

3.3 Results and Discussion

3.3.1 Density plots from MD and EoS calculations

While the mixing behavior of all the gases in this study deviates from the ideal mixing behavior, the deviation for the case of CO_2 is large enough to cause the mixture density to be higher than the pure liquid hydrocarbon in some cases as shown in Figure 3.2 using PR-EoS. The ideal mixing behavior in this plot is calculated based on real pure-component densities and assuming zero excess volume. When

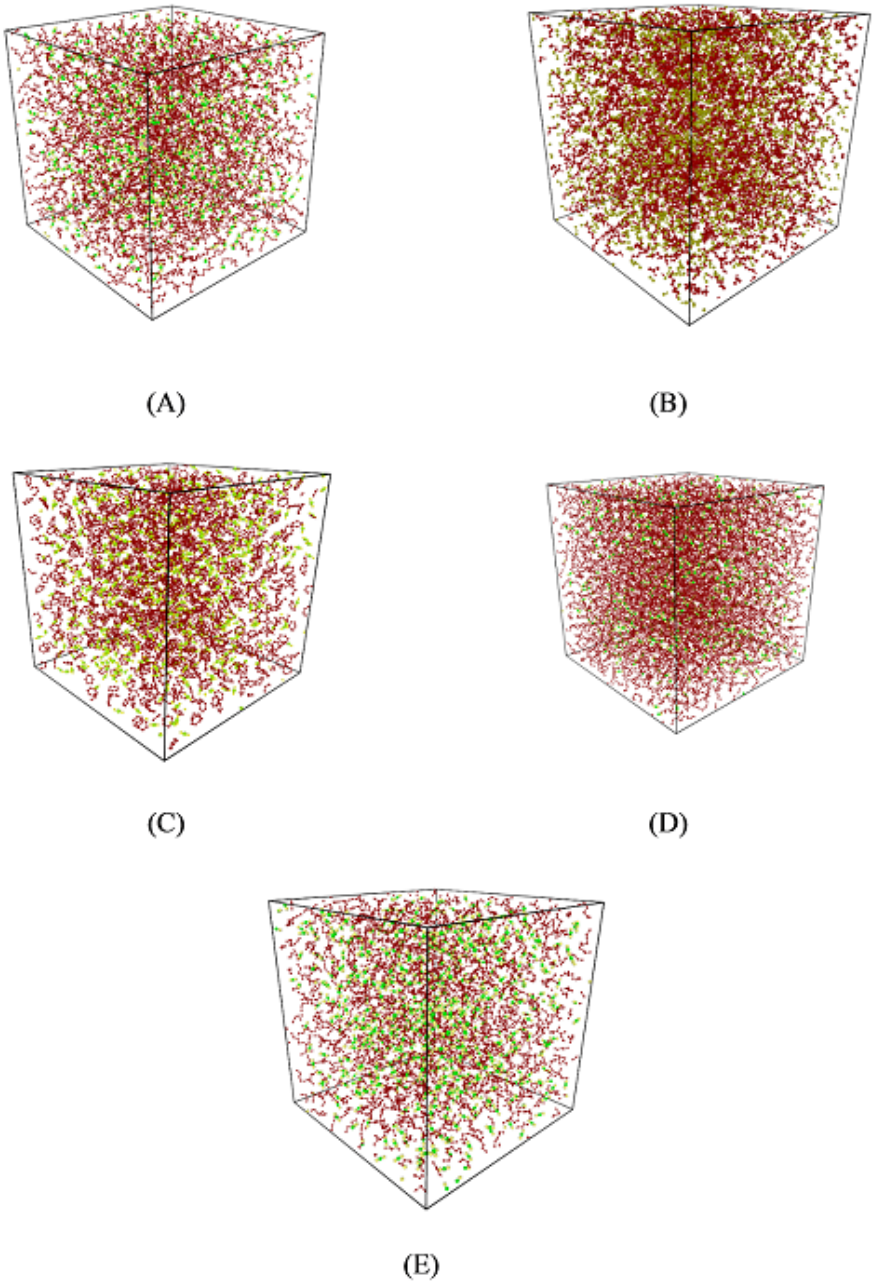

Figure 3.1: Snap shots of the systems studied with a 40% solute in the mixture: A) Carbon Dioxide-Octane B) Propane-Octane C) Carbon Dioxide-Benzene D) Carbon Dioxide-Hexadecane E) Carbon Dioxide Pentane (color code: CH3/CH2 (Octane, Pentane and Hexadecane) and CH (Benzene): red, C (carbon dioxide): green, O (carbon dioxide): yellow, and CH3/CH2 (propane): army green).

the density of pure CO_2 is higher than liquid hydrocarbon density, the increase in the density of the mixture upon mixing could be explained as a result of the addition of a higher density component. However, this behavior is also observed for cases where the density of pure CO_2 is lower than liquid hydrocarbon density, and this is what we focus on in this study. To this end, we select the temperature and pressure conditions at which CO_2's density is lower than solvent density, but similar to propanes density (shown in Figure 3.3) which has the same molecular weight as CO_2 and is used for comparison purposes.

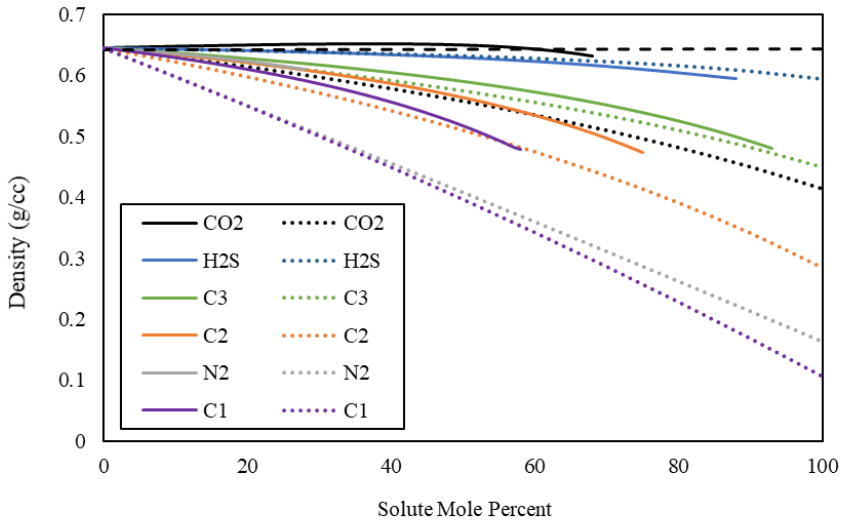

Figure 3.2: PR-EoS density calculations for octane mixtures with various gases at T = 242 °F and P = 2900 psia. The dashed lines represent the ideal mixing behavior based on zero excess volume upon mixing. The solid lines represent the non-ideal mixing behavior as calculated by PR-EoS.

Despite the ability of EoS models to capture the density behavior of CO_2 mixtures, the system structure and intermolecular interactions are not explicitly monitored and revealed in this approach. Therefore, the reproducibility of the trend of density using MD simulations was the first objective we targeted. **Figure 3.4** depicts a comparison between the results from MD and EoS calculations for CO_2,

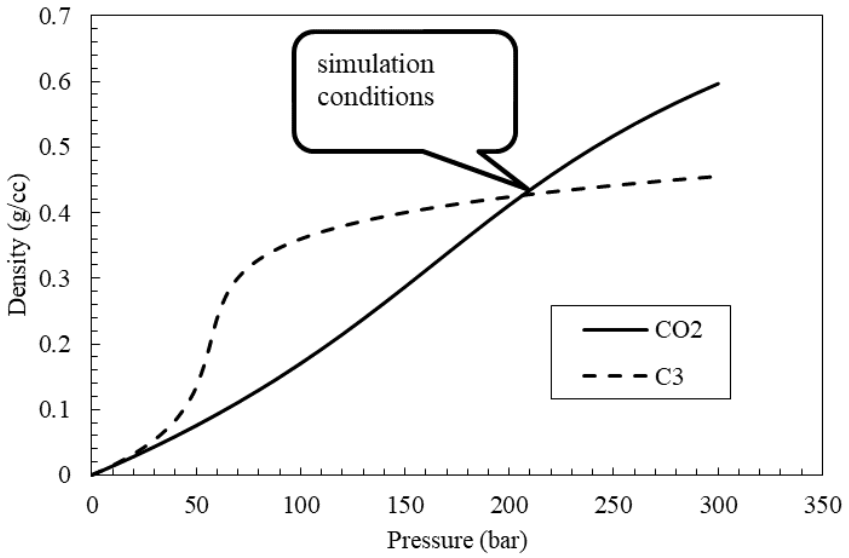

Figure 3.3: Carbon Dioxide and Propane Density at 242 °F (Data obtained from Linstrom and Mallard [30]) Based on NIST Data).

C3 and C1 mixtures with C8. The proximity of the results is satisfactory enough to derive faith in the MD calculations and start diagnosing the mixtures for key parameters controlling the density behavior. Note that these MD results are obtained without the use of any tuning parameters and are simply based on the optimized force field parameters for each molecule from literature [103]. **Figure 3.4** utilizes two vertical scales in order to match the pure octane MD and PR-EoS calculated density values for an easier visual comparison. The octane-propane mixture density from experimental measurements (data adopted from Milanesio et al. [107]), from MD simulation, and estimated by EoS with zero volume shift (EoS/Zero VS), EoS with volume shift estimated by Zra correlation (EoS/Zra VS) and EoS with volume shift estimated by interface correlation (EoS/Interface VS) are presented in **Figure 3.5**. The trend of the data does not greatly vary between these various plots, and addressing the differences is not the subject of this paper. We look at this as a

validation that the MD approach is estimating a similar trend to experiments and EoS calculations, and from that we derive faith in the results in order to analyze it at the molecular level. It is worth noting at this stage that the simplifications employed by the EoS approach do not seem to hinder its ability to provide a good estimate of the density values for this system.

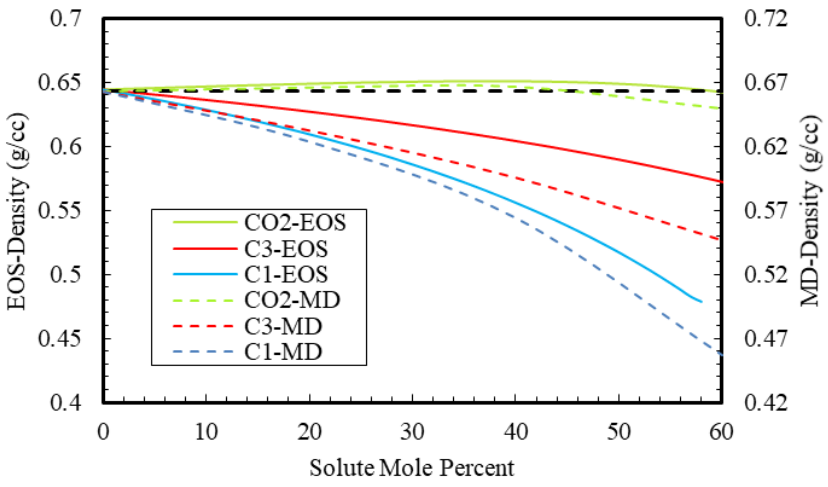

Figure 3.4: PR-EoS and MD estimations of octane-gas mixture density at 242 °F and 2900 psia.

To make sure that this behavior is not unique to the CO_2-octane system, we performed a set of MD simulations including a lighter alkane (pentane), a heavier alkane (hexadecane) and an aromatic solvent (benzene). The results are reported in **Figure 3.6**. While CO_2 mixtures sustain mixture density to a higher concentration of CO_2, C3 mixtures show a steady decrease in density. Interestingly, alkane mixtures sustain their density to a higher concentration of CO_2 compared to aromatics (benzene). The heavier the alkane is, the more sustainable its mixture density is. This is evident from comparing the pentane, octane and hexadecane mixtures.

This density behavior has been attributed in petroleum literature to the en-

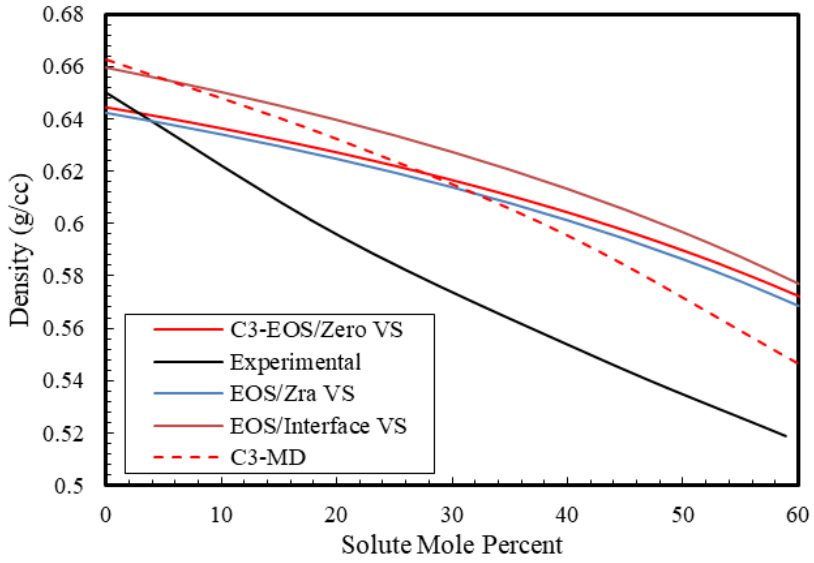

Figure 3.5: PR-EoS and MD calculations for octane-propane mixture density at T = 242 °F and P = 2900 psia

hanced coulombic forces in CO_2 mixtures, with the induced dipole in the hydrocarbon molecules, which in turn results in close packing of the system [3, 4, 2, 1]. Here, we want to properly define both the coulombic and VDW interactions. While VDW forces account for both the attractive and repulsive forces generated from dipole-dipole, dipole-induced dipole and instantaneous induced dipole-induced dipole interactions (London forces), Coulombic forces include electrostatic interactions of ions and ionic groups [108]. In other words, the molecular entity is neutral as far as VDW forces are concerned and charged in the case of coulombic interactions. With this in mind, we find that most studies in petroleum literature mislabel these induced dipole-dipole interactions as coulombic forces. However, it is in essence VDWs forces at play.

The system equilibrium volume is dependent on both the molecular size and intermolecular spacing. While the latter is controlled by the interaction energy

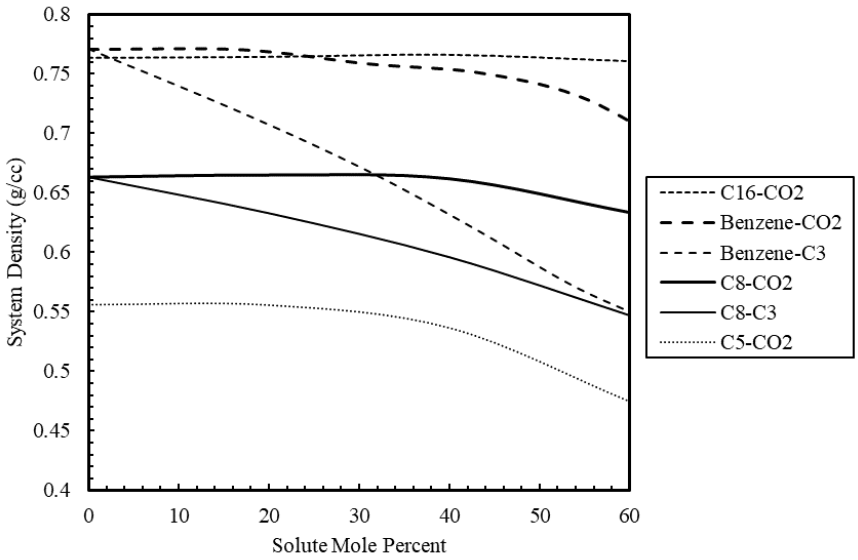

Figure 3.6: MD results of density for various gas-hydrocarbon mixtures at T = 242 °F and P = 2900 psia

between the different species, the former is dependent on the molecule structure. **Figure 3.7** presents the interaction energy between the system constituents, which is a combination of VDWs interactions and the columbic interactions when present. For solvent-solvent interactions, an increase in the interaction energy for all systems is reported with the increase of the solute concentration. This is normal given the increase in intermolecular spacing between solvent molecules as more solute molecules are added. The slightly higher line for the C3-C8 system compared to the CO_2-C8 system is in line with the density observations, where the volume occupied by the C3-C8 system is larger and the density is smaller.

The solute-solute interactions also follow an expected trend, where the addition of more solute molecules results in a lower interaction energy. Note that the solute-solute interaction is higher in the presence of alkanes than it is in the presence of an aromatic compound. This is an indication of a significant difference in packing

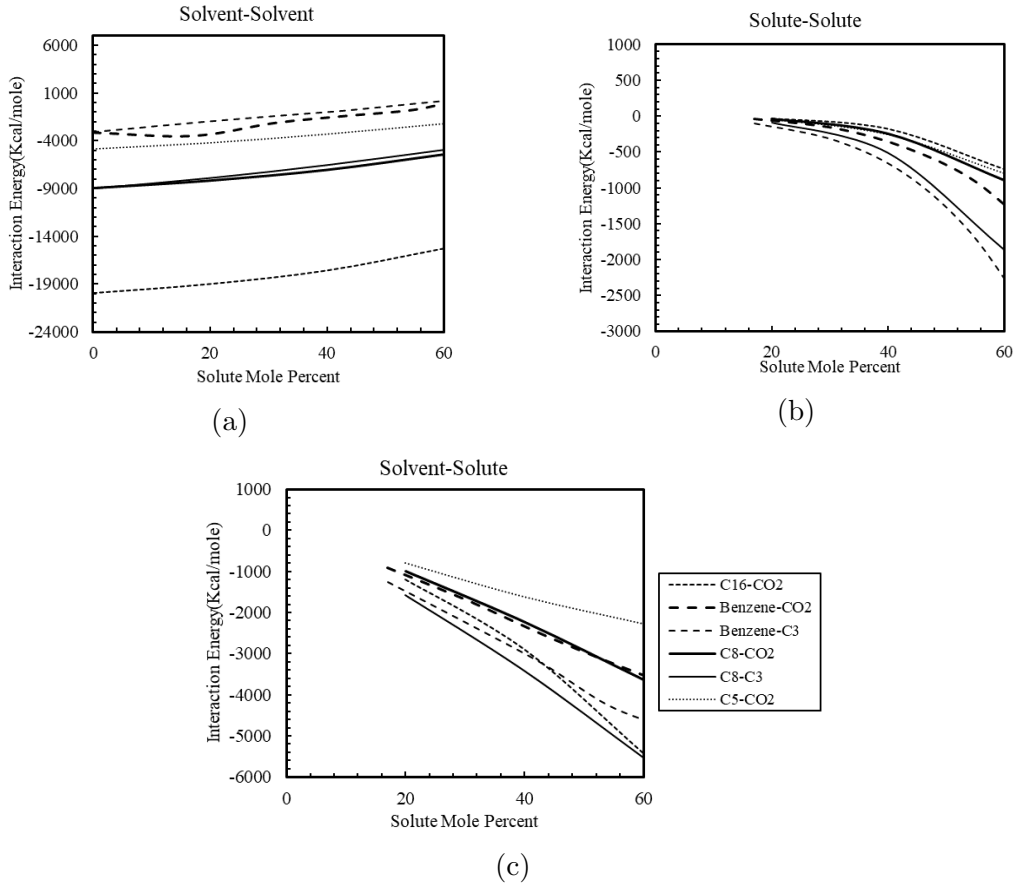

Figure 3.7: The interaction energy between systems constituents for the mixtures studied.

between the two systems. For solute-solvent interactions, a decrease in the interaction energy for all systems is reported with the increase in solute concentration. It is obvious from the data that there is less interaction energy in the case of mixtures that have C3 than there is in the case of CO_2 mixtures.

Analysis of RDF Functions

Radial Distribution Function (RDF), g(r), is a tool to explore the system structure and configuration where the normalized density is plotted versus the spatial radius. While the first peak location marks the intermolecular spacing, the peak intensity

is proportional to the atoms neighbors. The RDF converges to a value of 1 at a large-enough distance where the density of molecules within that distance is the same as the average density of molecules within the whole system. The coordination number is calculated by integrating the RDF function. A comparison between the RDFs for the various systems explored is reported in **Figure 3.8**. These plots were obtained using the center carbon atom for C3, the carbon atom for CO_2, and one of the terminal carbon atoms for octane. Considering the RDF between Solute-Solute molecules, which addresses the distribution of solute molecules around a given solute molecule, the first peak for pure CO_2 appears to the left of the first peak for pure C3, which means a closer packing for CO_2. This closer packing is mainly due to the molecule size. The increase in the peak intensity for the mixtures RDF compared to the pure cases reflects a higher coordination number. This number is higher for the solute in the presence of octane than it is in the presence of benzene. This is attributed to a more structured distribution of solute molecules in the case of octane, and a closer packing in the case of CO_2 compared to C3. The solvent-solute RDF represents the density of solvent molecules around a given solute molecule. A shift in the first peak location is reported for the CO_2 mixtures. This shift indicates the close packing of CO_2 mixtures, and in turn, the higher density of these mixtures. No significant difference is observed for peak intensity between CO_2-octane and C3-octane or CO_2-benzene and C3-benzene which implies a similar ability for the two solutes to disturb the structure of the solvent system. For Solvent-Solvent RDF, no significant change in the peak location is observed between the mixtures and the pure cases. However, a reduced peak intensity is observed for mixtures in contrast to the solute-solute cases. Studying the octane mixtures, we notice that introducing 40% of solute into the system results in a reduction in the density of octane molecules, which is a natural occurrence due to the presence of solute molecules. The peak

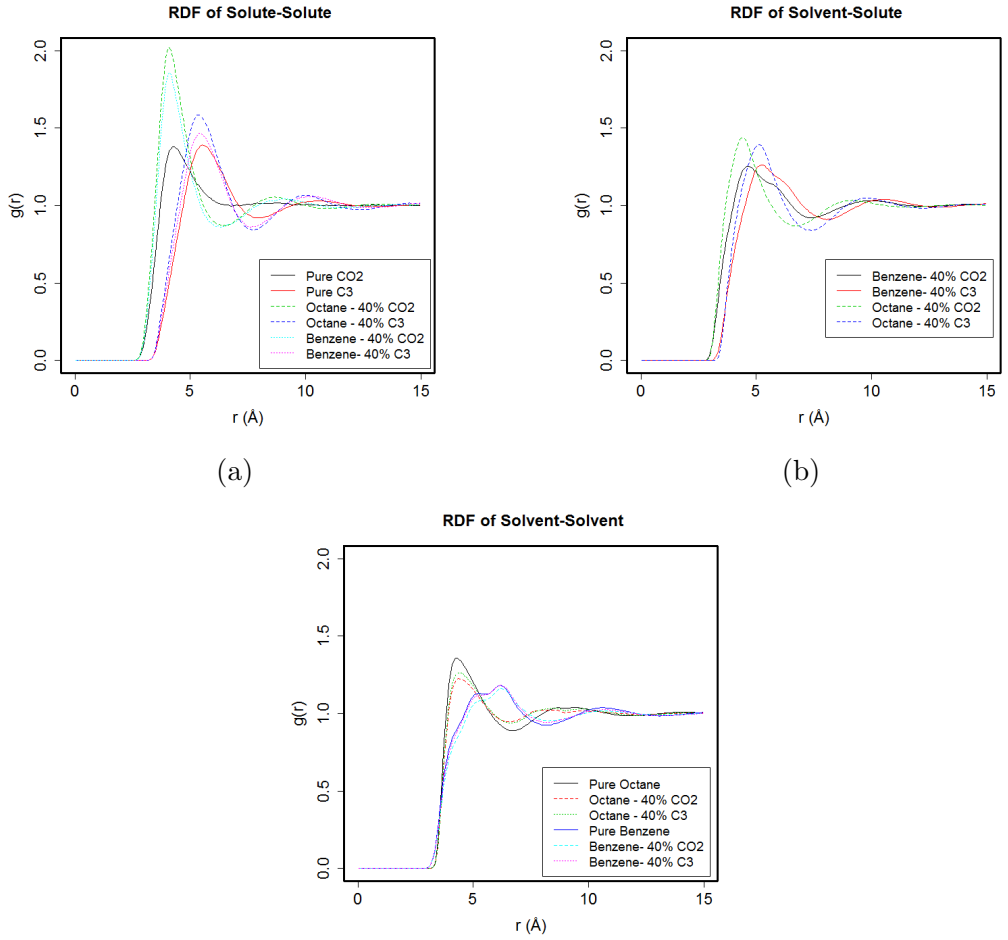

Figure 3.8: Diagnostic RDFs for the systems simulated.

is lower in the case of CO_2 compared to C3, which suggests that CO_2 is causing a higher disturbance to the system than C3.

3.3.2 Factors Affecting the Density Behavior

With various studies attributing the density behavior of CO_2 to the partial charge its atoms carry, we decided to run a systematic sensitivity study to investigate how force field parameters are affecting the density behavior. The first parameter that was evaluated was the partial charge. As indicated earlier, an All-Atom (AA) simulation

was implemented for the CO_2 molecules while a United-Atom (UA) approach was used for the hydrocarbon mixtures. In this part of the study, we include the case where All-Atom simulation is used for the hydrocarbon molecules as well. The results are shared in **Figure 3.9**. There is a 5% difference in pure octane density between the AA model and and UA model. The secondary axis is introduced to adjust for that difference. For the CO_2-C8 mixtures, whether an AA model or a UA model is used, both neutral CO_2 (referred to as NCO_2 in the figure) and CO_2 show the same density behavior up to a 35 mole% CO_2. The partial charge starts to have an effect on increasing the density of the system between 35 and 60 mole%. The partial charges for the C3 molecule in the AA model don 't seem to have an impact on the density behavior. This result is in agreement with the conclusions reported by Liu et al. [6], where the system interaction energy was decoupled, attributing only a small portion to the electrostatic interactions from partial charges

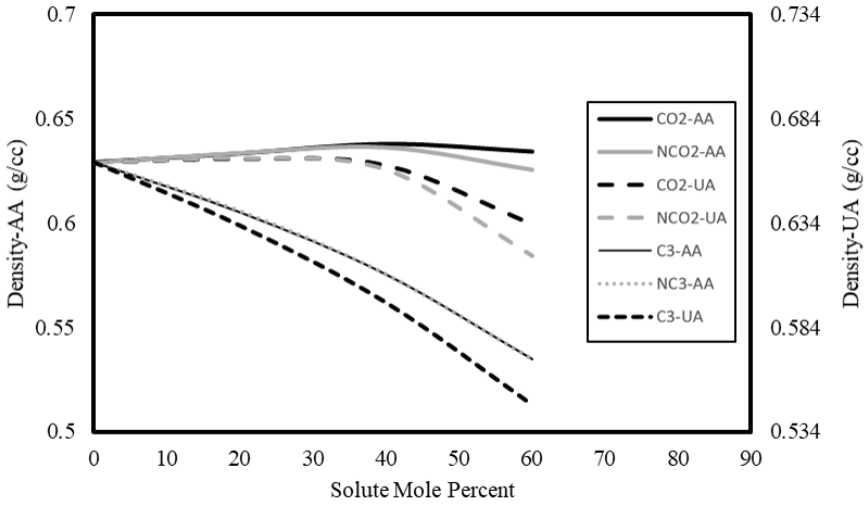

Figure 3.9: The impact of charge on AA vs. UA models on mixture density for C8-CO2 and C8-C3 systems. NCO2 and NC3 refer to the neutral molecules with no partial charge. The AA and UA distinction refers to the molecular structure used for the hydrocarbon molecules

Up to this point, our results show that the size and shape of the CO_2 molecule is the dominant factor in dictating the density behavior. The size of the molecule is reflected by the value of the sigma parameter in the force field. In order to test the hypothesis, we modified the sigma value in the CO_2 model to match that of C3. This does not represent a realistic system. It is done for the purpose of investigating the impact of this parameter in the model. The result is shown in **Figure 3.10**. The effect of CO_2 on mixture density in this case matches that of C3.

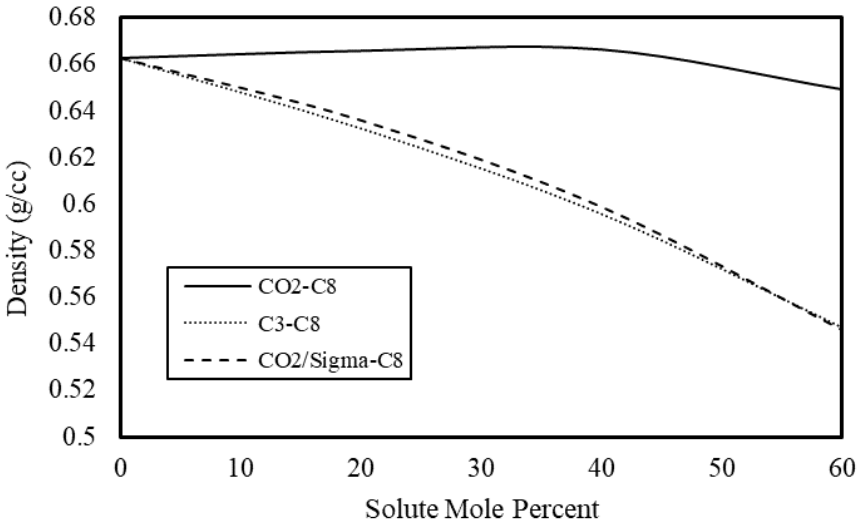

Figure 3.10: The impact of molecule size on the density behavior through the modification of sigma

3.3.3 Exploring the Stretching Theory

Liu et al. defined a tortuosity parameter relating the length of the alkane molecule in the pure and mixture cases where the negative value indicates a shrinking in the molecule length in the mixture case [6]. The plot in **Figure 3.11** shows the change in the probability distribution of tortuosity with time in peco seconds. In

their analysis of this work, Liu et al. attribute the swelling behavior of CO_2-alkane mixtures to the stretching of the alkane molecules in the presence of CO_2 molecules. In order to investigate the accuracy of this analysis, we used two models for octane molecules, the standard model that has been used in this work, and a rigid model that limits the stratching or shrinking of the molecule by multiplying the bond and angle constants by a factor of 4. The results for density behavior using the standard and the rigid models are presented in **Figure 3.11**. It shows that the model with the rigid octane exhibits the same density behavior as the standard octane model. There is a little stretching and shrinking observed as shown in **Figure 3.12** for the average length of the octane molecule, but it is not significant enough to affect the swelling or the density behavior. The probability distribution of the octane molecule length at the end of the simulation time is shown in **Figure 4.1** for the standard and rigid octane model.

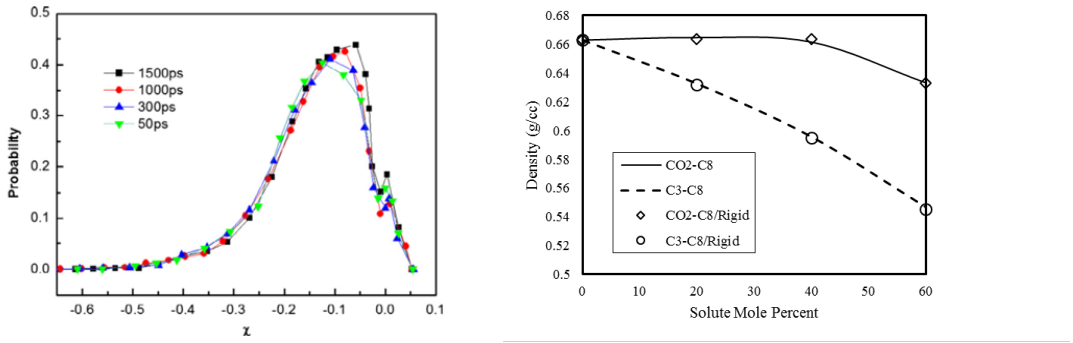

(a) (b)

Figure 3.11: a) the probability distribution of the tortuosity (χ) of alkane molecule at various simulation times in peco-second (ps)[6] b) the density behavior for rigid and flexible octane systems.

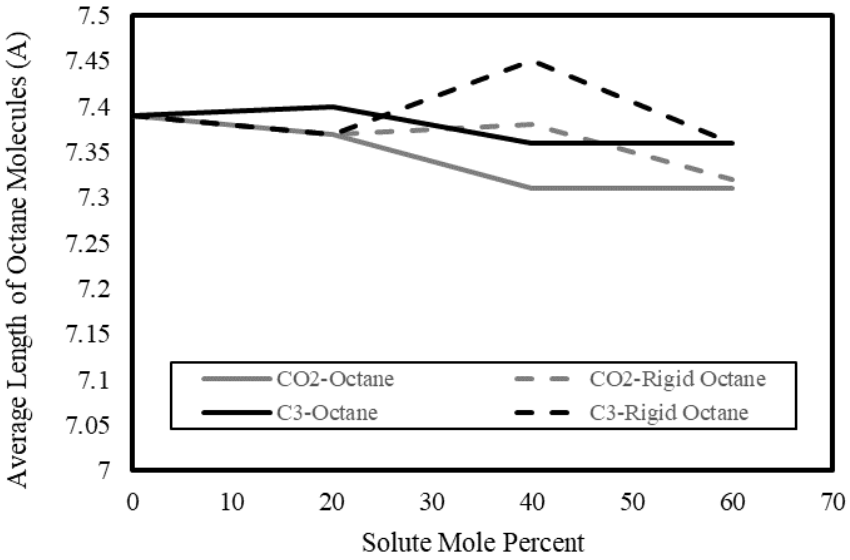

Figure 3.12: The average length of octane molecule using the standard and the rigid models.

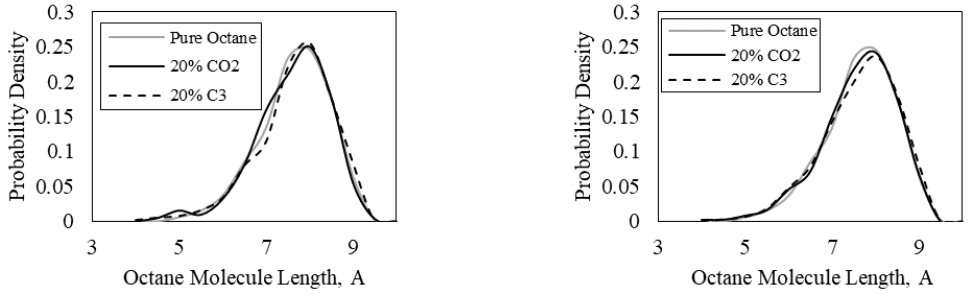

(a) (b)

Figure 3.13: The length distribution of octane molecules in pure octane, 20%, 40% CO_2 and 20%, 40% C3 mixtures a) flexible octane and b) Rigid Octane

3.4 Conclusions

We have performed a systematic molecular simulation study for the density behavior of various binary oil-gas mixtures to investigate the factors at play in the CO_2-oil density behavior. The findings presented in this paper support the following conclusions:

- The existing hypotheses in published literature attempting to explain the CO_2-oil density behavior, namely the columbic-induced dipole interactions and the possible stretching of alkane molecules, do not stand the test of in-depth analysis of molecular interactions and fail to account for the density behavior.

- The impact of CO_2 on increasing the density of the binary mixture is more pronounced in heavier alkanes.

- The MD simulation results show a closer packing of the mixtures that include CO_2 compared to mixtures that include C3, which explains the higher density observed. This packing seems to be highly correlated with the molecular size of the gas than with any interaction between the gas and the heavier hydrocarbon molecules.

Chapter 4

Asphaltene Aggregation

4.1 Introduction

Asphaltenes are defined as a solubility class, as being insoluble in heptane and soluble in toluene. The nature of the definition implies a gray area for the molecular structure of asphaltene [109, 110]. However, the condensed polyaromatic cores, the hetero-atom content and peripheral aliphatic chains have been accepted as the main characteristics of the asphaltene structure [111, 112, 113, 114]. This aromatic core might be divided to individual small cores connected by aliphatic chains, which is usually referred to as the archipelago structure, or remains as a compact condensed single core, which is usually referred to as the continental structure [115, 116]. The propensity for self-association and precipitation is what distinguishes asphaltenes from other oil constituents.

Even with the intrinsically ambiguous molecular structure, several modeling and conceptual studies have been proposed to enhance our understanding of the aggregation of asphaltenes. Carauta et al. implemented both molecular dynamics and mechanics to probe the impact of solvents on asphaltene aggregation [9]. N-butane,

n-heptane, toluene and isobutene are used to solvate two asphaltene molecules in a 100-ps simulation. Apart from the limited time and size, they managed to report the average separation between the asphaltene molecules. This separation was minimum with n-heptane and maximum with toluene. In addition, they relate the aggregation stability to the arrangement of the molecules where the most stable aggregation is observed when the aromatic cores of the molecules are stacked parallel to each other.

The interaction between carbon dioxide and hydrocarbons is complex and could explain the varied applications for CO_2 in petroleum engineering. These applications include Enhanced Oil Recovery (EOR), where the reduction in crude oil viscosity is integrated with improved swelling to provide better sweep efficiency [117, 118, 119, 120, 121, 122]. Besides, the superior adsorption characteristics of CO_2 elucidate its contribution to oil detachment and selective extraction [123, 124, 125]. However, these interactions might also induce precipitation and formation damage when the hydrocarbons have asphaltene content [126, 127, 128, 129, 130, 131].

The formation damage accompanying CO_2 flooding have been experimentally studied [97, 132]. Srivastava et al. determined the CO_2 concentration for the onset of asphaltene flocculation where limited impact is attributed to the operating pressure and crude oil properties [133]. Sim et al. reported an asphaltene onset concentration of 40 mol% of CO_2 which is in line with the results from Srivastava et al [134]. In addition, they related the permeability reduction to the relationship between asphaltene particle size and average pore throats. On the other hand, the impact of water on the precipitation of asphaltene in CO_2 flooding was the focus of Okwen where asphaltene precipitation is reduced when water is present [135]. This reduction is attributed to the buffering nature of the formation brine. These and other experimental studies document the damaging impact of asphaltene precipi-

tation on flow, but it is limited in its ability to explain the forces at play in such behavior and the factors affecting these observations.

Molecular simulation is used to investigate the characteristics of CO_2 as a solvent. Headen et al. studied the aggregation of continental asphaltene in carbon dioxide where they observed stable aggregates with longer lifetime in supercritical CO_2 compared to both heptane and toluene [14]. Sedghi and Gaul investigated the efficiency of two chemicals as asphaltenes inhibitors in CO_2 where they attributed the performance of inhibitors to the molecular forces at play [18]. They concluded that the co-injection of carbon dioxide with a polymer could curtail asphaltene aggregation. Liu et al. used the continental structure employed by Rogel [136] to study asphaltene aggregation when a representative oil sample is placed in a supercritical carbon dioxide bath. They proposed selective extraction as a mechanism for aggregate formation [6]. Lowry et al. extended the work of Sedghi and Gaul by evaluating the efficiency of polymers as dispersants for asphaltene aggregates formed in carbon dioxide over a calcite substrate [137].

While both resins and asphaltenes possess polyaromatic cores, resins are soluble in heptane/pentane. The role that resin plays in asphaltene stability is still debatable [138, 139, 136, 140, 141]. Olga et al. experimentally studied the adsorption of resins on asphaltenes; their results supported the colloidal nature of the crude oil where resins are peptizing the apshltenes [139]. Rogel used a molecular thermodynamic approach to prove the peptizing effect of resin [136]. However, Mullin et al. refuted the conceptual model of asphaltene-resin micelle [140]. In addition, Sedghi and Goual supported Mullin's claim through their experimental results [141].

Recent advances in computational tools and available molecular models allows for deeper probing of this topic. Previous studies investigating this topic have been limited in the size of the system it can handle and the scope of complexity of

such systems. Molecular simulations in representative oil samples have not been performed, and the results we share in this study show that the behavior is very different than that in pure solvents. In this work, the aggregation dynamics of asphaltene molecules is simulated using molecular dynamics where the impact of physical conditions and the nature of the solvent are probed. In addition, the impact of resins on asphaltene aggregation in carbon dioxide is investigated. Furthermore, a comparison between the impact of carbon dioxide and methane on asphaltene aggregation in a representative oil composition is discussed. The rest of this paper is organized as follows: in the methodology section, the structures of the molecules are presented along with the simulation details and matrix. In addition, the tools used in the analysis are described. In the results section, the aggregation behavior in both pure supercritical fluids and mixtures between toluene and these fluids is discussed along with the impact of both temperature and pressure on the aggregation in these systems. At the end, the impact of both methane and carbon dioxide on the aggregation behavior of asphaltene in a representative oil composition is revealed.

4.2 Methodology

In this section, we discuss the molecular structures used, along with the simulation details and matrix. In addition, the post-processing utilized in this study is briefly explained.

4.2.1 Asphaltene Structure

One of the main challenges associated with molecular simulation of asphaltenes is the molecular structure. However, two main categories have been developed with some defined characteristics: continental, which consists of one condensed poly aromatic

core with peripheral aliphatic chains, and archipelago, which consists of several aromatic islands connected by aliphatic chains [142, 143]. Boek et al. proposed a methodology to generate representative structures for asphaltene [12]. Among these structure, the widely-used structure A shown in Figure 4.1a is used in our study to represent the continental structures [19, 14, 13]. Structure B shown in **Fig.4.1b** is selected to represent the archipelago group [20]. The reason behind the selection is to have two structures that have similar molecular weights. The structure used for Resins is presented in **Fig.4.1c**. It is important to note that the presence of different functional groups and heteroatoms in the asphaltene structure affects the aggregation behavior. Published work that addressed this issue did not report a significant correlation between the nature of the heteroatom and the association free energy [144]. However, they did claim that the presence of nitrogen would reduce the electrostatic repulsion between the asphaltene dimers. In our study, we report how the nature of the polyaromatic core would impact aggregation behavior, but we do not de-couple this effect from that of heteratoms or functional groups.

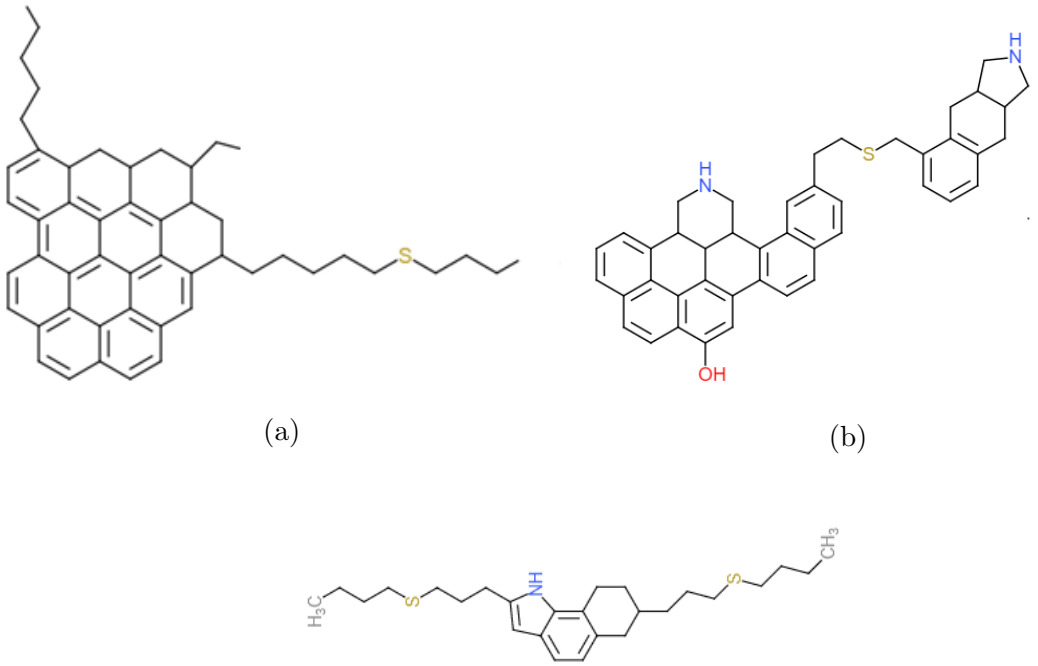

Figure 4.1: Asphaltene and Resin molecular structures: A) Continental-type [13] B) Archipelago-type [20] C) Resin [19]

4.2.2 Simulation Method and Details

Molecular simulation relies on treating the atomic nuclei classically while explicit partial charges are imposed to account for the electron cloud effects [58]. The system total energy is comprised of the intramolecular (bonded) interactions and the intermolecular (Non-bonded) interactions. The intramolecular interactions involve the interactions arising from the bond, angle and dihedral which maintain the molecular entity. On the other hand, the intermolecular interactions include both the Van der Waals interactions, which are modelled though the well-known Leonard Jones potential, and the Coulombic interactions.

All atom simulation is employed using GROMACS 5.1.6 [145]. The asphaltene molecules are randomly placed in a cubic simulation cell, then the solvent molecules

are added. The initial simulation box is set at 10 nm for all the systems except in the case of oil, where a 12 nm size is used. Afterwards, energy minimization is performed using the conjugate gradient algorithm to remove any high-energy configurations. The system is then equilibrated for 100 ps using the canonical ensemble at a temperature similar to the one used in the production run. Afterwards, the production run lasts for 100 ns using an isothermal-isobaric ensemble. The long range electrostatic forces are estimated using Particle Mesh Ewald (PME) method with an order of 4 and a Fourier spacing of 0.16 nm [146]. Modified Berendsen thermostat, V-rescale, is used to control the temperature and Berendsen pressure coupling is used to control the pressure [147, 148]. A periodic boundary condition is applied. We monitored the total energy of the system to infer the system equilibrium.

The GROMOS 54A7 force field is used to model the species [149]. The ability of the force field to reproduce the bulk fluid properties has been the focus of several research articles [150, 151]. In addition, Wang and Ferguson adopted this force field to develop mesoscale approach to study asphaltene aggregation. Flexible structure is used for CO_2 [152]. The topology files are generated using Automated Topology Builder (ATB) [153]. A 1-nm cutoff is employed for both Leonard Jones and coulombic interactions. Lorentz-Berthelot combination rules are used to estimate cross interactions [154]. The Avogadro molecular editing suite is utilized to build all molecular structures used [63]. Visual Molecular Dynamics (VMD) is used to prepare the visualizations [65].

Limited studies have focused on the dynamics of asphaltene in the gases commonly injected for Enhanced Oil Recovery (EOR). We used 27 molecule of asphaltene that makes up 7 wt.% of the system. We Then estimated the number of the remaining molecular species in the system to make up the rest of the weight percentages. The simulation matrix included in **Table 4.1** summarizes all the simulation

scenarios performed. Initially the aggregation of both asphaltene structures, continental and archipelago, is evaluated in single component solvents, C1, C3, C7, CO_2 and toluene, and binary component solvents, C1 & toluene, C3 & toluene and CO_2 & toluene. After that the continental structure is elected for further analysis for the impact of temperature, pressure, resin presence and solvent composition. We chose physical conditions that are relevant to the reservoir conditions. The representative oil composition used in section 3.4 is presented in **Table 4.2** [155]. Each one of the simulations had 27 molecules of asphaltene, then the number of molecules for the other components in the systems are calculated accordingly on a weight % basis.

Table 4.1: The simulation matrix

Structure	System Composition (wt.%)			Solvent Composition	T (K)	P (bar)
	Asphaltene	Resin	Solvent			
Continental (Structure A)	7%	0%	93%	CO_2	285	400
					300	
				C1	300	400
				C7		
				Tol		
				CO_2	350	400
				C1		
				C3		
				C7		
				Tol		
				CO_2	350	300
				C1		
				C7		
				Tol		
				CO_2	350	500
				C1		
				C7		
				Tol		
				CO_2	400	400
				C1		
				C7		
				Tol		
			30&63%	CO_2&Tol	350	400
				C1&Tol		
				C3&Tol		
		7%	86%	CO_2	300	400
					350	
					400	
					350	300
						500
		0%	93%	Oil	300	400
					350	
			30&63%	CO_2&Oil	300	400
					350	
				C1&Oil	300	
					350	
Archipelago (Structure B)	7%	0%	93%	CO_2	350	400
				C1		
				C3		
				C7		
				Tol		
			30&63%	CO_2&Tol	350	400
				C1&Tol		
				C3&Tol		

Table 4.2: Oil composition

Component	# molecules	Mol (%)
Hexane	343	13.19
Heptane	315	12.10
Octane	372	14.29
Nonane	429	16.49
Cyclic Hexane	229	8.80
Cyclic Heptane	372	14.29
Toluene	372	14.29
Benzene	143	5.50
Asphaltene	27	1.04
Total	2602	100.00

4.2.3 Analysis Methods

Molecular simulation allows to both visualize the time evolution of the computational experiment and collect the thermodynamic characteristics of the system. One of these characteristics is the average aggregation number (AAN) which is used to represent the aggregate size in terms of molecules. Clustsize, a built-in module in GROMACS, is used for AAN estimation where a 3.5 Å cutoff is implemented [19]. In addition, the Radius of Gyration (R_G) is estimated to present a shape-independent measure of the cluster size in length units and is estimated using gyrate, another built-in analysis tool in GROMACS. Both R_G and AAN estimations are based on the dynamics of the last 10 ns of the simulation time. The sphericity nature of the aggregate is assessed using ratios between the Eigen values of the gyration tensor; r_1 presents the ratio between the largest and the middle Eigen values, and r_2 describes the ratio between the middle and the smallest Eigen values [19]. When both r_1 and r_2 equal unity, the aggregate would have a spherical shape. With only r_1 equals to unity, the aggregates tends to possess an oblate shape. On the other hand, prolate aggregates tends to have a unity r_2. In addition, the interactions among asphal-

tene molecules themselves and with solvent molecules are used to probe the driving force for aggregation. In the case of a mixture, the asphaltene-solvent interaction is the summation of the interactions between asphaltene and each component in the mixture.

4.3 Results

In this section, we discuss the results for both pure and mixed solvents. In addition, the impact of temperature, pressure and resin content on the aggregation behavior is analyzed.

4.3.1 Aggregation Behavior in Pure and Mixed Solvents

The aggregate formation and stability is the initial stage for asphaltene precipitation. The average aggregate size is reported in **Fig.4.2**. For both asphaltene structures, complete aggregation is observed in pure methane and pure propane, where all 27 asphaltene molecules form a single aggregate. The addition of toluene slightly enhances asphaltene solubility of the continental structure in methane, and to a great extent in propane by reducing the aggregation number. Toluene is not successful in enhancing the solubility of asphaltene in methane in the case of the archipelago structure, but it does enhance it in propane to some extent. Both structures have a similar aggregation number in the case of heptane, with almost full aggregation, however one can notice the spread of the distribution in the case of the continental structure indicating less aggregation. Toluene is successful in dissolving the asphaltene molecules of both structures. Interestingly, the results show that carbon dioxide could be considered as an inhibitor for the continental structure and a precipitator for the archipelago structure. However, toluene greatly enhances

the solubility in CO_2 for both structures. The average aggregation number of both structure in toluene is less than 10, which is in line with experiments [140, 156]. zeng et al. used Direct-Current (DC) electrical conductivity to estimate the aggregation number in toluene at 21°C where small aggregation numbers (less than 10) were observed [156].

The results might suggest that the combination between the sulfur atom and condensed aromatic core results in an asphaltene structure that is soluble in Carbon Dioxide and the combination between the -NH and -OH groups and the divided aromatic core results in an asphaltene structure that is insoluble in carbon dioxide. However, since we did not introduce more variations in the structure, we avoided claiming this as a finding in this work.

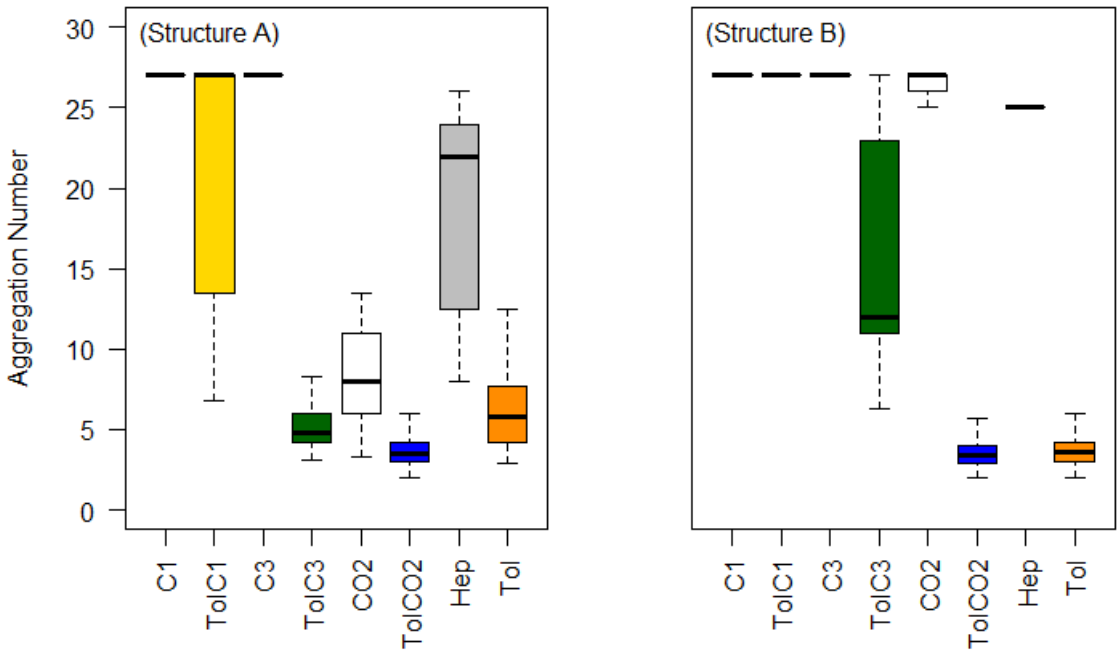

Figure 4.2: Average aggregation number of Asphaltene aggregates for both structures A and B at T = 350 K and P = 400 bar (toluene mixtures consist of 67 wt.% toluene, 30 wt.% gas and 7 wt.% asphaltene)

The aggregate shape and molecular orientation of the continental structure is

Figure 4.3: Snap shot of time evolution of the system of continental asphaltene with different solvent at T = 350 K and P = 400 bar (solvent molecules are removed for clarity). The length of the final simulation box is included in parenthesis for each solvent in Å

reported in **Fig.4.3**, where visualization states of the time evolution of the system are presented. Open structure aggregates are observed for all solvents, where the aggregate contains other molecular species besides asphaltene. More scattered aggregates are observed for toluene and carbon dioxide. In addition, the parallel arrangement of the polyaromatic cores is found to be the energetically favorable orientation [15, 9]. However, the loss of configurational entropy limits the growth of this orientation [17].

The stability of the aggregate and dynamics of the aggregate size are related. **Figure 4.4** presents the dynamics of the aggregate size, which is presented as the

aggregation number versus time for the 100 ns of the simulation. For the continental structure, complete aggregation is observed for all aliphatic solvents. However, only methane exhibits a highly stable aggregation. Conversely, both propane and heptane experience fragmentation events. It is worth noting that the delayed complete aggregation observed in methane, up until 70 ns, could be attributed to the formation of two quick stable aggregates with limited diffusion. On the other hand, the other solvent systems experience an oscillating behavior controlled by the balance between the formation and breakdown of the aggregate. This behavior is clearly seen in toluene, carbon dioxide and the toluene/propane mixture. As for the archipelago structure, a quick and stable formation of the aggregate is observed for both pure and mixed methane. For heptane, propane, and carbon dioxide, complete aggregation is reached, yet, few fragmentation events are experienced. While only a delaying effect is observed for toluene on the asphaltene aggregate growth in propane, stable dispersion is observed for asphaltene in mixed carbon dioxide. An oscillating behavior is observed for toluene and carbon dioxide/toluene mixtures.

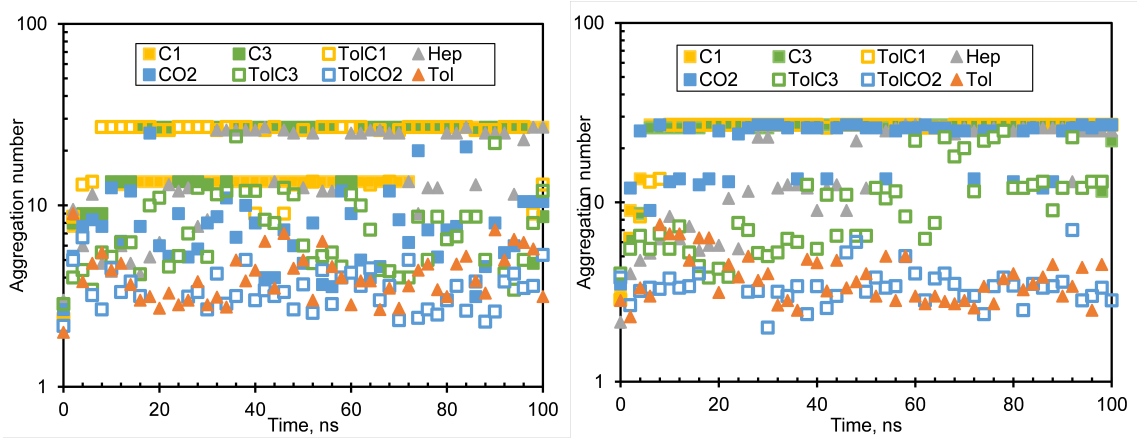

(a) Continental (structure A)

(b) Archipelago (structure B)

Figure 4.4: Aggregation dynamics for Asphaltene structure for 100 ns at T = 350 K and P = 400 bar

4.3.2 The Size and Shape of Aggregates

The aggregate volume, which could be quantified by R_G, is contingent on both the aggregate size and molecular arrangement in the aggregate. **Figure 4.5** presents R_G for various systems. Denser aggregates are observed in aliphatic solvents for both asphaltene structures; This is reflected in the small value of R_G, even though the corresponding aggregate has a larger number of asphaltene molecules as observed in **Fig.4.4**. The aggregate formed in propane is the most compact, followed by methane, and finally heptane. A broader multimodal distribution is observed when toluene is added to methane or propane; This reflects the varying size of the largest aggregate in the system over the last 10 ns of the simulation time. The larger size, compared to pure aliphatic solvents, reflects the dispersed nature of the aggregate resulting from the addition of toluene. While a shift in the peak location and reduction in the peak amplitude is evident for propane mixtures, only a reduction is observed for methane mixtures, with a slight shift of peak location in the case of the archipelago structure. While introducing toluene to the system results in a more porous aggregate for propane and a limited porous aggregate for methane, it results in a denser aggregate for carbon dioxide. Observing the distribution of R_G in carbon dioxide, the compact structure of the aggregate in the case of the archipelago structure is evident in the single peak and small R_G value, while the larger value and wider distribution in the case of the continental structure is another quo into the enhanced solubility of that structure in carbon dioxide. The addition of toluene results in a wider spread of the distribution for both structures, resulting from enhanced solubility. The radius of gyration in toluene is observed to be around 3.8 nm, which is in a close proximity to the experimental value of 3.6, measured for heptane-precipitated asphaltene in toluene using Nuclear Magnetic Resonance

(NMR) [67]. It should be noted that R_G describes aggregates formed from asphaltene molecules with a definite chemical structure, while experimentally-measured values describe aggregates formed from a mixture of heptane-precipitated asphaltenes, of varying structures. The comparison and close proximity is meant to indicate the appropriateness of the selected structures.

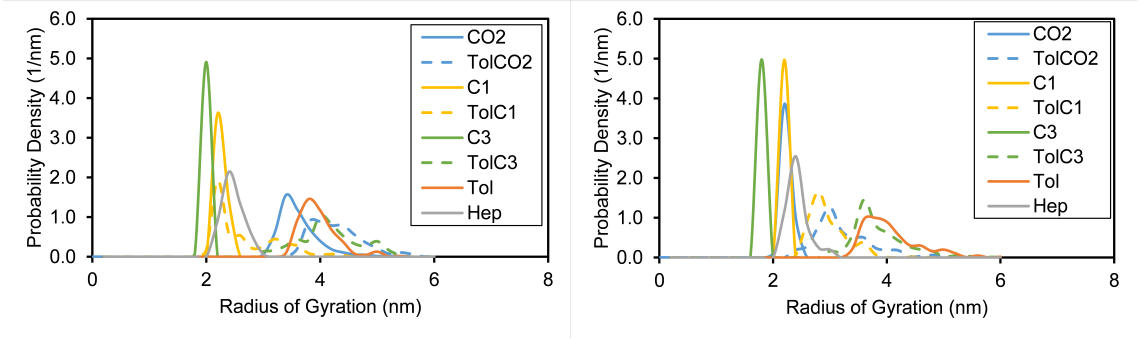

(a) Continental (structure A)

(b) Archipelago (structure B)

Figure 4.5: The radius of gyration of asphaltene aggregates at T= 350 K and P = 400 bar

The sphericity nature of the resulting aggregate could be assessed using the dimensional map, which represents the ratios of the Eigen values of the gyration tensor. The dimensional map is presented in **Fig.4.6**. Limited dependence on the solvent or structure type is observed for r_1. The aggregate structure is closer to a spherical shape in the solvents that have C1, where r_1 and r_2 have similar values. The continental structure forms a spherical aggregate in pure C7 and C3, while the archipelago structure forms a spherical aggregate when mixed with pure CO_2. Both structures form the most prolate aggregates in the toluene/C3 mixture. Experimentally, the aggregate dimensions could be assessed through Small-Angle X-ray and Neutron Scattering (SAXS/SANS) [69, 70, 71]. For instance, Eyssautier et al. used SAXS and SANS to measure the aggregates in toluene where aggregates with a height of 6.7 Å and a diameter of 32 Å were observed, roughly equal to an

r_1 of 1 and an r_2 of 2 [69]. While suggesting a disk-shaped aggregate similar to the experimental observations, our results report relatively thinner disks.

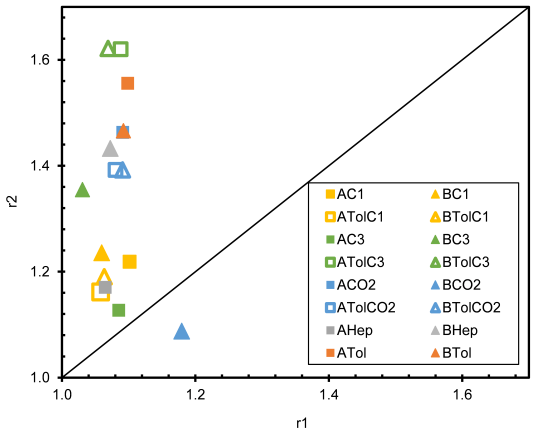

Figure 4.6: Dimensional map of average aggregate geometry

4.3.3 The Molecular Interactions Driving Aggregation

The molecular interactions drive and determine the aggregation state of asphaltenes. The average interactions, with uncertainty that ranges from 0.092% in single-component solvent up to 0.3% for multi-comment solvent, are presented in **Fig.4.7**. ASP-ASP Coulombic interactions (Coul) are independent of the nature of the solvent, while Lennard-Jones interactions (LJ) are affected by the nature of the solvent. Strong LJ attractive forces are observed between asphaltene molecules in aliphatic solvents. These attractive forces have a lower value in toluene, and in most toluene mixtures, where it is replaced by interactions with the solvent molecules. The interactions between asphaltene molecules in CO_2 are stronger in the case of structure B, which is in line with the precipitation-like behavior observed earlier. ASP-solvent columbic interactions exhibit more dependence on the solvent type. While both pure carbon dioxide and the carbon dioxide mixture with toluene have attractive columbic forces, the other systems have repulsive interactions. In addition, a wide spectrum

is observed for LJ interactions between asphaltene-solvent compared to ASP-ASP. The solvating power could be related to the ability of the solvent to disturb the ASP-ASP interactions and replaced it with attractive interactions between the solvent and asphaltene. This is the case for CO_2, toluene and their mixture. Clearly, the aggregation behavior is driven by the LJ interactions and not the charge-based coulombic interactions.

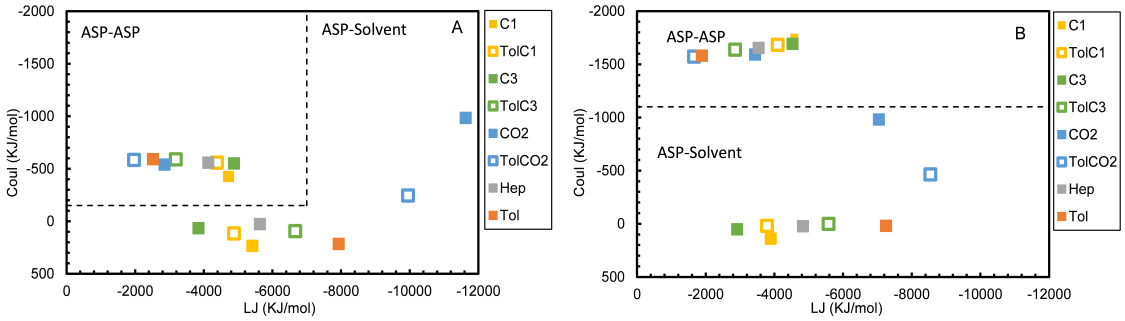

(a) Continental (structure A) (b) Archipelago (structure B)

Figure 4.7: Intermolecular interactions at T=350 K and P = 400 bar

Another observation worth noting is on the impact of toluene on the coulombic interaction when mixed with C1, C3 and CO_2. for the continental structure, a slight increase in the value of the attractive interactions between ASP-ASP molecules is observed, while for the archipelago structure, toluene results in slightly reducing those interactions.

4.3.4 The Effect of Temperature and Pressure

For the remainder of the discussions, we investigate the behavior of the continental structure, structure A, which experienced solubility in CO_2, to examine the factors affecting this observation. The impact of temperature on the aggregate size is reported in **Fig.4.8a**. Solubility in toluene seems to be independent of temperature.

Higher temperature results in a reduction in the aggregation number in heptane, which is in line with experimental observations [157]. It is important to mark how carbon dioxide's characteristics as a solvent are changing as it crosses the critical point to a super critical fluid. Carbon dioxide has a critical temperature of 304 K. For temperatures lower than the critical temperature, complete aggregation is observed. On the other hand, for temperatures higher than the critical temperature a significantly lower aggregation number is observed with a dynamic balance between aggregate growth and reduction. The aggregation behavior for methane turns out to be independent of temperature, however it does occur more rapidly at higher temperature; this result is not included in the figure for brevity. Note that the aggregation behavior in CO2 and heptane, represented in the aggregation number, seems to correlate with the value of LJ interactions between the solvent and Asphaltene molecules. This almost-direct correlation is presented in **Fig.4.9a** for heptane and **Fig.4.9b** for CO2.

The effect of pressure on the aggregation behavior is presented in **Fig.4.8b**. Limited impact is observed on the aggregation behavior in carbon dioxide and toluene. A clear non-monotonic impact of pressure on aggregation behavior in heptane is observed, where lower aggregation can be seen at the lowest (4350 psi) and highest (7250 psi) values of pressure, and a high aggregation number can be seen at 5800 psi.

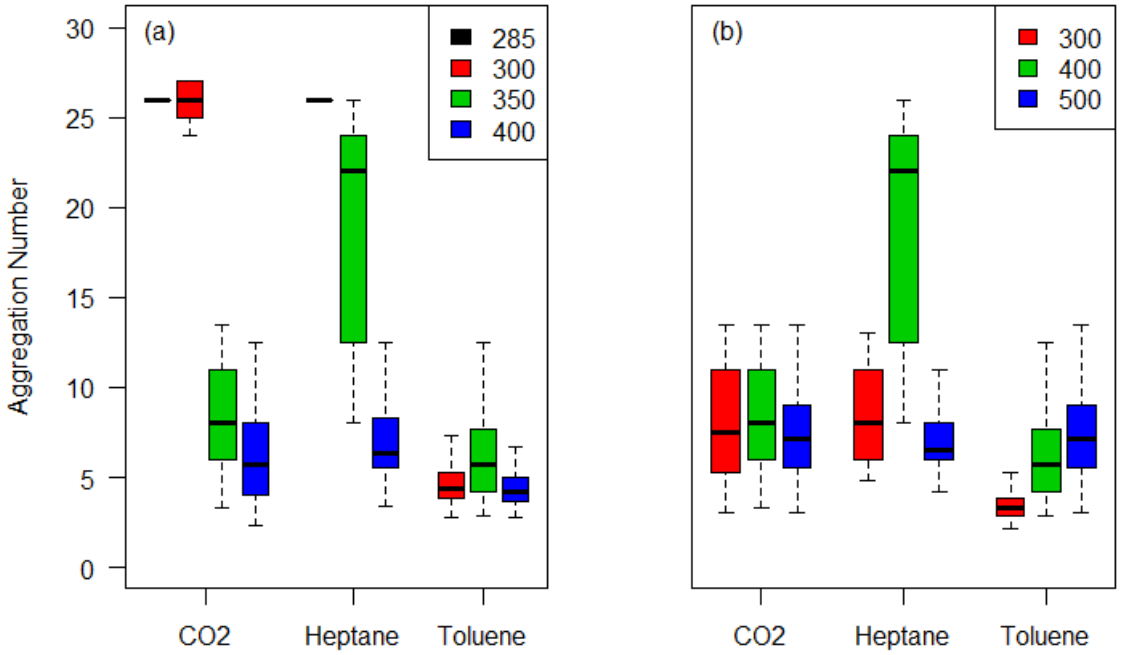

Figure 4.8: The average aggregation number for continental asphaltene dependence on: a) Temperature, K at P = 400 bar and b) Pressure, bar at T = 350 K

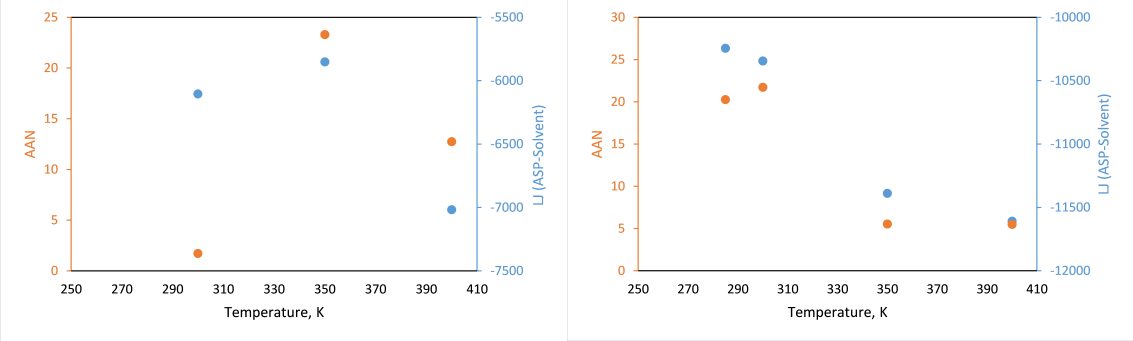

(a) Heptane (b) Carbon dioxide

Figure 4.9: The average aggregation number versus the intermolecular interactions

4.3.5 Investigating the Effect of Resin

The impact of resin molecules on asphaltene aggregation in carbon dioxide is presented in **Fig.4.10** for different temperature and pressure values. Limited impact is reported for resin on the AAN at the temperatures and pressures studies, except at

pressure of 500 bar where a significant reduction in the AAN is observed. Based on their simulation results, Lui et al. also suggest limited impact for the resins on the asphaltene aggregation in CO_2 [6]. However, there is still an ongoing debate about the resin impact on asphaltene stability in different solvents [138, 139, 136, 140, 141]. More investigation would be beneficial to better understand this role.

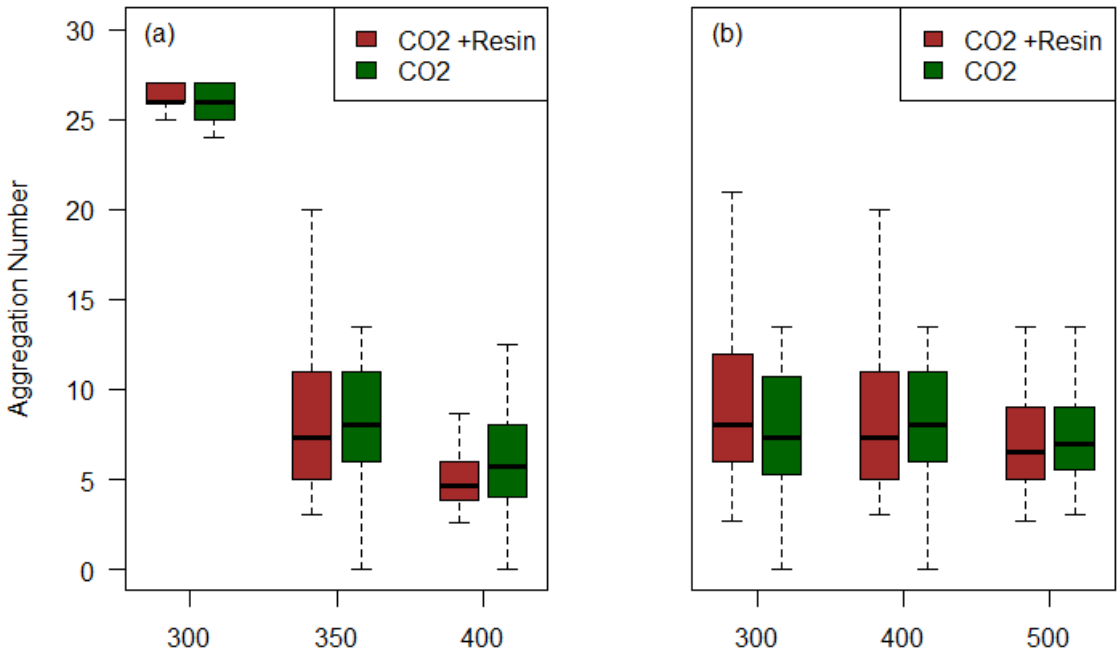

Figure 4.10: The average aggregation number in carbon dioxide with and without resins presence for asphaltene structure A: a) the impact of temperature at P = 400 bar and b) the pressure at T = 350 K

The impact of resins on the sphericity nature of the asphaltene aggregate formed in carbon dioxide is presented in **Fig.4.11**. There is a more pronounced impact at lower temperatures, 300 K and 350 K, compared to other temperature and pressure values.

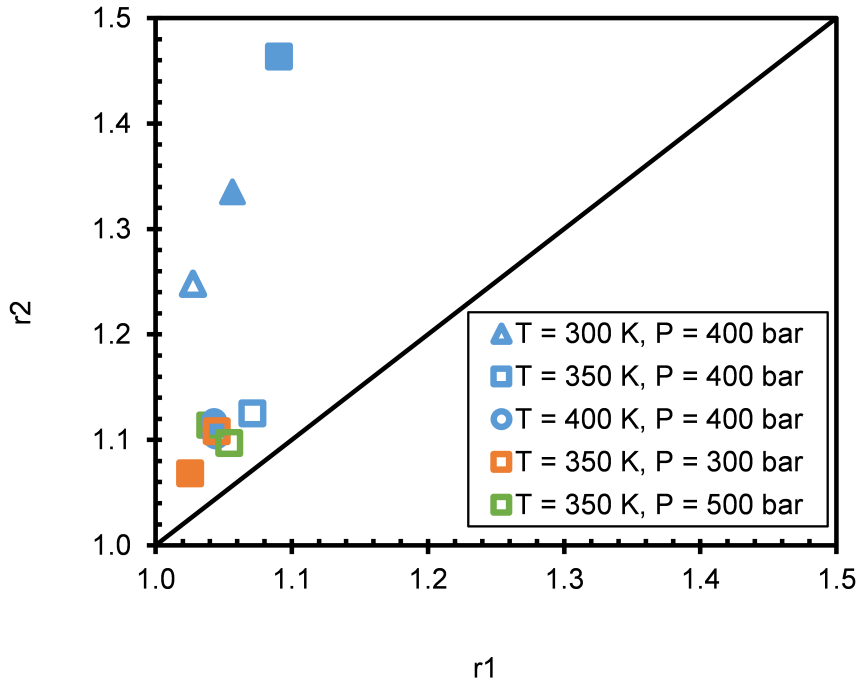

Figure 4.11: The dimensional map in carbon dioxide for asphaltene structure A (solid symbols represent carbon dioxide and open symbols represent carbon dioxide and resin)

The impact of resin presence on the molecular forces observed in CO_2 mixtures at different pressures and temperatures is presented in **Fig.4.12**. For ASP-ASP interactions, limited impact is observed for resins. However, the temperature affects the LJ and coulombic interactions of this system differently. While a positive relationship is observed between temperature and coulombic forces, a negative one is observed with LJ. On the other hand, a nonmonotonic impact is observed for pressure on both LJ and coulobmic forces when resin is not present; this impact became negligible when resin is present.

For ASP-solvent interactions, similar LJ interactions are observed with and without the resin presence. However, a slight reduction in the columbic forces is reported in resin-containing systems. On the other hand, the resin presence turned

the LJ forces to be more pressure-independent and non-monotonically temperature-dependent. It is worth noting that CO_2 in a liquid state results in a reduction in both coulombic and LJ interactions regardless of the resin presence.

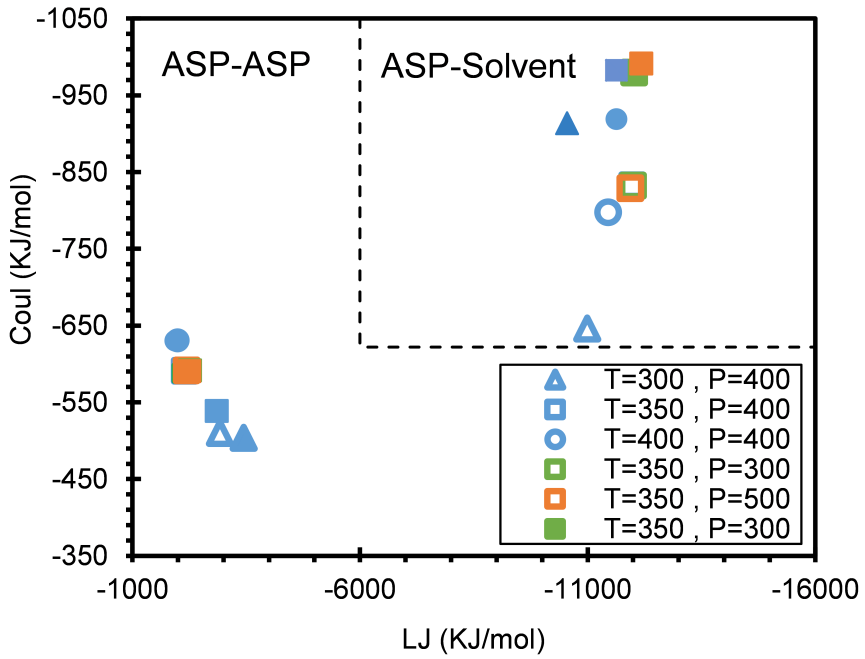

Figure 4.12: The impact of pressure and resin on asphaltene-asphaltene intermolecular interactions in carbon dioxide for asphaltene structure A (solid symbols represent carbon dioxide and open symbols represent carbon dioxide and resin)

4.3.6 Aggregation Behavior in an Oil Mixture

The stability of asphaltene molecules in a representative oil composition is discussed in this section. The aggregation number for oil, oil with 30% methane and oil with 30% carbon dioxide at temperatures of 300 and 350 K and pressure of 400 bars is presented in **Fig.4.13**. Interestingly, the effect of methane is more pronounced for the temperatures studied. On the other hand, limited influence is observed for carbon dioxide. In addition, a reduction in the aggregation number for the

oil/CO_2 mixture is observed as the temperature decreases which is in agreement with the Verdier et al.'s experimental observation [128]. Similar observations to what was seen earlier are made when studying the shape and size of aggregates in these mixtures. The addition of methane results in a smaller radius of gyration, indicating a compact asphlatene aggregate as shown in **Fig.4.14**. The addition of methane also has a significant impact on LJ interactions, which is in line with the earlier reporting in this study.

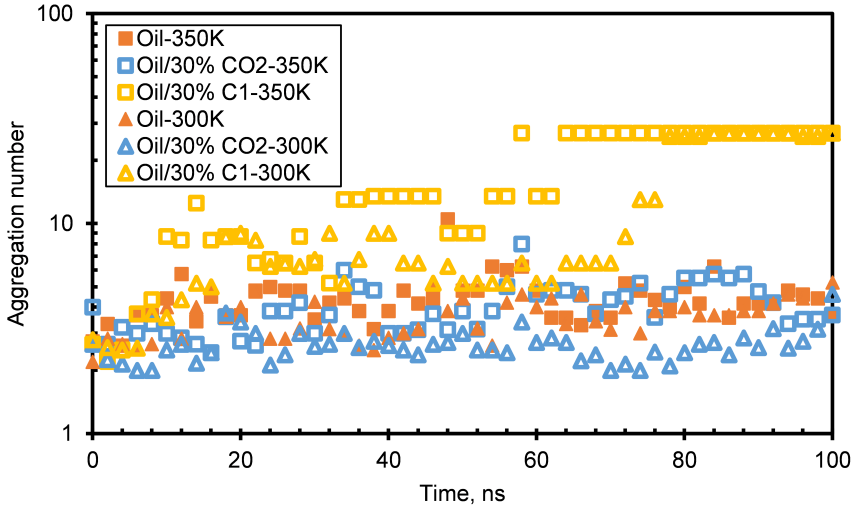

Figure 4.13: Aggregation number of Asphaltene aggregates for asphaltene structure A at T = 350 K and P =400 bar

Limited impact is observed for temperature on both ASP-ASP and ASP-Solvent interactions when either carbon dioxide or methane is present in the solvent as shown in **Fig.4.15b**. For ASP-ASP interactions, the CO_2 and oil mixture exhibits similar interactions to those observed in the oil mixture at lower temperature, while at high temperature, a reduction is observed in both coulombic and LJ interactions. This might be driven by the attractive coulombic and strong attractive LJ forces observed between asphaltene and solvent when CO_2 is present in contrast to the

other systems. This suggests that CO_2 has either a limited or reducing impact on the aggregation of asphaltene in oil mixtures with concentrations up to 30 mol%. In contrast, the presence of methane does increase the LJ interactions between asphaltene molecules at both temperatures, and coulmbic interactions at the lower temperature only. This led to minimal interactions reported between ASP-Solvent molecules.

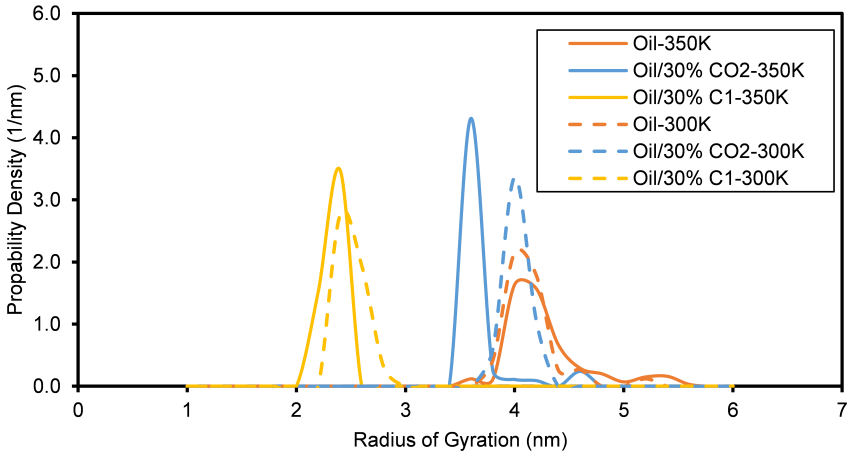

Figure 4.14: Radius of gyration distribution in representative oil mixture

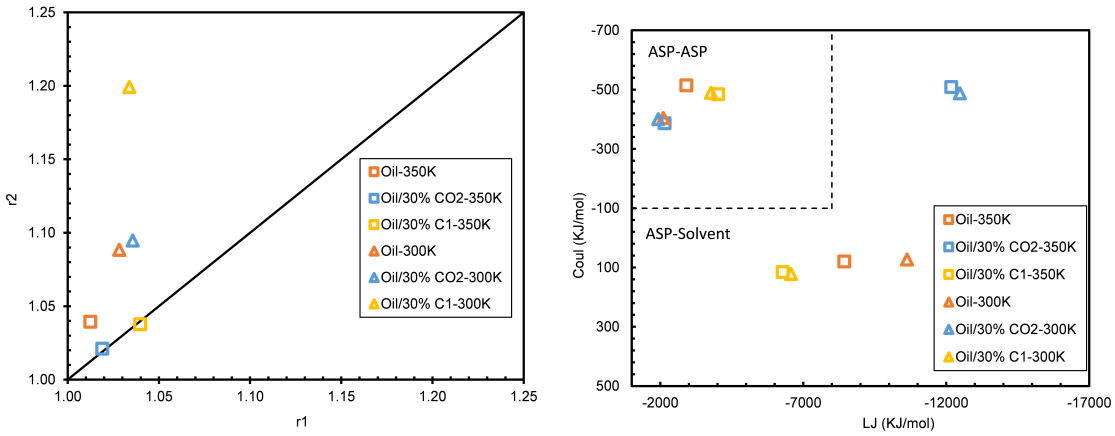

(a) (b)

Figure 4.15: Asphaltene A aggregates in representative oil mixture: a) the dimensional map for Asphaltene aggregate b) the intermolecular interactions

4.4 Conclusions

The dependence of asphaltene aggregation dynamics on the physical conditions and composition of the system is investigated with a focus on the effect of CO_2. The following remarks could be drawn:

- The molecular interactions present in the system determine the dynamics of asphaltene molecules. The stronger the asphaltene self-interactions are, the more prone it is to aggregate. Favourable solvent/asphaltene interactions could replace the asphaltene self-interactions and lead to a dissolved state for the asphaltene. The relative value of LJ interactions seems to be a good predictor of solubility.

- The state of CO_2 is a crucial factor for determining its characteristics as an asphaltene solvent. Continental asphaltene could be dissolved in supercritical CO_2 mixtures, in contrast to archipelago asphaltene which forms larger aggregates. In addition, liquid CO_2 could be considered an asphaltene precipitator for both structures.

- The continental aggregate size in CO_2 correlates negatively with temperature, while a non-monotonic effect of pressure on aggregation is observed in the case of heptane.

- The presence of resin has limited impact on the aggregation propensity of asphaltene in CO_2.

- Continental asphaltenes form diffusive aggregates containing more than 4 molecules with R_G of 4 nm in oil mixtures. This aggregate grows to take in all asphaltenes in the mixtures and become denser with half the R_G when

30 wt% C1 is introduced to the mixture. However, when a similar percentage of CO_2 is introduced, a slight reduction in R_G is observed. Depending on the structure of the asphaltene molecule, methane injection can be more of a problem than carbon dioxide injection when it comes to the potential for precipitating asphaltenes

Chapter 5

Water Salinity and Oil Recovery

5.1 Introduction

Recent challenges in petroleum engineering have initiated several research areas. Among these, LSW has been one of the main research areas in petroleum engineering for several decades [158, 159, 160, 161, 85, 162, 163]. The interest is driven by the improved performance observed for only some of the tested cores and field tests [23]. The contradiction reported in experimental results and field studies necessitate a fundamental understanding of LSW. Besides, it widen our analysis from water salinity to water chemistry, where both ions and water specific characteristics could be brought into the scene to provide elucidations for the observations. Several mechanisms have been proposed to better understand the essence of LSW. However, given the intrinsic heterogeneity involved in the reservoir system and the contradicting, yet extensive, literature, LSW is one of the main research areas lacking deep understanding.

The feasibility of LSWF is documented in some field pilots. Seccombe et al. (2010) reported the first inter-well application of LSWF in Endicott field, Alaska

where they confirmed the behaviors observed in both core and single well [164]. They observed a reduction in the residual oil in place. On the other hand, Skrettingland et al. (2010) reported both core and field results of the LSWF applications in Snorre field, North Sea where low potential is observed [165]. In addition, Mahani et al. (2011) analyzed the response of LSWF applied in two fields in Syria where gain is observed for one field when LSWF is applied in the secondary mode and no gain is observed for another when it is applied in the tertiary mode [166]. However, they illustrated that the LSW 's gain in these field are not related to the recovery mode, instead it is related to the reservoir characteristics.

In the petroleum literature, Ligthelm et al. (2009) suggested that the DLE is the main mechanism for wettability modification in sandstones [167]. In addition, Nasrallah and Nasreldin (2014) in one of the most-cited papers on the topic claimed that the DLE is the main mechanism for IOR where they back their premise by measuring zeta potential measurements showing a shift towards more negative values for both W/O and W/R interfaces as water salinity decreases [168]. In addition, they discussed the interplay between salinity and pH impact on the performance of LSWF. Whereas water salinity controls how the surface charge is compensated, the pH determines the charge induced on the interface. Recently, Jackson et al. (2016) supported DLE where they suggest that the electrostatic repulsion between W/O and W/R interfaces are essential for the improved oil recovery (IOR) to happen [169].

The double layer usually refers to the stern and the diffuse layers. Whereas the former represents a compact layer of the adsorbed ions with a sharp decrease in the electrostatic potential, the latter includes an array of ions whose distribution follows Poisson-Boltzmann equation [170]. The distribution and dynamics of molecular species in these layers is described classically in light of DLVO theory where the

Van Der Waals (VDW) and electrostatic interactions are used [171]. While VDW are short-range interactions independent of electrolyte concentration, electrostatics are long range interactions dependent on the electrolyte concentration [172]. On the other hand, non-DLVO forces like hydration and hydrophobic interactions, have been introduced to properly account for the intermolecular forces dominating at small scales [173, 174, 175].

Given, the quintessential role the surface charge plays in the structure of the double layer, this charge could be permanent or temporary [176]. While the permanent charge could be induced by lattice substitutions encountered in the charged clay minerals, the temporary charge could be induced by the ions preferential adsorption over the surface. Interestingly, the nature of the surface charge determines its response to water flooding. In the case of temporary charge, the introduction of an ion-diluted water to the system disturbs the equilibrium state and might result in a release of the adsorbed ions. Consequently, the surface charge, its induced electrical field and its potential are reduced. On the other hand, the permanent charge is not impacted by water salinity. Yet, its electrical field and potential would be since longer distance is required for electric field to be screened. Therefore, a permanent charge would be an indispensable parameter for DLE mechanism to happen.

In addition, the heterogeneous composition of crude oil would complicate the interaction of the brine/oil interface with water salinity. Crude oil contains several functional groups whose presence and concentration determine the charge of the crude oil [177]. Among these functional groups, the acid group, COOH and the base group, N are extensively used to model crude/water interactions in almost all the studies using surface complexity model to thermodynamically predict the interface response to the changes in water salinity [178, 179, 180, 181, 182, 183, 184, 185]. In addition, Wu et al. (2017) measured the disjoining pressure induced between

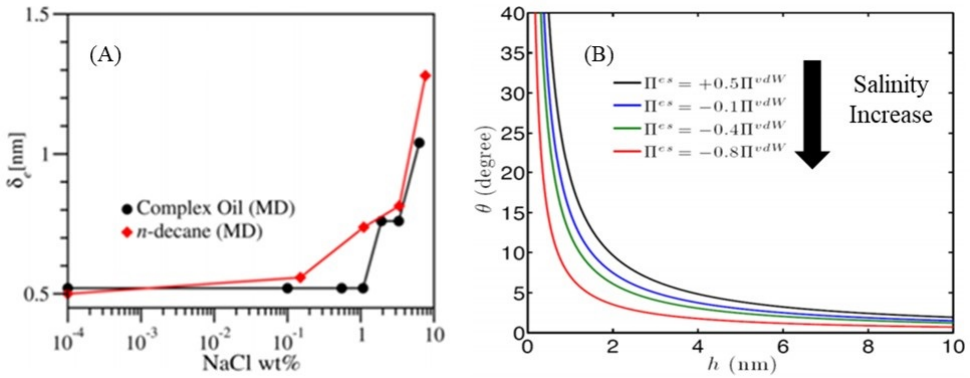

Figure 5.1: Contradicting results between the molecular simulation and classical disjoining pressure: a) film thickness from molecular simulation [26] b) film thickness from disjoining pressure(modified after Minyt and Firoozabadi [189].)

mica substrate and oil functional groups where they observed strong adhesion for both N and COOH group.[186] They reported the inapplicability of conventional DLVO to model the experimental. Therefore, they proposed an extended version which include the structural force contribution which successful model the measured disjoining pressure for various functional groups. Nonetheless, limited impact is reported for salinity on the interfacial tension between water and crude [85, 187].

Double layer expansion is confirmed in Minyt and Firoozabadi 's review [23]. However, the results from the same research group suggest the opposite. Jimenez-Angeles and Firoozabadi reported a positive relationship between the water film thickness and water salinity as shown in **Figure 5.1** [27, 26]. They measured the film thickness formed underneath an oil droplet containing only decane molecules and a mixture of decane and nonylphenol (complex oil). Interestingly, the same group proposed the opposite trend while discussing DLE in light of thin film thermodynamics reporting an increase in the film thickness as salinity decreases [188, 189].

The double layer characteristics have been investigated microscopically. Bourg and Sposito (2011) studied the characteristics of the electric double layer for a Smectite surface in the presence of aqueous solutions with varying ionic strength [22].

They concluded that the location of the adsorption planes is independent of both the ionic strength and ion type. Recently, Underwood et al. (2015) investigated double layer expansion, multicomponent ionic exchange and pH effects using Smectite basal planes [24]. However, they refuted DLE as one of the mechanisms affecting the performance of LSWF where they argued that the electrical field strength originating from the charged surface is not affected by the aqueous phase salinity. The double layer characteristics for varying ionic strengths and its impact on LSWF is the focus of this study. The rest of this chapter is organized as follows; the methodology section presents the molecular structures and model setup. The force fields and the analysis tools utilized in this work are detailed. The results section includes the molecular species distribution in varying ionic strength mediums. In addition, both the screening functions and the electrical potential are discussed.

5.2 Methodology

5.2.1 Molecular Structures

Two clay minerals, montmorillonite and kaolinite, are selected to investigate both the surface layer charge and structure in terms of its impact on species distribution. montmorillonite is a 2:1 clay mineral which possesses permanent charge due to the octahedral substitution of one aluminum atom with a magnesium atom. With chemical formula $[Al_3Mg_1][Si_8O_{20}](OH)_4$, montmorillonite has an octahedral layer sandwiched between two siloxane layers. On the other hand, kaolinite is a 1:1 neutral clay mineral with alternating octahedral layer, a gibbsite-like, tetrahedral layer, and siloxane. With chemical formula $Al_2Si_2O_5(OH)_4$, kaolinite possesses both hydrophobic and hydrophilic surfaces. Both unit cells are obtained from the American

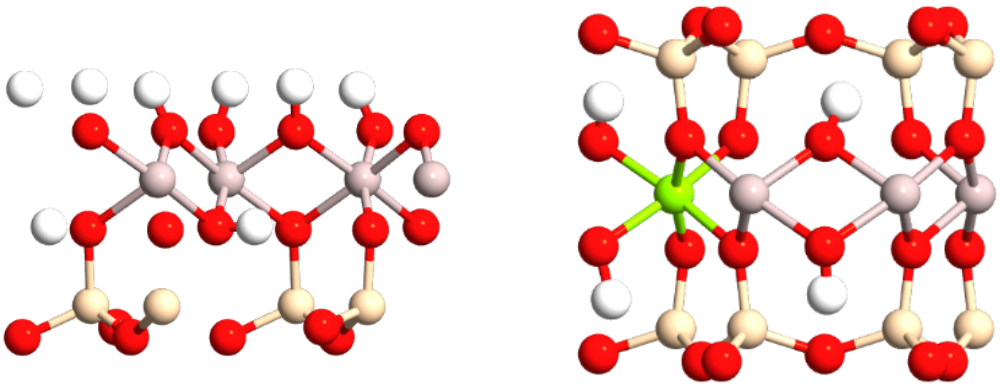

(a) (b)

Figure 5.2: Unit cell structure; a) kaolinite b) montmorillonite (color code: white Hydrogen, red (Oxygen), light green (Magnesium), light yellow (Silicon) and light pink (Aluminum)

mineralogical database [190], previously employed in several molecular simulation studies and are presented in **Figure 5.2** [30, 25, 24, 191].

5.2.2 Model Setup

A supercell of 12 x 7 unit cells is constructed to create the substrate with dimensions around 6 x 6 nm. This substrate is placed in contact with a water box containing a given concentrations of ions. The neutrality of the system is maintained where counter ions are added to compensate for the montmorillonites permanent charge. The system is relaxed for 50 ps using the microcanonical ensemble (NVE) with a 0.1 limit where the langevin thermostat is employed [191]. After that, the simulation is performed for 25 ns using the canonical ensemble (NVT) where a 330 K thermostat is used. A periodic boundary condition is applied in the X and Y directions while a virtual wall is imposed in the Z direction. Both Avogadro and Moltemplate software are utilized to prepare the simulation data file [63]. OVITO software is used for visualization [64].

5.2.3 Simulation Details

Atomistic simulation is performed using an open-source software, LAMMPS [61]. Clayff force field is used to model both the clay minerals and ions [192]. This force field have been used extensively to model the interactions of clay minerals [28, 104, 193, 194, 195, 196]. SPCE is used to model water molecules [197]. Particle-Particle Particle Mesh (PPPM) is used with an accuracy of 1×10^{-4} to evaluate both short- and long-range interactions [198]. Slab boundary condition is used to limit the periodicity in the vertical directions. Lorentz-Berthelot mixing rule is used to estimate cross interactions between the unlike atoms. Lennard Jones interactions are smoothly shifted to zero at 12 Å. Although, the coulombic interactions have the same cutoff, the interactions outside the cutoff are not neglected and a damping factor based on kspace-style is used.

5.2.4 Analysis

The spatial distribution of the charge across the simulation box is estimated where the summation of both the partial charges of water and the charges of ions and surfaces are included. The integration of this charge distribution represents the electrical field induced by the surface charge [199]. The integration of the electrical field would result in the electric potential across the system. Both the charge and molecular species distribution are based on the last 5 ns of the simulation. A screening function is proposed by Bourg and Sposito to quantify the surface charge compensation and is utilized in our work [22]. This function is estimated by cumulatively summing the charges across the surface while considering the surface charge. The film thickness estimated from molecular simulation was based on the electric potential where the end of the diffuse layer is selected when the potential

decay is stable. The interaction energy across Z-direction is estimated by dividing the aqueous solution to bins with width of 1 Å. Then, the interaction between the surface and the bin atoms is calculated.

5.3 Results

In this section, the distribution of ions and water molecules is discussed for both Na-montmorillonite and kaolinite. In addition, the screening function, electric field and electric potential for different systems are estimated and analyzed. Besides, the film thickness from molecular simulation and experimental measurements are compared. Finally, the interactions energy between the surface and the aqueous solution is discussed.

5.3.1 Molecular Species Distribution

The structure of both the solvent and ions in contact with the surface is highly impacted by that surface. The distribution of the molecular species near the montmorillonite surface is presented in **Figure 5.3** & **Figure 5.4**. The distribution of the water molecules shows layering structure near the surface where four peaks (layers) are observed. The amplitude of the first two peaks is affected by increasing the salinity, where a reduction is observed for higher salinities. On the other hand, the amplitude of the remaining peaks is independent of water salinity. The location of the first counter-ion peak is preceding the water peak. In addition, the location of the first ion peak is independent of the initial configuration as shown in **Figure 5.4** where the dynamics of the two systems are presented; one where the counter-ions are placed far from the surface and one where the counter-ions are placed close to the surface. Interestingly, both systems formed a full layer of counter-ions near the

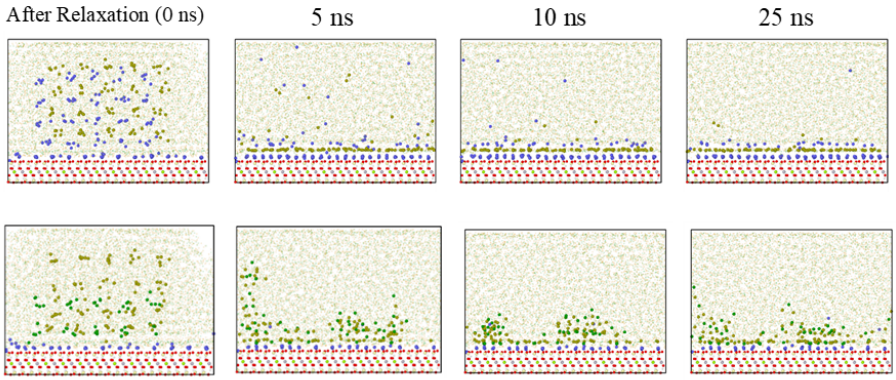

Figure 5.3: Snapshots of montmorillonite in contact with water having 1.2 molar of chloride ion: the first row is Na-montmorillonite with NaCl salt, and the second raw represent Na-montmorillonite with $CaCl_2$ salt. The water molecules are faded for clarity purpose. The color code is Sodium ion is blue, chloride ion is dark yellow and Calcium ion is dark green

surface which assures that the location of the ion peaks is independent of the initial configuration.

The structure of the electric double layer is usually described by defining adsorption planes. Macroscopically, these planes are used as defining boundaries between the behaviors in both the stern and diffuse layers. Our results show that the location of the adsorption planes is independent of the ionic strength. This observation is consistent with several molecular simulation studies. However, this observation on its own does not refute the DLE mechanism, given that DLE is more concerned with the overlap between the diffuse layers.

Figure 5.6 and **Figure 5.7** present the molecular species distribution for kaolinite where the layering of both water and ions is more clearly observed for the gibbsite-like surface compared to the siloxane surface. Interestingly, the nature of the advancing ion is dependent on the surface. While chloride ions are closer to the gibbsite-like surface, siloxane surface attracts more sodium ions. On the contrary to the charged surface, the water peak is preceding the ions peak for a neutral surface.

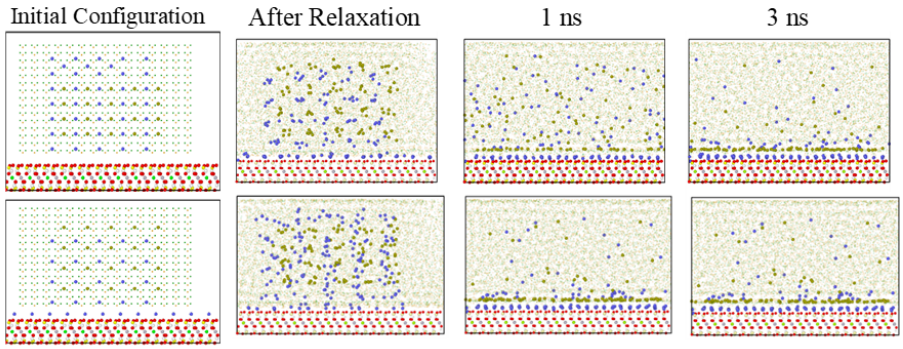

Figure 5.4: Snapshots of Na-montmorillonite in contact with water having 1.2 M of NaCl to show that the location of the adsorbed ions is independent of the initial configuration: The first row represents the system where the counter-ions is placed far from the surface and the second row represents the system where the surface charge is saturated completely by a layer of counter-ions initially located advancing the water layer. The water molecules are faded for clarity purposes. Color code: sodium ion is blue; chloride ion is dark yellow and calcium ion is dark green.

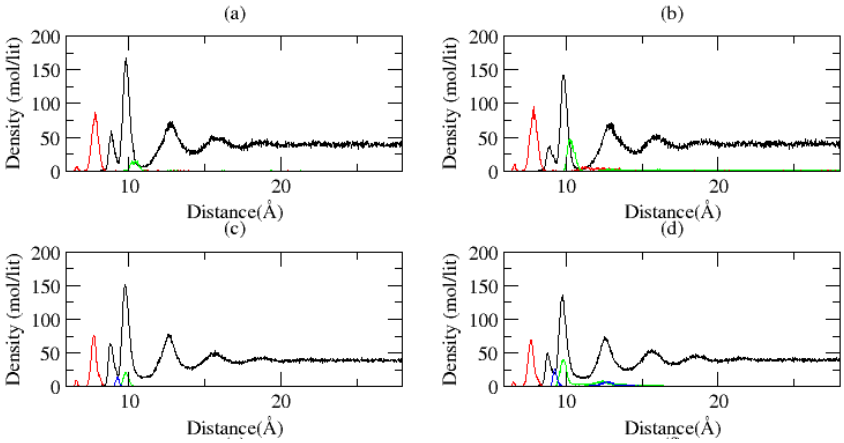

Figure 5.5: Molecular Species distribution; the left and right column represent low (0.3 mol_{cl}/lit) and high (1.2 mol_{cl}/lit) salinity systems respectively: the rows indicate the Na-montmorillonite with $NaCl_2$ and Na-montmorillonite with $CaCl_2$ and respectively. Color code: water (oxygen atom) is black, red is Sodium ion, green is chlorine ion and blue is Calcium ion.

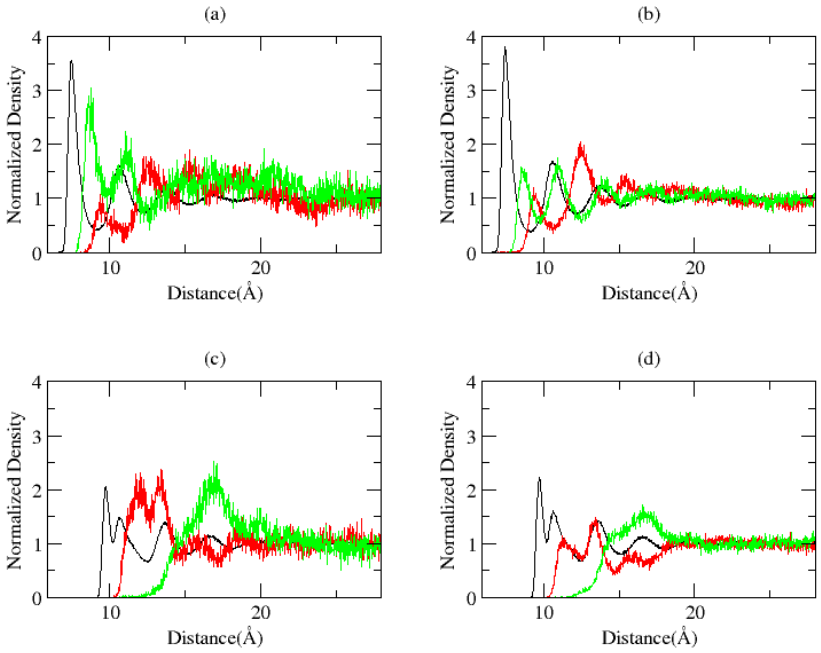

Figure 5.6: Molecular Species distribution; the left and right column represent low (0.3 mol_{cl}/lit) and high (1.2 mol_{cl}/lit) salinity systems respectively: the rows indicate the kaolinite (gibbsite) and kaolinite (siloxane) systems respectively. Color code: water (oxygen atom) is black, red is Sodium ion and green is chlorine ion.

This behavior could be understood considering the interplay between the surface-ion attraction and the ion hydration shell. For charged surfaces like montmorillonite, the surface-ion attraction is strong enough to remove water molecules from the hydration shell resulting in an ion peak preceding the water peak. However, for neutral surfaces like kaolinite, the opposite holds true.

5.3.2 Screening Function

The screening function represents the accumulation of the ions near the surface as shown in **Figure 5.8**. Charge inversion is observed for all the systems. For montmorillonite, the impact of salinity on the screening function is more pronounced for divalent ions compared to the monovalent ones. Whereas a positive relationship

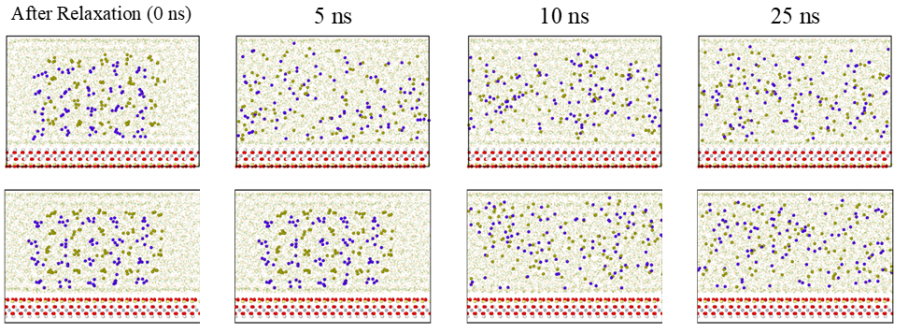

Figure 5.7: Snapshots of kaolinite in contact with water having 1.2 molar of chloride ion: the first row represents the gibbsite-like surface of kaolinite and the second row represents siloxane surface. The water molecules are faded for clarity purpose.The color code is Sodium ion is blue and chloride ion is dark yellow.

between the salinity and the peak amplitude is observed for NaCl, the opposite is observed for $CaCl_2$. Without the electrostatic attractions that are present in the case of a charged montmorillonite substrate, kaolinite surfaces still manage to a lesser degree to induce charge distribution near them. Whereas both kaolinite surfaces attract water molecules to a higher degree than the ions as shown in **Figure 5.6**, the orientation of the water molecules affects the charge distribution near the siloxane surface more than the gibbsite-like surface as shown in **Figure 5.8c-d**. For the gibbsite-like surface, the chloride ions attraction to the hydroxyl groups in the surface results in an accumulation of the negative charge near the surface which is screened by the preceding sodium ions. This oscillatory behavior lasts for 2 nm (3 layers of alternating positive and negative ions) before it reaches equilibrium. On the other hand, the siloxane surface attracts the sodium ions which promotes the positive charge near the surface. However, the oscillatory behavior is not well structured compared to the gibbsite-like surface.

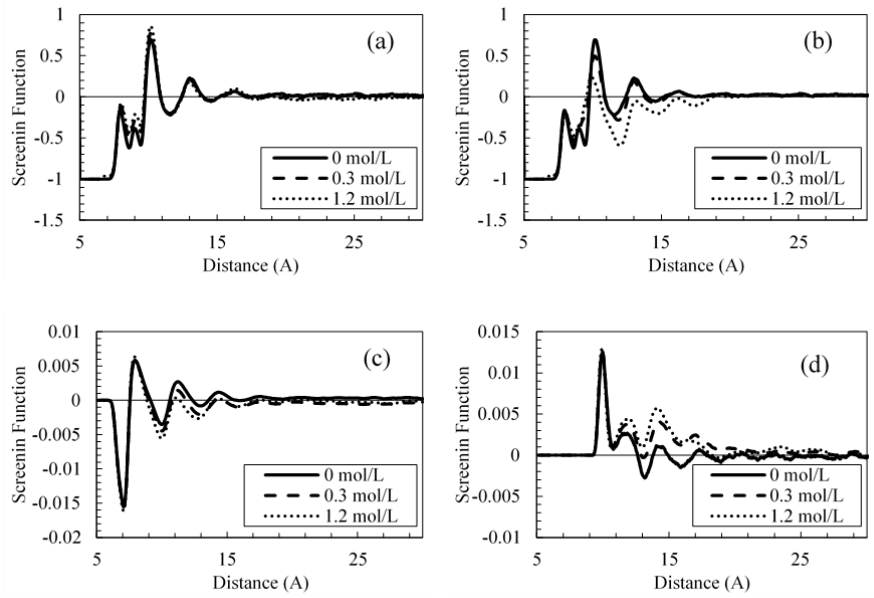

Figure 5.8: Screening function for Na-montmorillonite (NaCl and $CaCl_2$ are a and b respectively) and kaolinite (gibbsite-like and siloxane surface are c and d respectively).

5.3.3 Electric Field and Potential

Zeta-potential is one of the main concepts used to investigate the stability of the colloidal system which is defined as the electrostatic potential at the shear (slip) plane [200]. However, Predota et al. investigated the relation between the molecular nature of the electrostatic potential and the macroscopic concept of Zeta-potential where they suggested that the oversimplified Zeta-potential is not applicable at the molecular scale [201]. The shear plane whose potential is considered as Zeta-potential is defined as the plane separating the mobile and immobile water. It is not feasible to pick a location for the shear plan knowing that water layers near the surface could not be considered immobile since they are proved to possess non-negligible diffusion coeffiencints [22, 202, 203].

According to the stern model, the surface potential could be monotonically de-

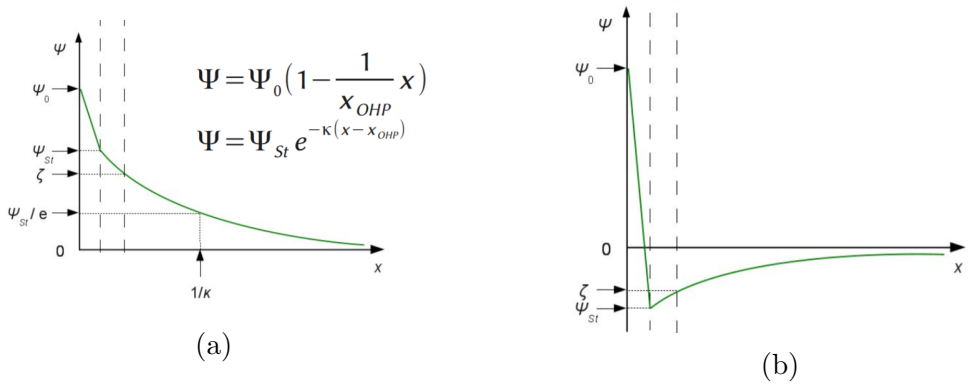

Figure 5.9: Schematic representation of the electrostatic potential according to Stern model: a) the normal b) the charge inversion.[205]

creasing as the distance from the surface increases [204]. In addition, the slope of this relation is constantly decreasing as well. This slope is steep between the surface and the Outer Helmholtz Plane (OHP) and exponentially decaying in the diffuse layer as shown in **Figure 5.9a**. However, charge inversion would result in a reversed behavior as shown in **Figure 5.9b**.

In our simulations, we have specified the charge and estimated the electric field and potential induced. For the charged montmorillonite, the electric field is initiated by the surface charge which both attract positively-charged ions and orient the water molecules in a way to dissipate the electric field as shown in **Figure 5.10a-c**. On the contrary, the kaolinite surfaces induce an electric field to a lesser degree as shown in **Figure 5.10e-g**. Based on the nature of the kaolinite surface, the electric field induced is different. In addition, for the same surface as Na-montmorillonite, the electric field differs based on the ion valence.

The second integration of the charge distribution would be the electric potential which is presented in **Figure 5.10**. For a charged surface like montmorillonite, multiple charge inversions are observed in case of monovalent cations and lower concertation of divalent cations; while a steady decay is observed in case of high

concentration of divalent ions. For a neutral surface like kaolinite, lower potentials are observed. In case of the gibbsite-like surface, the potential in the case of low salinity shows a different signature than that of fresh water and high salinity cases. This could be due to offset contributions for both water and ions to the total potential field. In case of the siloxane surface presented in **Figure 5.10h**, larger electric potential is induced for higher salinity with small oscillations.

The contribution of the water molecules and ions to the total electric potential is presented in **Figure 5.11**. Both water and ions are adversely contributing to the total electric potential. In addition, the water is contributing in an oscillatory behavior reflecting the layering of the medium where the oscillations are propagating for more than 15 Å away from the surface for both fresh and high salinity cases and 10 Å for low salinity. On the contrary, the ions are contributing more smoothly. However, a charge inversion is observed for the low salinity case and a double charge inversion is observed for the high salinity case.

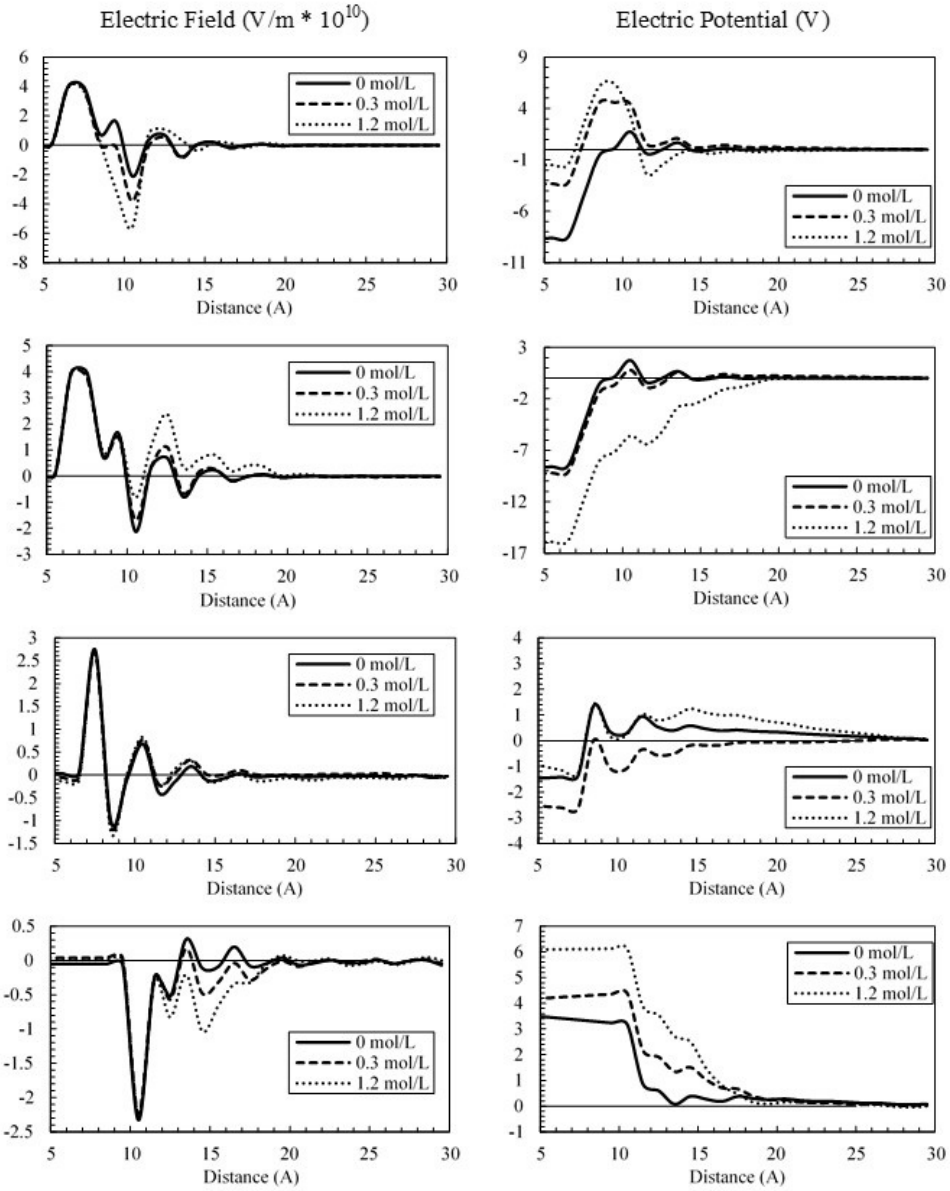

Figure 5.10: Electric potential and electric field for Na-montmorillonite with NaCl (a & b), Na montmorillonite with $CaCl_2$ (c & d), gibbsite-like kaolinite surface with NaCl (e & f), the siloxane kaolinite surface with NaCl (g & h).

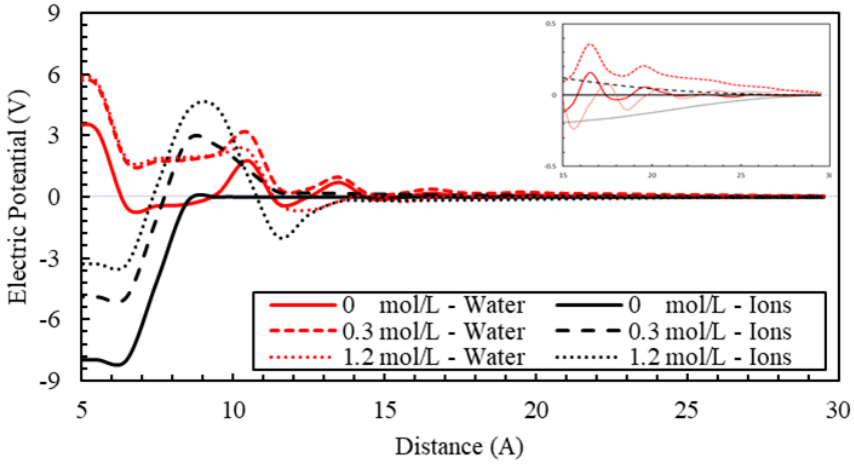

Figure 5.11: Water and ions contributions to the electric potential of NaCl solutions in contact with Na-montmorillonite. The inset graph shows a close look at the potential for distance 15 to 30 Å away from the surface. 0 mol/L refers to the fresh water.

5.3.4 Film Thickness

The advances of thin films thermodynamics developed relations between the wetting film stability and disjoinging pressure and between the film thickness and contact angles [175, 189, 206]. Lee et al. measured the thin film thickness for sandstone and clay as shown in **Figure 5.12** suggesting an expansion of the DL at lower salinities. However, we think it is difficult to deduce this conclusion given the uncertainty involved in the measurements. In addition, the results show that the film dynamics experiences more dynamics in the case of sandstone compared to clay, which is counter-intuitive given that clay surfaces are charged and sandstones are neutral. Apart from the uncertainty and the film dynamics, the expansion of the DL is not monotonic and if we exclude the fresh water from the analysis, the expansion of the DL is ranging from less than 1 Å for NaCl in contact with clay to around 7 Å for $CaCl_2$ in contact with clay. However, the main point from this

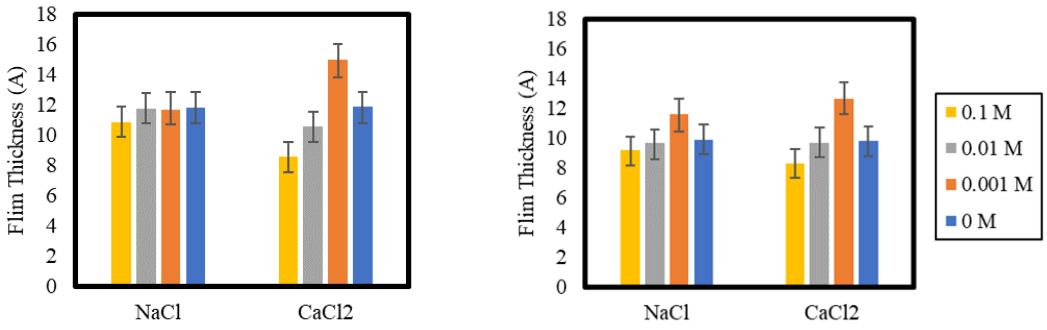

(a) (b)

Figure 5.12: Film thickness of water layer adjacent to the mineral surface for different salinities: a) clay b) sandstone (changed after Lee et. al [191]). We focus on the salts used on our study.

figure is that the thickness of the thin film ranges from 1 to 2 nm. This means that for DLE to be effective, both O/W and W/R interfaces have to be less than 4 nm of each other. Considering the exponential decay of the disjoining pressure with the film thickness, having an overlap between the DL of two interfaces does not mean that the resulting repulsive force is enough to induce a significant change in the wetting nature of the surface. In addition, honoring the fact that pore throat sizes in conventional reservoirs are usually greater than 2 μm [207] and the water saturation usually encountered in conventional reservoirs, it is highly unlikely to find a situation where both O/W and W/R interfaces are confined in less than 4 nm.

The film thickness estimated from our molecular simulation results is presented in **Figure 5.13**. Interestingly, the diffuse layer shrinks for all the systems as salinity decreases from high to low cases. However, an expansion is observed when fresh water is used for all systems except for Na-montmorillonite in contact with NaCl. This behavior might be counterintuitive to our macroscopic understanding of electric double layer characteristics. However, this trend is previously produced

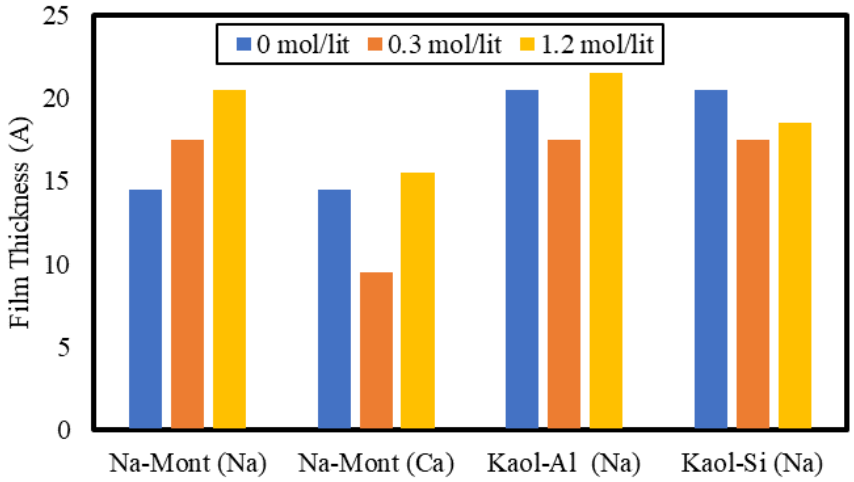

Figure 5.13: Film thickness from molecular simulation for montmorillonite with NaCl, montmorillonite with $CaCl_2$, kaolinite (gibbsite like surface) with NaCl and kaolinite (siloxane surface) with NaCl. The concentration refers to the chloride ions (roughly in our simulation 0, 0.3 and 1.2 mol/lit equal to 0, 2 and 10 wt.% respectively)

in molecular simulation studies. These observations are supported by considering the shortcomings that have been raised about the validity of DLVO at small scales,[173, 175, 186, 208, 209, 210, 211] and the assumptions involved [212]. Given that there is limited expansion in the diffuse layer (according to the experimental measurements presented in **Figure 5.12**) or shrinkage (according to our molecular simulation presented in **Figure 5.13**), the premise of DLE is unwarranted.

5.3.5 Interaction Energy

The interaction energy between the surface and the solvent across the Z-direction (perpendicular to the surface) is estimated and presented in **Figure 5.14** Limited impact for salinity is observed on the interaction energy for the neutral surfaces. However, a pronounced impact is observed for charged surfaces where a larger energy barrier with a shift in the peak location with increasing salinity is observed in the

case of monovalent ions. On the other hand, for a charged surface in contact with divalent ions, limited impact is observed for the peak amplitude. However, the shift in the peak location is still noticeable. The repulsive interaction observed in **Figure 5.14c** for the gibbsite-like surface of kaolinite suggests the oil-wetting nature of this surface which is consistent with both experimental and molecular simulation literature [25, 213, 214].

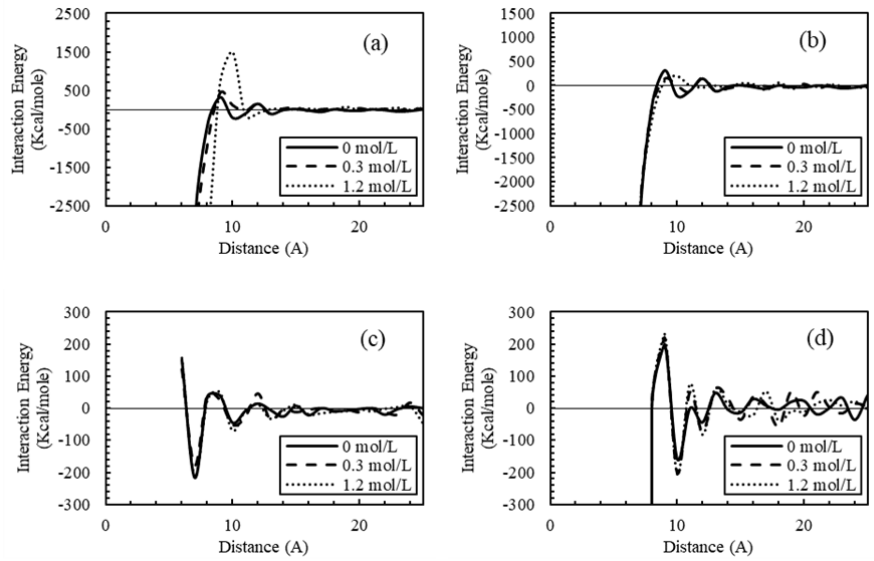

Figure 5.14: Interaction energy between surface and solvent molecules (including ions) along the Z direction (perpendicular to the surface): a) Na-montmorillonite with NaCl, b) Na-montmorillonite with $CaCl_2$, c) Gibbsite-like kaolinite surface with NaCl and d) the siloxane kaolinite with NaCl

5.4 Conclusions

This study was aimed at investigating the impact of water salinity on the microscopic level near the solid surface. Simulations were performed for two types of surfaces and two types of ions at two concentrations. The conclusions of the work presented in this paper are outlined below:

- Based on our analysis and the literature review, there is limited evidence supporting the DLE mechanism.

- In the cases where salinity had an impact on the system, the change is in the electric field and the potential induced, with very little impact on the thickness of that layer.

- The two neutral surfaces of kaolinite attract different types of ions, with the gibbsite-like surface attracting the negatively-charged chloride ions and the siloxane surface attracting the positively charged sodium ions, with no disturbance of the hydration layer in both cases, unlike the case for the charged montmorillonite surface.

- The behavior of monovalent and divalent ions was not drastically different, with very little amplified observations in certain cases such as an elevated interaction energy peak for the monovalent ions case for high salinity, and a more pronounced impact of salinity on the screening function and electric potential for the case of divalent ions.

Chapter 6

Conclusions and Future Work

This chapter summarizes the main findings along with recommendations for future work.

6.1 Main Findings

Molecular simulation provides insights in petroleum engineering, and should be used to tackle both seasoned and emerging challenges in petroleum engineering. Additionally, the main conclusions from this study are presented below:

- We have performed a systematic molecular simulation study to investigate the density behavior of various binary oil-gas mixtures to investigate the factors at play in the CO_2-oil density behavior. We found that the existing hypotheses in published literature attempting to explain the CO_2-oil density behavior, namely the columbic-induced dipole interactions and the possible stretching of alkane molecules, do not stand the test of in-depth analysis of molecular interactions and fail to account for the density behavior. In addition, the impact of CO_2 on increasing the density of the binary mixture is more pronounced in

heavier alkanes. The MD simulation results show a closer packing of the mixtures that include CO_2 compared to mixtures that include C3, which explains the higher density observed. This packing seems to be highly correlated with the molecular size of the gas than with any interaction between the gas and the heavier hydrocarbon molecules.

- The dependence of asphaltene aggregation dynamics on the physical conditions and composition of the system. We found that the molecular interactions present in the system determine the dynamics of asphaltene molecules. The stronger the asphaltene self-interactions are, the more prone it is to aggregate. Favourable solvent/asphaltene interactions could replace the asphaltene self-interactions and lead to a dissolved state for the asphaltene. The relative value of LJ interactions seems to be a good predictor of solubility. It is important to note that the state of CO_2 is a crucial factor for determining its characteristics as an asphaltene solvent. Continental asphaltene could be dissolved in supercritical CO_2 mixtures, in contrast to archipelago asphaltene which forms larger aggregates. In addition, liquid CO_2 could be considered an asphaltene precipitator for both structures. The continental aggregate size in CO_2 correlates negatively with temperature, while a non-monotonic effect of pressure on aggregation is observed in the case of heptane. Surprisingly, the presence of resin has limited impact on the aggregation propensity of asphaltene in CO_2. Furthermore, we observed that continental asphaltenes form diffusive aggregates containing more than 4 molecules with R_G of 4 nm in oil mixtures. This aggregate grows to take in all asphaltenes in the mixtures and become denser with half the R_G when 30 wt% C1 is introduced to the mixture. However, when a similar percentage of CO_2 is introduced, a slight reduction

in R_G is observed. Depending on the structure of the asphaltene molecule, methane injection can be more of a problem than carbon dioxide injection when it comes to the potential for precipitating asphaltenes.

- Finally, the impact of salinity on water dynamics near the solid surface is investigated on the microscopic level. Based on my analysis, there is limited evidence supporting the double layer expansion mechanism. In the cases where salinity had an impact on the system, the change is in the electric field and the potential induced, with very little impact on the thickness of that layer. The two neutral surfaces of kaolinite attract different types of ions, with the gibbsite-like surface attracting the negatively-charged chloride ions and the siloxane surface attracting the positively charged sodium ions, with no disturbance of the hydration layer in both cases, unlike the case for the charged montmorillonite surface. The behavior of monovalent and divalent ions was not drastically different, with very little amplified observations in certain cases such as an elevated interaction energy peak for the monovalent ions case for high salinity, and a more pronounced impact of salinity on the screening function and electric potential for the case of divalent ions.

6.2 Future Work

In this section, we would like to suggest some extensions of the current work.

The close proximity between the molecular simulation and EoS predictions in chapter 3 suggests that MD could provide a reliable tool to tune the EoS parameters when the experimental work is not accessible. This might include the estimation of the binary interaction coefficients. Another extension could be considering other properties like viscosity, diffusion and solubility. After that, considering the con-

finement impact on those properties would be the natural extension and major contribution to the literature.

As demonstrated in chapter 4, molecular simulation could capture the dynamics of asphaltene molecules. The natural extension of this observation is to use molecular simulation to assess the performance of the proposed inhibitors for asphaltene. In addition, the quantification of the interactions between the asphaltene and the solvent could provide a reference for the binary coefficients of the EoS. Another dimension would be to further investigate the impact of asphaltene/resin ratio.

The optimization of low-salinity waterflooding is a multifaceted challenge where involving several physicochemical mechanisms are involved. In chapter 5, we have presented an observation that challenges our current understanding about the dynamics of double layer. Further research is required towards deep understanding of the phenomenon. In addition, we have illustrated the ability of MD to capture the wettability of the mineral surface. This could be used to provide a microscopic measure of the surface wettability. At the same time, it calls for bridges that connect the molecular forces to the current macroscopic measurements like contact angle.

Appendices

I have included two of my experimental studies that have motivated us to embark on molecular simulation journey. Appendix A discusses the impact of salinity on the water dynamics and formation strength in shale formations and it was the motivation of the work presented in chapter 5. On the other hand, appendix B evaluates the impact of the asphaltene deposition on the fluid flow and field productivity in sandstones. This work was the main motivation for the work presented in chapter 4.

Appendix A

Salinity Impact on Imbibition and Formation Strength in Shale

A.1 Abstract

Spontaneous imbibition is one of the mechanisms proposed to reveal the fate of fluids used during fracturing operations in shale reservoirs. However, the influence of salinity and mineralogy on the imbibition kinetics are not yet well-understood. We performed imbibition experiments on samples collected from Woodford and Caney shale outcrops with slick water having salinities up to 15 wt% KCl. The impact of salinity on imbibition rate and capacity shows a different trend for samples of varying mineralogy. A correlation between the carbonate to clay ratio and the imbibition rate is observed. This ratio, as well as illite content were linked to be factors affecting the impact of salinity on imbibition. This correlation suggests a maximum volume of imbibition at a ratio of 1.5. The impact of salinity on formation strength seems to correlate with the amount of siderite and anhydrite present in the rock. It is worth noting that the swelling of the expansive clay minerals could

mask the imbibition signature of the samples where the apparent weight is used to estimate the liquid uptake. This is mainly apparent in the later stages when the bulk volume expansion can outweigh the liquid uptake, however, this effect does not reach the level of impacting the trends and correlations observed in this study.

A.2 Introduction

It has been two decades since the beginning of the shale boom, and the fate of the fracturing fluid is still a controversial issue [215]. The mechanisms of fracturing fluid imbibition and their impact on well productivity and formation strength are the focus of several research groups around the world [216, 217, 218, 219, 220, 221, 222, 223] such as the Lower Silurian Longmaxi formation in China [216], Marcellus and Haynesville gas shale in Pennsylvania and Louisiana [220], Horn River Basin [221, 222] in Canada. The unique characteristics of shale along with the unlike-expected experimental observations have challenged the petroleum industry for years [219, 224, 225]. Many authors suggest that spontaneous imbibition is a key factor explaining the low load recovery, where they relate the extended shut-in time to the enhanced early well performance by proposing the suction of fracturing water to the matrix as a cleaning mechanism of the flooded fractures [226].

The preferential adsorption of water is considered as one of the driving mechanisms of water intake in clay-rich shale based on studies of samples from the Horn River basin [227]. Dehghanpour et al., using cores from Simpson, Muskwa and Otter Part formation, observe that water adsorption enhances water intake in shale regardless of the swelling nature of that shale [228]. This observation could explain the superior imbibition of water observed in oil-wet shale cores [229]. In addition, they found that this adsorption is highly impacted by fluid salinity and viscosity,

as well as the orientation of the bedding planes, especially in one-dimensional imbibition experiments where the choice of the surface exposed to imbibition should be carefully considered. Interestingly, the stress accompanying the adsorption of water in clay pores might induce micro fractures improving the rock conductivity.

Fracturing fluid imbibition might also induce permeability impairment. Yan et al. experimentally elucidate that this impairment is a lithology-specific property where a higher, more permanent damage is observed with shale compared to tight sandstones [230]. The source of these core samples was not specific. The main cause for this permeability reduction are the rock-fluid interactions including the swelling of clays and the scale precipitations. On the other hand, favorable rock-fluid interactions, dissolution, could be stimulated by using sea water as the fracturing fluid where promising well performance is observed [231, 84].

The native state of rock samples enacts the imbibition behavior. The connate water saturation highly controls both the imbibition rate and capacity in conventional rocks.19, 20 However, its impact would be minimal in shale where in-situ excessive drying leaves the initial saturation in a sub-irreducible state.15 The salinity and composition of connate water determine both the type of geochemical interactions stimulated and the direction of osmatic flow [84, 232].

The physiochemical process controlling liquid uptake in shale includes capillary and osmosis hydration [233]. The capillary suction is controlled by pore morphology and mineralogy, and consequently wettability [234, 235]. On the other hand, the osmatic flow is driven by the salinity contrast between the formation brine and the fracturing fluid. The incorporation of both mechanism is critical in properly modelling water dynamics in both fracture [226, 236, 237, 162] and matrix imbibition [232]. Li et al. integrate the two mechanism to develop a one-dimensional imbibition model for shale using samples from the Horn River basin [238].

The dependence of the rock wettability on water composition adds another level of complexity to the imbibition dynamics [239, 240, 241, 242, 243]. Aslan et al. experimentally demonstrate the non-monotonicity behavior of rock wettability with water salinity using smooth surfaces of quartz, mica and calcite [244]. In the same vein, Valluri et al. suggest an optimum salinity condition where any deviation from it would result in enhancing the rock oil-wetting nature [245]. The surface charge of the pore wall determines the extent of wettability variations with water composition. Interestingly, the lower Zeta potential values obtained for higher salt concentrations suggest a more significant role for the surface charge reversal, or multicomponent ion exchange, as wettability control mechanisms [245].

Usually rock wettability could be described by the contact angle. However, contradicting results have been reported between imbibition and contact angles in unconventional rocks where the bulk samples exhibit a higher water intake despite the oil-wetting nature of those samples as indicated by contact angle measurements [246]. These results cast doubts on the reliability of the contact angle as a measure of the wettability in shale. However, the double layer thickness and stability could be used to describe of the wettability state of the rock [247].

The complexity of water imbibition in shale pores necessitates a microscopic-level investigation. Hu et al. correlate the water dynamics and ions distribution with pore mineralogy for carbonates versus organics using Molecular Dynamics (MD) simulations [248]. Yang et al. attribute the higher oil uptake in shale to the fast imbibition of oil in organic pores [249]. In addition, the deviation between the capillary pressure macroscopically-measured and microscopically-estimated was evident experimentally, and varied up to one order of magnitude [250].

The imbibition process could be described by the imbibition rate and capacity. While the former marks the dynamic nature of the flow, the latter quantifies the

relation between the connected pore network and the driving forces associated. Hu et al. attributed the imbibition rate to the connectivity of the pore network where three main categories are identified based on early imbibition slope with values of: 0.26, 0.5 and 0.26 to 0.5 mm/min representing poor, well, and moderately-connected pore bodies [251]. The imbibition rate is correlated with the porosity, permeability and clay content of the rock in addition to the fracturing fluid properties [252]. Furthermore, the imbibition capacity is correlated with well logs readings and sample mineralogy [228].

In this paper, the impact of salinity on fracturing fluid dynamics and formation strength is investigated experimentally. This paper is organized as follows: the materials and methods section outlines the rock samples used, their mineralogy and dimensions, in addition to the properties of fluids and the equipment used. The results section analyzes the imbibition experiments in terms of rate, capacity and formation softening. In addition, the salinity impact is correlated with the formation mineralogy whenever needed. Finally, the conclusions summarize the main findings from this work.

A.3 Materials and Methods

Outcrop samples from Woodford and Caney formations were collected. Six groups, namely K, D, T, E, W and C, were identified and labeled. The mineralogy of the samples, in weight%, was measured using the Fourier Transform Infrared Spectroscopy, FITR, and is presented in Fig. A.1 and Table A.1. The dimensions of the samples used are reported in Table A.2. While C, K and W samples are cubic ones, the rest are cylindrical. All samples were dried for 24 hrs. at 100C (till no weight change was observed). While D, T, E and W samples are Dolomite-rich, C and

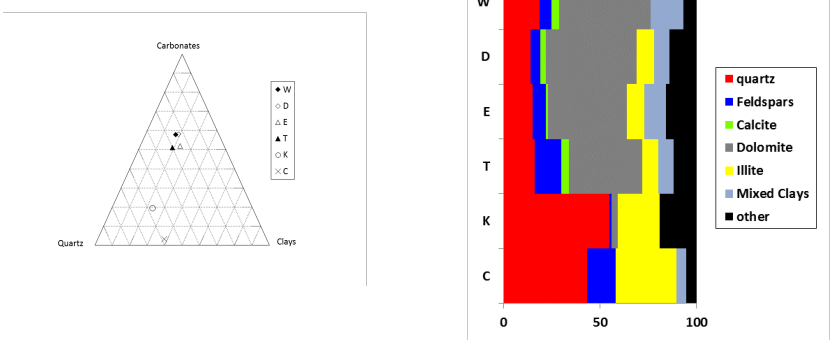

Figure A.1: The FTIR mineralogy of samples used. Data is in weight%

Table A.1: FTIR mineralogy of outcrop shale samples used in this study, in weight%

	Quartz	Feldspar	Carbonates			Clays				Albite	Anhydrite	Apatite	Aragonite
			Calcite	Dolomite	Siderite	Illite	Kaolinite	Mixed Clays	Chlorite				
W	19	6	4	47	5	0	0	17	0	0	1	0	0
D	14	5	3	47	6	11	0	8	0	4	2	0	0
E	15	7	1	41	6	9	2	11	1	3	3	0	1
T	16	14	4	38	6	8	1	8	2	0	3	0	0
K	55	1	0	3	9	22	1	0	0	0	4	2	3
C	43	15	0	0	3	31	1	5	0	0	1	0	0

K are Quartz-rich. Porosity for W and C formations was measured using helium expansion. The porosity for K, D, T and E samples was estimated using mercury injection. Since this is a destructive method of measurement, only was sample from each block of rock was used to perform this set of measurements. Porosity data are reported in Table 2. Mercury injection data shows that the D, T and E samples had an average pore throat size of 3 to 6 nm, while sample K had an average pore throat size of 400 nm. While it took over 4000 psi of pressure for mercury injection to be initiated in samples D, T and E, around 200 psi were enough for sample K indicating the larger pores and higher permeability for this sample.

Slick water samples were prepared with different salinities and kept hydrating for 4 hrs. before use. 2-Acrylamido-2-methylpropane sulfonic acid was used in a 0.7

Table A.2: Relevant properties of outcrop shale samples used in this study

Salinity (wt.% KCl)	ID	Length (cm)	Width (cm)	Height (cm)	Weight After Drying (g)	Weight after Imbibition (g)	Porosity (%)
0	W9	2.05	2.72	3.42	46.42	47.50	6.31
5	W10	2.18	2.17	3.54	48.10	49.35	
10	W11	2.07	2.03	4.35	65.81	67.38	
15	W12	2.80	2.77	4.16	77.96	79.87	
0	D0*	2.54	2.54	4.49	53.30	54.51	6.46
5	D1*	2.54	2.54	4.49	53.94	55.14	
10	D2*	2.54	2.54	4.51	54.11	55.29	
0	E3*	2.54	2.54	4.14	49.12	50.40	6.32
5	E0*	2.54	2.54	4.10	49.11	50.33	
10	E1*	2.54	2.54	4.14	48.98	50.18	
15	E5*	2.54	2.54	4.13	49.11	50.54	
5	T2*	2.54	2.54	3.80	45.63	46.78	5.58
10	T3*	2.54	2.54	3.78	45.44	46.56	
0	K0*	2.61	2.51	2.52	24.57	29.98	31.41
5	K4*	2.46	2.46	2.53	23.95	29.14	
0	C0	2.40	2.37	3.82	39.00	41.75	20.13
5	C1	2.37	2.80	2.48	33.45	35.80	
10	C2	2.53	2.86	2.40	35.03	37.18	
15	C3	2.40	2.41	2.25	26.99	29.00	

* cylindrical samples with 2.54 cm diameter

wt% concentration as a friction reducer to prepare the base slick water samples to generate a relatively-representative fracturing fluid. The ability of KCl to minimize clay swelling was the reason it was selected in controlling fluid salinity for the purpose of this work, referred to as the fracturing fluid later in the paper. The imbibition setup is composed of a digital scale, a beaker for holding the fracturing fluid and a data acquisition system. The digital scale is used to record the weight of samples which are fully submerged in the fracturing fluid while being held by a nylon thread as shown in Fig. A.2. The weight of the imbibed fluid could be estimated assuming the sample bulk volume remains constant throughout the experiment. Counter-current, unconfined imbibition is performed on fully exposed samples. The ultimate compressive strength of the sample is used to represent the strength of the formation. The compressive strength of the samples is measured after a two-week soaking period in a fracturing fluid with a given salinity. Test Mark Machine is used to measure the

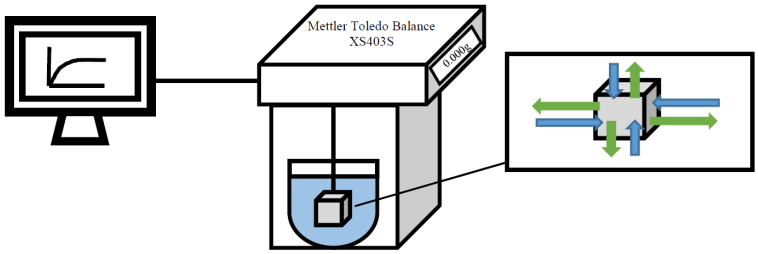

Figure A.2: Imbibition Setup used [85].

compressive strength where a constant loading rate of 0.5 MPa/min is applied until the rock fails. This one done with samples saturated with slick water of varying salinity after the two-week soaking time. Because the behavior of dry rocks is different than that of saturated rocks, it was not possible to add the original rock strength to this data since the samples were obtained in the dry state.

A.4 Results and Discussion

In this section, we analyze the imbibition results in terms of rate and capacity. After that the mineralogy role is discussed where the relation among salinity, mineralogy and both imbibition rate and capacity are deduced. Finally, the formation softening is correlated with sample mineralogy.

A.4.1 Imbibition Rate and Capacity

The results of the spontaneous imbibition experiments can be represented in multiple ways. In our case, we share this data as a plot of the imbibition length in cc/cm^2 as a function of the square root of time in $hr^0.5$. The measured imbibed volume of fluid is normalized with the total external surface area of the sample that is exposed to fluid entry in order to determine the y-coordinate for these plots with minimized

shape and size effect. A higher imbibtion length represents a higher recovery rate.

It has become an accepted knowledge in the petroleum industry that low salinity water enhances the imbibition capacity of the rock by shifting the rock towards more water-wetting and stimulating the adsorption of water into clay layers. However, a reverse behavior is observed in W samples, and a non-monotonic behavior is observed in C and E samples. In addition, a significant improvement in recovery is observed for K samples as salinity decreases, a moderate one is reported for D and a modest one is detected in T samples as shown in Fig. A.3. These results reveal that the extent of recovery enhancement, or suppression, is actually sample-dependent.

The product of capillary pressure and permeability could be constructed from the imbibition data [253, 254]. We used Handys model where the pores are assumed as cylindrical straight capillary tubes [255]. The salinity impact on capillary pressure curves is presented in Fig. A.4. However, attributing the change in imbibition capacity solely to capillary suction might be misleading. Mehana et al. quantified the contact angle of the brine/air/rock system for Woodford and Caney samples with the change in salinity, as well as the decrease in the brine/air surface tension with increasing salinity [237]. However, the range for the change in the contact angles was 15 and the change in the surface tensions was 2 mN/m. This change in the fluid properties could not affect the capillary suction enough to explain the imbibition behavior.

The imbibition rate in our work is represented as the slope of the plot between the imbibition length and the square root of the imbibition time ($hr.^0.5$) on a log-log scale [251, 252]. According to our experimental results, the imbibition in most samples experienced three main characteristic rates: initial, transient and late as presented in Fig. A.5. A Gradual decline in the imbibition rate is expected as the imbibition progress where the capillary forces slow down as the liquid saturation

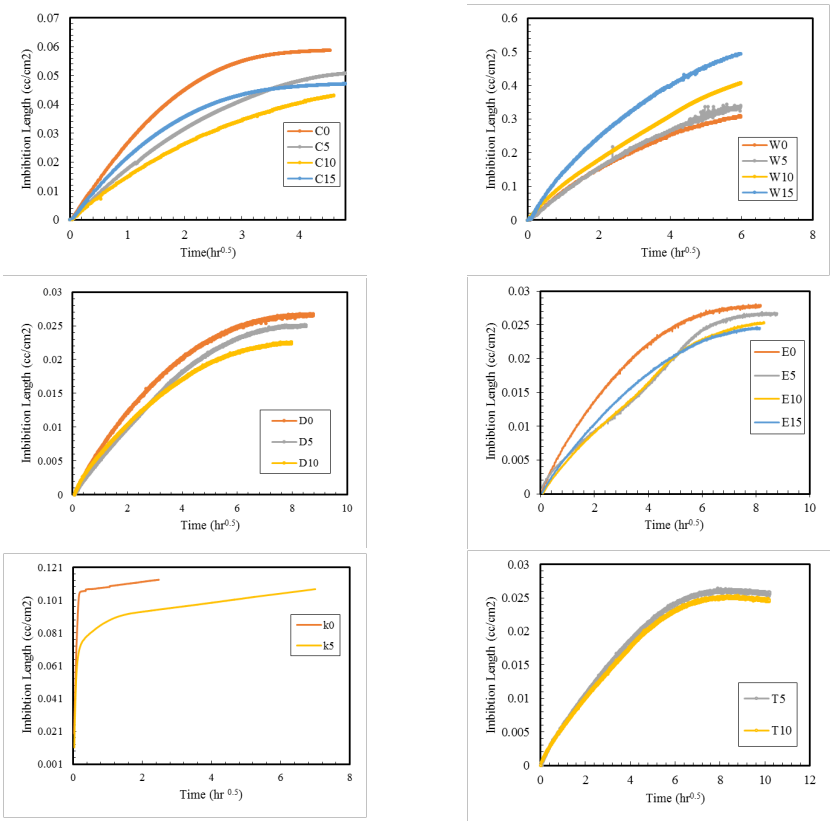

Figure A.3: Normalized imbibed volume versus Time. (C and W adopted from Mehana et al.)[163]

increases [252, 256]. In some cases, the transition from initial to late, equilibrium, stage might be too sharp to experience a transient region as observed in K samples (Fig. A.5c).

Interestingly, negative late rates are reported for the T samples (Fig. A.5d) which could be ascribed to the swelling of clay minerals which would result in bulk volume expansion and in turn less apparent weight. Although the swelling kinetics suggests faster swelling rates [257, 258, 259], the impact of this swelling might be masked by the higher rates in the earlier stages of imbibition.

The results presented in Fig. A.6 represent the normalized imbibed volume for various rock samples at 16 hours of imbibition time. In this plot, we used the porous

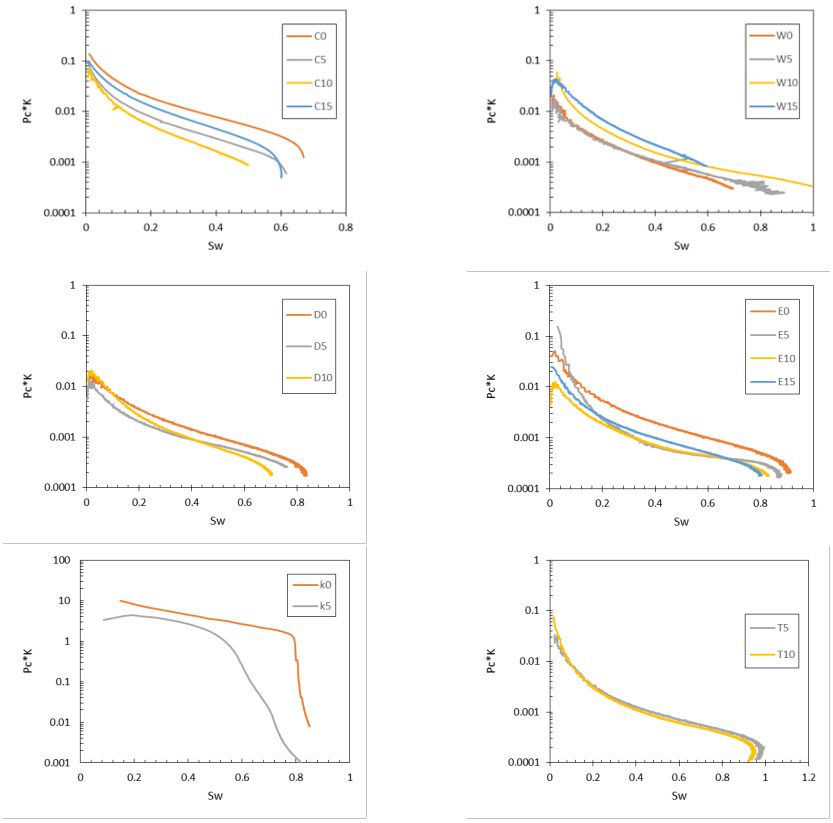

Figure A.4: A plot of the product of capillary pressure and permeability as a function of saturation, derived from the imbibition results (C and W adopted from Mehana et al. [85]).

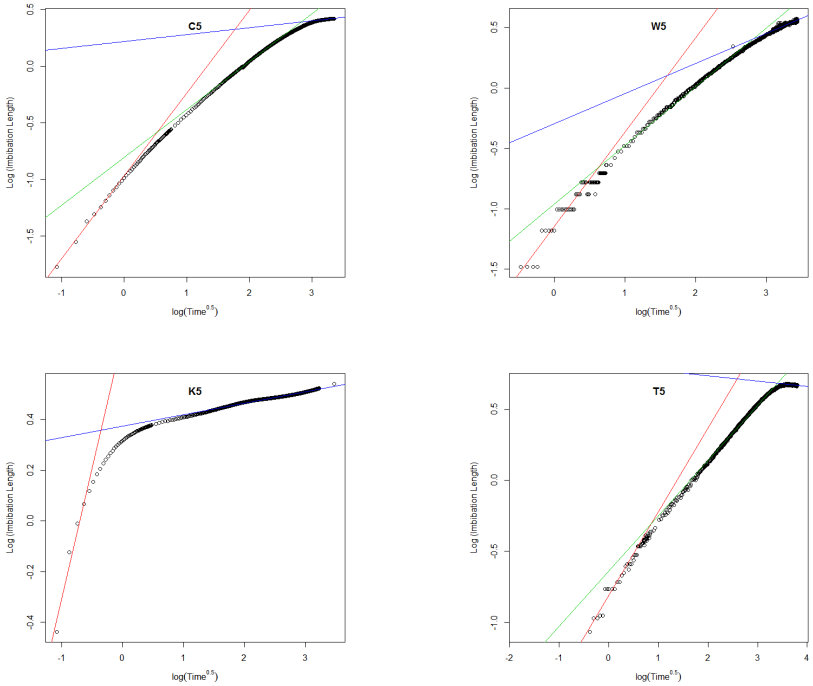

Figure A.5: Imbibition length vs square root of time for 5 wt% salinity samples.

area of the exposed surface in order to generate the normalized imbibed volume. We use this value as an indication of imbibition rate into the rock by comparing the normalized volume imbibed at a fixed imbibition time. The results clearly show a monotonic behavior of imbibition rate for a given rock sample for 0%, 5% and 10% salinity, and a reversal of trend for the 15% salinity. The E samples deviate from this observation, but consulting the imbibition data shows that the results are masked by clay swelling effects. Even with those effects considered, it is clear that for the E sample, the reversal of trend for the 15% salinity case doesnt occur. It is worth noting that although C and K samples are both Quarts-rich, C samples had mostly the lowest normalized imbibed volume value at 16 hours while K samples was second to the highest for a given salinity between all 6 sample types.

Comparing the total imbibition capacity results in a slightly different trend.

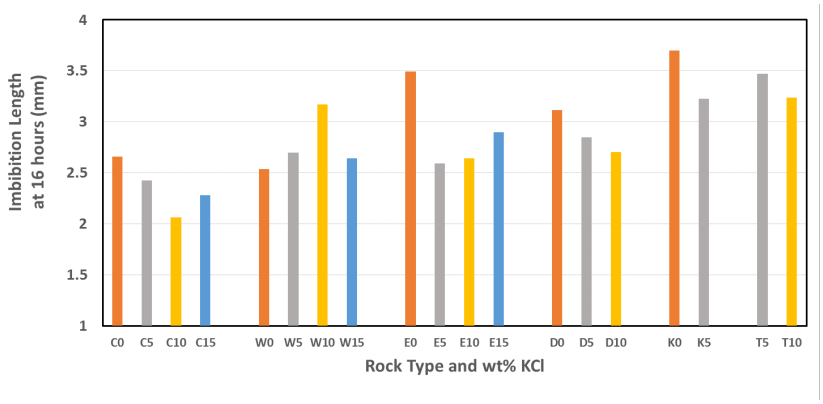

Figure A.6: Normalized imbibition volume for the various rock samples in various fracturing fluids at 16 hours of imbibition time.

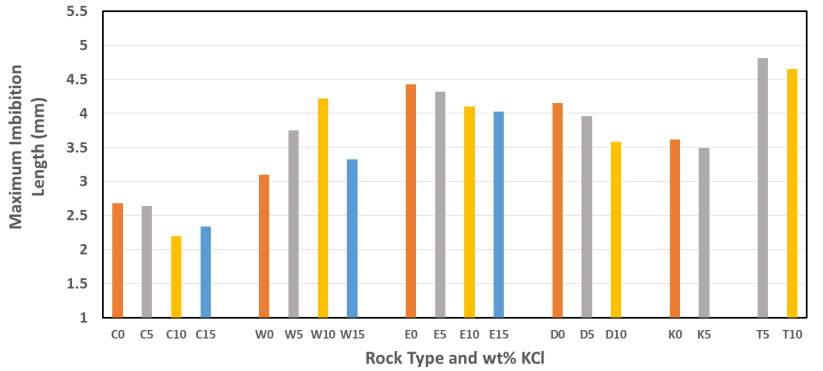

Figure A.7: Maximum recorded imbibition length for the various rock types with the various salinity values used.

Keep in mind that not all the samples reach their maximum imbibition capacity and some of the samples started showing signs of clay swelling. The results are still revealing and comparable within each rock type. We plot in Fig. A.7 the maximum imbibition length recorded for each case. Water adsorption in clays might explain some of the results, to some extent, like the enhanced performance for the deionized water imbibition in samples with clay content. However, KCls ability to suppress clay swelling restricts the impact of this mechanism for saline cases.

Osmosis hydration is usually overlooked when describing water dynamics in reservoir studies. However, this might explain the faster imbibition observed for higher saline cases in E samples, where the rate of imbibition for 15 and 10% cases exceeds the rate for the 5% case in the earlier time. After this initial transient behavior in E samples, the late imbibition capacities are ordered in a manner depicting negative correlation between the water salinity and imbibition capacity. On the other hand, C samples show an interesting trend where the 15% imbibition rate initially exceed that of both 5% and 10%, and towards the end only exceeds the 10% case. This behavior was previously noted in the three forks formation (dolomite-rich) where the distilled water exhibits a performance lower than the low salinity imbibition and higher than the high salinity imbibition [260].

The impact of clay swelling on imbibition data is twofold. First, it is responsible of sample expansion (strain) especially in unconfined imbibition. This expansion affects the buoyancy force involved and in turn results in a decrease in the apparent weight recorded on the scale. This observation might explain the decrease in the calculated imbibed volume during the later stages of imbibition. Zhou et al. reported similar behavior and ascribed it to the osmosis imbalance [232]. However, considering the shale membrane efficiency and the decrease in the volume imbibed, we believe that it would be more realistic to attribute this behavior to the sample

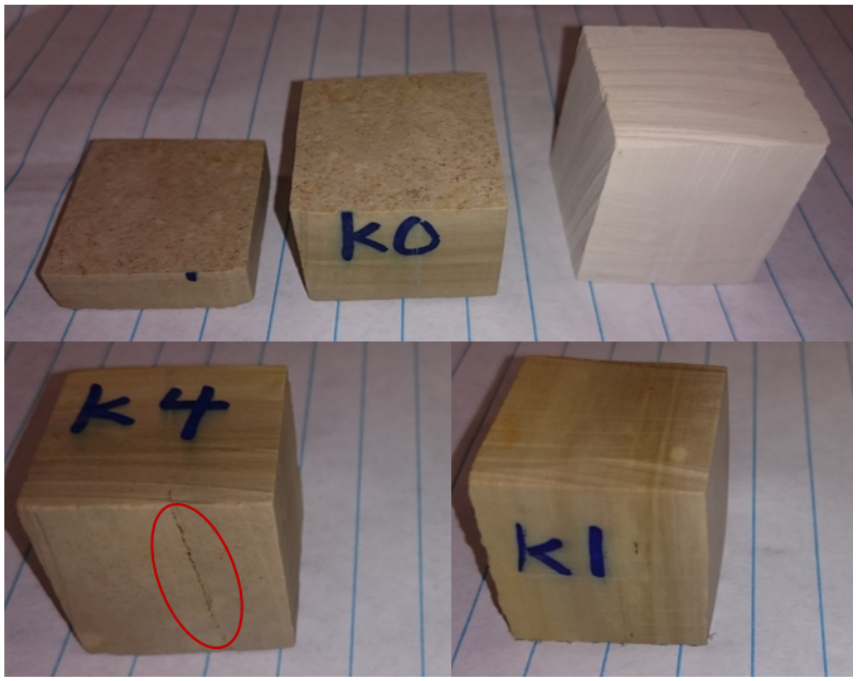

Figure A.8: Images of K samples before (the white sample) and after imbibition. Note that K0 sample broke to two pieces during the imbibition experiment and a fracture appeared in K4 sample (5 wt% salinity) while K1 sample is intact (10 wt% salinity).

expansion and not to the osmosis imbalance. Second, the swelling might induce stresses that are large enough to create micro fractures and in some cases can lead to breaking the sample apart as shown in Fig. A.8. In the next section, we further explore the impact of mineralogy on imbibition data.

A.4.2 Imbibition and Mineralogy

The difference in observed results between the various rock types for slick water imbibition and the impact of salinity on imbibition is a function of the properties of the rock surface and pores. We examined the correlation between rock properties and the imbibition length at 16 hours (representing imbibition rate) for the case of slick water with 9% salinity. This value did not correlate with rock porosity,

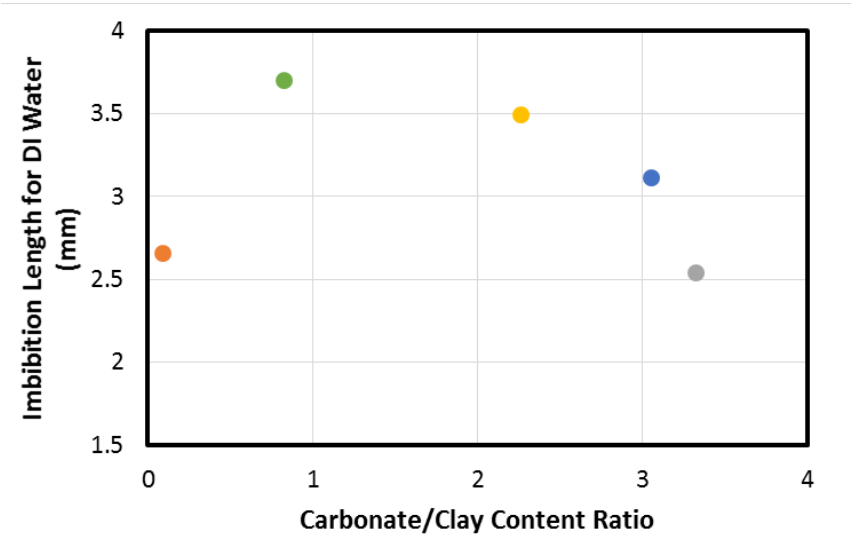

Figure A.9: Imbibition length as a function of carbonate/clay content ratio. Colors represent different rock types as follows: Orange (C), Green (K), Yellow (E), Blue (D), and Gray (W).

or with the specific mineralogy content such as quarts, carbonate or clay content. However, a clear correlation was apparent between this imbibition length and the ratio of carbonate to clay content. This is demonstrated in Fig. A.9. The imbibition length, represented by the imbibed volume divided by the porous exposed surface area, is maximized at a ratio of 1.5, where carbonate content is 50% more than clay content.

When analyzing the impact of salinity on the change in imbibition length, we notice two trends of impact. We report this as a difference in imbibition length between the case of 10 wt% KCl solution and the 0% case. A positive value represents an increase in imbibition length and a negative value implies a decrease in imbibition length with the increase in salinity. The illite content correlates with this value in an interesting way. The result is presented in Fig. A.10. Samples with high illite content show largest difference between 0 and 10 wt% KCl cases, while samples with no illite content show a positive value, reflecting an enhancement in

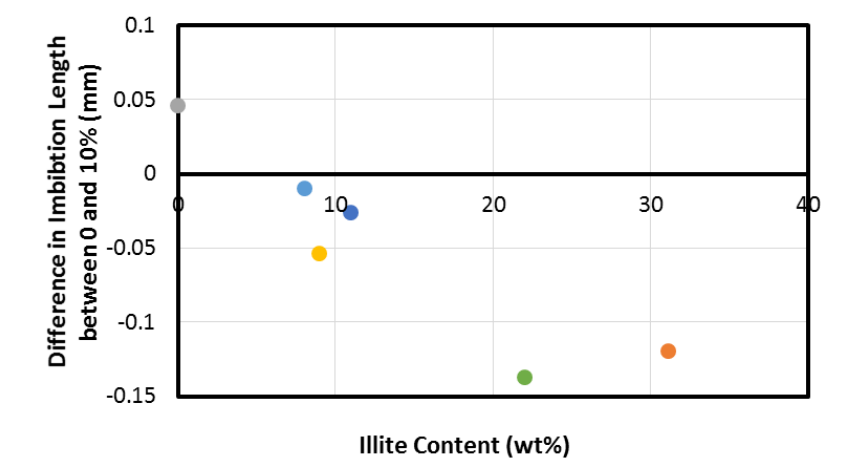

Figure A.10: The impact of salinity on imbibition length shows a monotonic trend with illite content.

imbibition rate with the increase in salinity.

Further investigation of the impact of salinity on imbibition length as correlated with the carbonate/clay content ratio reveals interesting findings that are highly unlikely to be circumstantial. This is discussed in Fig. A.11 and Fig. A.12. The change in imbibition length between the slick water case and the three cases where KCl is presented in Fig. A.11. It clearly shows a minimum impact of salinity on imbibition rate at the same ratio of 1.5 carbonate to clay content for all three salinity cases. The value of that maximum impact is decreases as salinity increases. A positive value of that difference is noted at the largest value of carbonate to clay content ratio. The non-monotonic impact of salinity on imbibition length is investigated in Fig. 12. A plot of the difference between the imbibition length for the 15 wt% KCl case as compared to the 0, 5 and 10% cases is plotted as a function of the same carbonate/clay content ratio. A positive value implies that the 15% solution has a higher imbibition length and a negative value implies its lower. The results reveals that there is a monotonic relationship between the change in imbibition length between the 0 and 15 and between the 10 and 15% cases, and

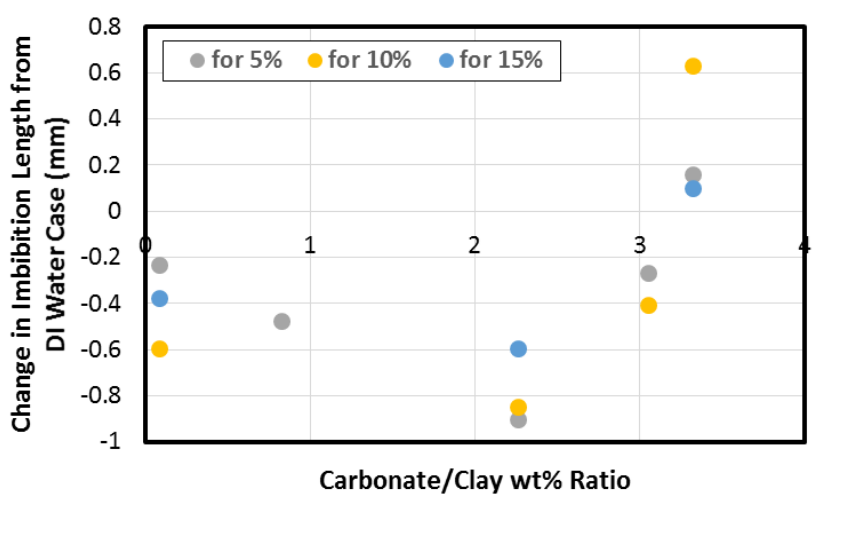

Figure A.11: The change in imbibition length with the increase in salinity as a function of carbonate/clay content ratio.

that the relation between the 5% and 15% is non monotonic with this ratio, with a maximum value at a ratio of 1.5.

Making sense of this result requires further analysis on the distribution of the minerals and its impact on both, the type and distribution of pores as well as the wetting characteristics of the pore walls. The ratio clearly affects both the imbibition rate as well as the impact of salinity on imbibition. The non-monotonic nature of this effect could be related to a type of heterogeneity that could be the key factor in this observed behavior. If this was purely driven by surface hydration [261] and wettability, then the imbibition should behave in a monotonic way when plotted against the wetting ratio of non-water-wet minerals (carbonate) [262] and water-wet minerals (quarts and clay) [263] but such a plot does not reveal a clear correlation in that regard, as shown in Fig. A.13.

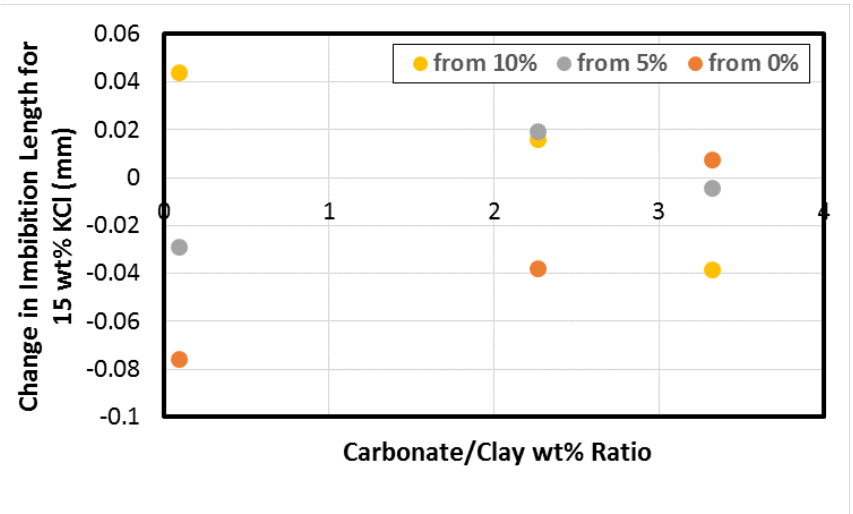

Figure A.12: The difference in imbibition length between the 15 wt% case and other salinity cases as a function of carbonate/clay content ratio.

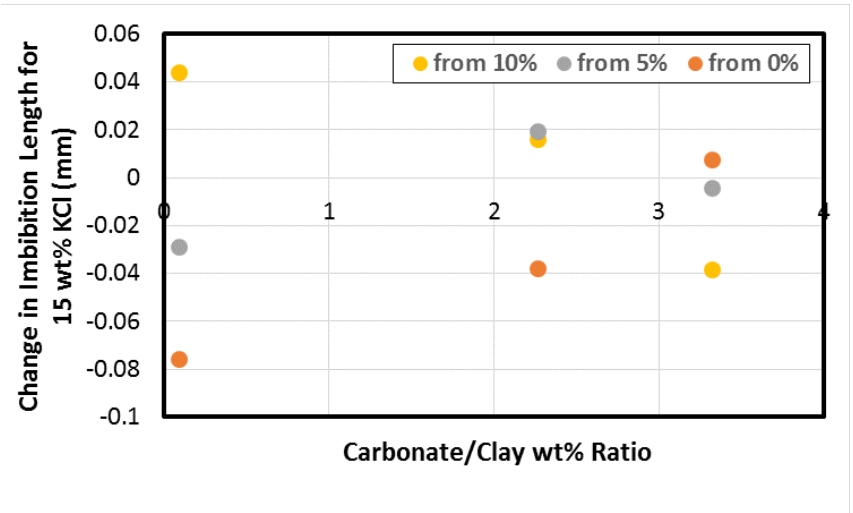

Figure A.13: A plot of imbibition length as a function of wetting ratio reveals no clear correlation.

A.4.3 Formation Softening

Several concerns have been raised regarding the impact of the trapped fracturing fluid on formation strength, which might affect the prolonged productivity of the well [264, 265, 266]. The loss of compressive strength of the samples could be used as a measure of formation softening. Figure 14 presents the compressive strength of the samples after 2 weeks of soaking in various fracture fluid solutions. The compressive strength of the native rock is not recorded in these experiments. While the strength of the C, W and E samples decreases with the increase in fluid salinity, K, D and T samples seem to experience an enhancement in strength with the increase in salinity. This is presented in Fig. A.15 as a percentage of change in compressive strength between the 0 and 10% cases. When investigating the factors affecting the impact of salinity on compressive strength, we observed that the impact was correlated with the amount of siderite and anhydrite present in the rock sample, as shown in Fig. A.16. For low values, less than 5 wt%, a 10 wt% KCl solution results in a compressive strength that is 60% less than that of a 0% KCl solution. On the other extreme, for rocks with 15 wt% siderite and anhydrite, when soaked in 10 wt% KCl solution, it has 40% more compressive strength than when it is soaked in 0% KCl solution.

Other than the K samples which had the lowest compressive strength values, rock types that imbibed more fracturing fluid had higher values of compressive strength. However, within the same rock type, higher imbibition volumes were mostly correlated with lower values of compressive strength as shown in Fig. A.17. In Fig. A.18, a cross plot of the impact of 10 wt% KCl on compressive strength against its impact on imbibition puts the rock samples in three quadrants. At the bottom left, samples C and E experience a negative impact of salinity on both compressive strength and

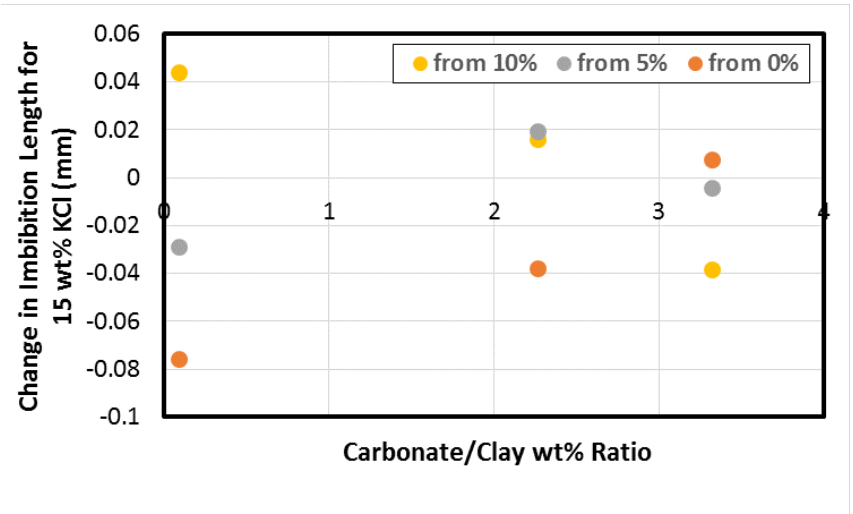

Figure A.14: Compressive strength in MPa for the various rock samples after soaking for two weeks in fracturing fluids with various salinity.

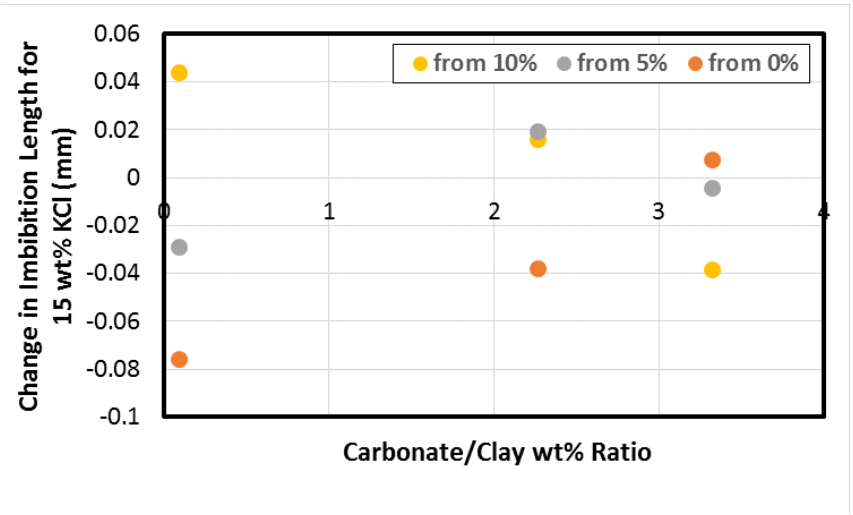

Figure A.15: Change in compressive strength for various rock samples after soaking in 10 wt% KCl solution for two weeks as compared to soaking in a 0 wt% KCl solution.

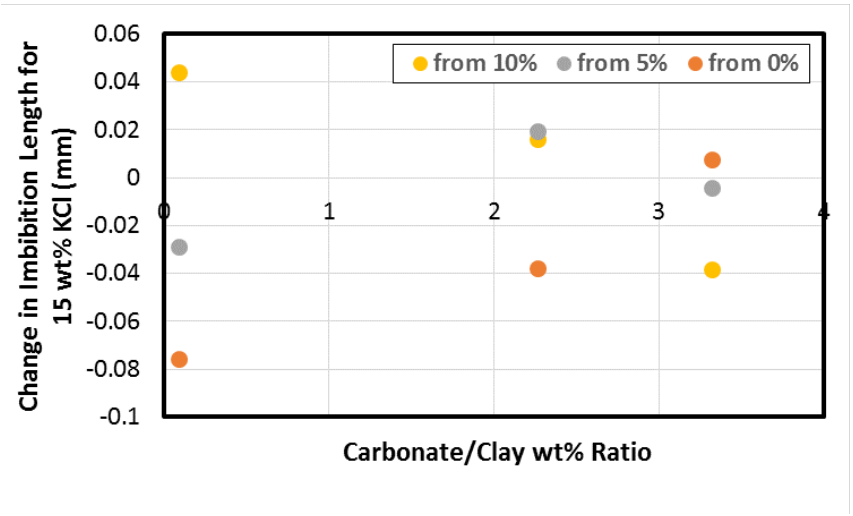

Figure A.16: The impact of salinity on compressive strength, plotted against the sum of siderite and anhydrite composition of the rock.

imbibition. Samples K, T and D in the upper left quadrant experience a positive impact of salinity on compressive strength and a negative impact on the imbibed volume. Sample W at the bottom right quadrant experiences a negative impact of salinity on compressive strength and a positive impact on imbibed volume. The worse impact of fracturing fluid on rock softening was experienced for K samples as shown in Fig. A.8 where the sample placed in deionized water broke apart after 6 hr., the sample placed in 5% KCL exhibits only visible fractures, and the sample placed in 10 wt% KCl solution stayed in. It is worth noting that the rock-fluid interactions in some cases might induce tangible reduction in the rock permeability, yet minimal impact on sample compressive strength. Impact on permeability was not recorded in this study. KCl clay interactions could result in enhancing the formation strength by reducing the spacing between the clay sheets. In addition, carbonates and feldspars reactions could be activated through reversible reactions controlled by the water ionization [267]. The impact observed on imbibition capacity and compressive strength is the result of a combination of various factors. The

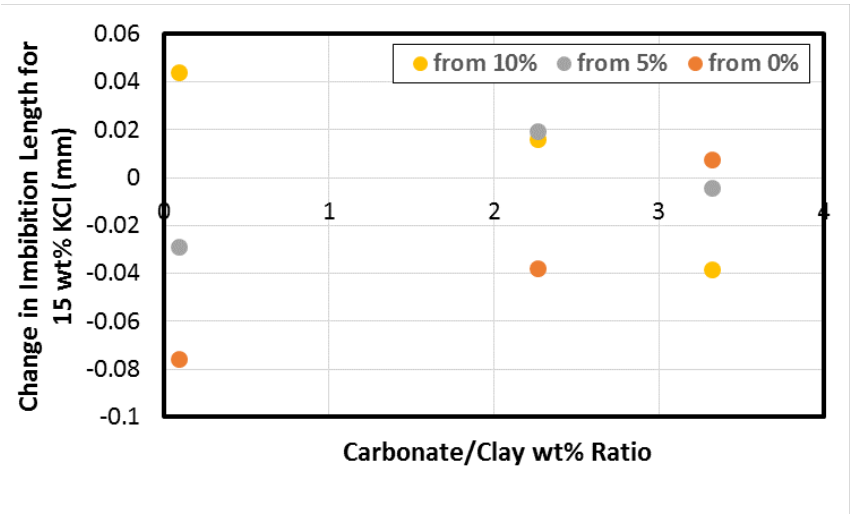

Figure A.17: A cross plot of the impressive strength of the rock and the imbibition length at 16 hours for various rock samples.

results presented in this paper correlate those effects with various rock properties, especially rock mineralogy.

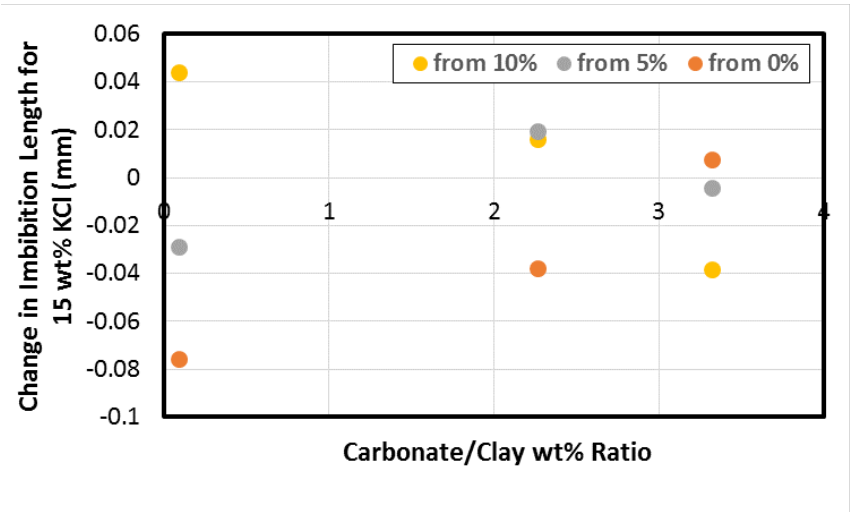

Figure A.18: A cross plot of the impact of 10 wt% KCl solution on rock compressive strength and on imbibition length for various rock samples.

A.5 Conclusion

We performed a systematic set of experiments to investigate the relationship between the salinity, imbibition and formation softening for rocks with different mineralogy content. KCl was chosen as the control agent for salinity because of its impact on reducing clay swelling. The main findings are listed below:

- Low salinity does not always result in an increase in fracturing fluid imbibition and gas recovery. The results reveal a correlation with illite content, where more illite results in a higher impact of salinity on imbibition, and no illite shows on the positive side of the chart where higher salinity results in more imbibition.

- Carbonate/clay content ratio seems to have a significance when it comes to the volume imbibed and the impact of salinity on imbibition. The amount imbibed is maximum at a ratio of 1 to 1.5 for the samples used in this study. The impact of salinity on imbibition also sits at a maximum at that ratio, while the rock with the maximum ratio of 3.5, W, experienced the opposite trend of salinity impact than the remainder of the rock samples.

- Neither compressive strength nor imbibition seem to correlate directly with quartz, carbonate or clay content for the samples used in this study.

- Samples with higher siderite + anhydrite content showed a positive impact of salinity on compressive strength, while samples with lower siderite + anhydrite content experienced a negative impact of salinity on compressive strength.

- The reverse imbibition observed in some of the samples during the late stages of imbibition, reflected as a drop in tail end of the plot, might be misinterpreted

as reverse osmosis flow. However, we ascribed it to the expansion in the bulk volume induced by clay swelling.

Appendix B

Asphaltene Deposition Impact on Fluid Flow

B.1 Abstract

Asphaltene deposition in oil reservoirs is a contentious issue affecting both well and reservoir productivity. Though the phenomenon has been previously studied in several laboratory experiments, the uniformity aspects of the asphaltene deposit are usually overlooked. We have previously developed an experimental workflow to create a uniform deposit of asphaltene inside the core sample. In this study, the impact of this uniform deposit on fluid flow is quantified through imbibition, corefloods and relative permeability experiments. In addition, the lab results are used in a field scale simulation to investigate the impact of deposition on field performance. The results exhibit a shift in the wettability state where a reduction in both water imbibition rate and capacity are observed after deposition. Besides, up to 25% reduction in absolute permeability is detected. Results of pressure drop experiments across the core conducted on the exposed rocks indicate a change in the wetting character-

istics, with the exposed rocks becoming more mixed/intermediate wet and varying with the change in the initial brine saturation in the rock. Subsequently, the relative permeability set is affected where a shift in the oil residual saturation, a downgrade in the oil curve and an upgrade in the water curve are observed. Upscaling this new data to field scale indicated a loss of more than half of the well productivity and an earlier breakthrough if waterflooding is implemented.

B.2 Introduction

Asphaltenes characterization and stability is a topic of continuous importance to the petroleum industry. Asphaltenes constitute the most polar fraction of crude oil [268] with an undefined molecular weight or structure [269, 270]. They are usually defined as a solubility class, where asphaltenes are soluble in light aromatics such as benzene and toluene, and insoluble in light aliphatic like pentane and heptane [271, 272, 273, 274]. The deposition of these molecules could be triggered by disturbing the equilibrium state through either a change in the physical conditions or the composition [275].

Several thermodynamics models have been proposed to study asphaltene stability. Some advocate the colloidal nature of asphaltene, where the precipitation is caused by micelle flocculation, and others advocate the molecular nature of asphaltene where precipitation happens conventionally. For instance, Leontaritis and Mansoori assumed asphaltene molecules are suspended solid particles peptized by resin molecules present in the mixture [276]. On the other hand, Wang and Buckley proposed a two-component solubility model to predict the onset of asphaltene flocculation [272].

The permeability impairment induced by asphaltene deposition is evident in

several experimental studies [277, 278, 279]. Minssieux (1997) conducted core flood experiments on sandstone samples using different crude oils where a 20-90% drop in the absolute permeability to cyclohexane is observed [280]. They analyzed the asphaltene content of oil at both the inlet and effluent streams when they inferred that the permeability impairment was indeed due to asphaltene deposition. Hamadou et al. (2008) focused on quantifying the damage in the absolute permeability of the Berea and Rhourd-Nouss cores where Soltrol was injected to both displace the crude oil and measure the initial and final permeability [281]. In addition, they correlated the extent of damage to the iron content of the core, where a negative relationship was observed with a reduction in the possible damage occurring in the cores with a higher iron content. This relationship was also validated by Behbahani et al. (2013) who observed the same trend, besides a positive relationship between the calcite content and the extent of deposition [282]. The deposition of asphaltene in carbonate rocks is evident. Kord et al. (2012) used both live and dead oil samples to study the deposition of asphaltene where they reported an exponential behavior for the impact of deposition on permeability damage and a linear behavior for pore plugging [283].

Asphaltene deposition has been modeled at both the well and the reservoir scales. Almehaideb (2004) developed a four-component single well model where both the distribution of precipitated asphaltene molecules and the permeability and porosity reduction induced by plugging and deposition are reported [284]. Shirdel et al. (2012) critically reviewed the current deposition models for asphaltene [285]. Mohebbinia et al. (2017) used PC-SAFT EOS to properly simulate the asphaltene deposition [286]. Further developments in the understanding of asphaltene include using a support vector machine to develop a model for asphaltene precipitation [287], computational fluid dynamics to study the deposition of asphaltene molecules

[288, 289], and molecular simulation to study the interactions among these molecules [290].

The relation between rock wettability and asphaltene deposition is the focus of many research studies [291, 292]. Al-Maamari and Buckley (2000) experimentally studied the relation between asphaltene stability and the wetting nature of mica surfaces where the oil wetting nature increased for the majority of the crudes tested [293]. Uetani (2014) observed an increase in the water cut after the asphaltene onset, which could be attributed to an enhanced oil wetting state induced by asphaltene deposition [294]. Mirzayi et al. (2008) also studied the alteration of rock wettability by determining the reduction in the irreducible water after crude injection, decreased from 26.5% to 10.7% [295]. However, they did not take into account the effect of the non-uniform deposition on the flow behavior. Wolcott et al. (1996) tested and quantified this wettability change using Amotts imbibition tests where they related the extent of wettability alteration to the content of asphaltene and resin, as well as the aging period [296].

Limited studies were also conducted on the effect of asphaltene deposition on two phase flow behavior and its impact at a reservoir scale. Hematfar et al. (2013) performed several experiments on sand packs with asphaltene from Canada, and observed a shift in the relative permeability endpoints, corresponding to the adsorption of asphaltenes onto the surface [297]. Similar results were also obtained by Shedid (2001) who studied the deposition of asphaltene in carbonate rocks with crudes of different asphaltene contents [298]. It was observed that the relative permeability end points are shifted further depending on the asphaltene content, with the crude having a higher asphaltene content showing lower irreducible water saturation. Nasri and Dabir (2009) upscaled the effect of relative permeability shifts to a field scale where they observed a reduction in both the cumulative oil production

and the bottom hole pressure and that the extent of this drop was dependent on the asphaltene content of the crude [299].

Most of the experimental work cited acknowledges the non-uniformity aspect of the deposition, where the inlet of the core experiences a larger drop in permeability; however, that literature does not note the need for a uniform asphaltene deposition so that meaningful relative permeability data can be collected. When a core experiences a gradient in permeability change between the inlet and outlet due to the non-uniform deposit of asphaltene, the measured flow and pressure data cannot be reliably translated into usable relative permeability data that can be used in simulation efforts. In this work, the impact of uniform asphaltene deposition on both reservoir characteristics and fluid mobility is quantified. The uniformity of the asphaltene deposit is what distinguishes our work from previous attempts towards such measurements. The rest of this paper is organized as follows; in the material and methodology section, both rocks and fluids used are presented along with the experimental procedure and the simulation details. In the results and discussion section, the impact of deposition on imbibition and pressure drop is analyzed. After that, the permeability impairment associated with the deposition is investigated, and subsequently, the results are implemented in a field scale study. Finally, the main findings and concluding remarks are summarized in the conclusions section.

B.3 Materials and Methods

B.3.1 Rocks and Fluids

Berea sandstones cores are used with a diameter of one inch, and a length ranging from one to six inches. Air coring is implemented, as the rocks are prone to clay

swelling. The cored samples are polished to achieve a flat surface and their dimensions are then measured. The porosity of the cores is measured using a porosimeter based on Boyles law with helium expansion. Once the porosity is measured, the absolute permeability of the cores is estimated using a nitrgoen gas permeameter under a confining pressure of 1500 psi. The rock properties and dimensions are reported in Table B.1.

The crude oil used in these experiments is obtained from a wellhead in Texas. The asphaltene content is measured using a modified form of the ASTM IP143 Standard for the Determination of asphaltenes in Crude Petroleum [300]. Two grams of oil are mixed with 80 grams of heptane and heated to accelerate asphaltene aggregation. The sample is then passed through a filter paper under vacuum. The deposit is dissolved in toluene and then evaporated to measure the amount of asphaltene in the sample. Brine with 3 wt.% NaCL is used to suppress clay swelling experienced with fresh water. In addition, heptane is used as a displacement fluid, as it is not a solvent to the asphaltenes. Toluene is used mainly for cleaning the setup, during the asphaltene content filtration test, as well as to remove the asphaltene deposition. Helium and nitrogen are used to measure the porosity and permeability respectively. The fluid properties are summarized in Table B.2.

B.3.2 Experimental Procedures

Previously, we investigated the uniformity of the asphaltene deposit where the deposit established through vacuum-saturating the cores exhibits more uniform distribution than asphaltene deposit through injecting oil into the cores [132]. In this work, we utilized the protocol established in that publication to study the impact of asphaltene deposits on fluid flow using imbibition and core flood experiments.

This step was identified as essential so that meaningful macroscopic flow data can be collected and analyzed. The imbibition experiments are conducted on the cores utilizing two imbibition cycles. Oil-saturated cores are dried for a day after flushing it with heptane. The imbibition tests involve alternating water and heptane cycles into air-saturated cores, separated by 1 day of drying. The weight change of the submerged cores is used to monitor the progress of imbibition. On a different set of cores, pressure drop is recorded during brine and heptane flooding.

Relative permeability is estimated to evaluate the impact of the asphaltene deposit on the mobility of fluids. Six-inch cores are used for these experiments. Brine and heptane are injected in a varying sequence (total flow rate is less than 2 cc/min) to obtain the end points of the relative permeability curves. Stones correlations are used in order to generate the relative permeability graphs given the measured end-point data.

B.3.3 Simulation Details

The lab results are implemented at the field scale using a black-oil model; in such model, there phases are considered (oil, gas and water) where the compositional changes are insignificant. The reservoir extends 2500 ft. x 2500 ft. and properties are listed in Table B.3. The impact of asphaltene deposition is incorporated by adopting the damaged core relative permeability curves along with a 10% reduction in the absolute permeability. The reservoir model includes one injector, whose rate is constrained to 1000 bbl/day, and one producer, whose bottom-hole pressure is constrained to 2000 psi, placed at the corners. The injection well is rate-constrained. Our model is layered, where the water is injected from the bottom and the oil is produced from the top. We designed our simulation scenario as a water flood

Table B.1: Cores dimensions and properties.

Purpose	Cores	L (in)	D (in)	W (gm)	ϕ (%)	K(md)	Process
Spontaneous Imbibition	GB-J2-1	1.958	0.999	51.97	22.49	-	Control- DI/Hep/DI
	GB-J2-2	1.899	0.996	50.45	22.42	125	Exposed to crude-DI/Hep
	GB-J2-4	1.984	1.000	53.06	22.20	133	Exposed to crude-Hep/DI
Pressure Drop Test	GB-J9-3	1.954	0.996	53.23	19.88	105	Control -Brine Injection- Heptane Injection
	GB-J6-3	1.990	0.985	52.69	19.88	107	Vacuum Saturated– Heptane Flush- Dried- Brine Injection- Heptane Injection
	GB-J6-2	1.928	0.986	51.00	19.25	117	Vacuum Saturated–Heptane/crude slugs (4:1 PV) - Heptane/crude co-injection– Heptane Flush- Dried- Brine Injection- Heptane Injection
	GB-J9-2	1.844	0.998	49.90	20.77	118	Crude Injection– Heptane Flush- Dried- Brine Injection- Heptane Injection
Relative Perm	GB-J7-1	5.960	0.992	159.70	20.11	135	Clean
	GB-J10-1	5.992	0.999	163.48	19.86	-	Saturated

Table B.2: Fluids used, and their Properties

Fluid	Density (g/cm^3)	Viscosity (cp.)
Texas Crude*	0.884	19
Brine	1.021	1.32
Heptane	0.684	0.376
Toluene	0.865	0.560
Deionized Water	1	1

* Asphaltene content: 0.85 ±0.2 wt.%

where we could quantify the changes in the multiphase flow characteristics and its impact on productivity. In addition, we differentiated between the damage resulting from the absolute permeability and the damage resulting from relative permeability. This is manifested by simulating a scenario where the absolute permeability is the only modified parameter and another where the relative permeability is the only modified scenario, after that the performance of these scenarios is compared to the overall performance where both absolute and relative permeability damage are incorporated.

Table B.3: The input parameters used for simulation

Fluid	Density (g/cm^3)	Viscosity (cp.)
Texas Crude*	0.884	19
Brine	1.021	1.32
Heptane	0.684	0.376
Toluene	0.865	0.560
Deionized Water	1	1

* Asphaltene content: 0.85 ±0.2 wt.%

B.4 Results and Discussions

In this section, the impact of the deposition on spontaneous imbibition, pressure drop during core flooding, and relative permeability is presented. After that, results are used in a field example.

B.4.1 Imbibition Results

As a dynamic measure of the wettability state of the rock, imbibition experiments are conducted on dry cores that have been vacuum-saturated with crude oil, aged, and flooded with heptane then dried. The results as presented in Fig. B.1. While, the initial imbibition rate is controlled by capillary suction, the imbibition capacity indicates the accessible pore volume [85, 163]. It is clearly observed that the heptane imbibition behavior experiences two distinct early and late imbibition rates for a given rock sample. With clear variations in the initial rate, the late rate is relatively the same for all the heptane cases considered. On the other hand, the water imbibition behavior experiences a relatively slower initial rate with a late rate close to zero. This behavior can be attributed to the lower density and viscosity of heptane compared to water, which results in both a faster imbibition of heptane and a larger accessible pore volume as the trapped gas could easily induce counter-current flow.

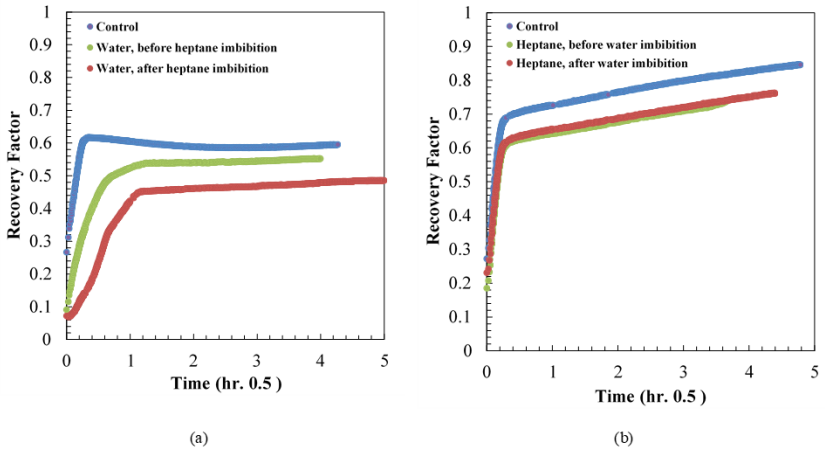

Figure B.1: The imbibition results: A) Water Imbibition B) Oil Imbibition

Both the reduction in the initial imbibition rate and capacity in the case of the water compared to the control sample reflects the damage induced by asphaltene deposition in its impact on permeability and wettability. While the reduction imbibition rate indicates a shift in the water wetting nature of the rock towards reduced water-wetting, the reduction in the imbibition capacity indicates the conductivity damage induced. In addition, the reduction in the imbibition capacity for heptane in the second cycle compared to the control indicates the damage to the flow capacity of the rock. The non-monotonic behavior of water imbibition in the control run presented in Fig B.2 was attributed in our earlier work to clay swelling [163]. Interestingly, both water imbibition tests performed for rocks that were exposed to oil do not show such a signature although fresh water was used in the tests. This is an indication that clay particles had less access to the imbibed water. Exposure to heptane reduced the water wetting nature even more as shown in Fig B.2a, while exposure to water did not affect the heptane imbibition as shown in Fig B.2b.

B.4.2 Pressure Drop

A reduction in the pressure drop during brine injection experiments is observed when the core is exposed to crude oil compared to the reference case, which implies a shift in the wetting nature of the rock. This shift increases when more deposition is introduced to the system by vacuum saturating the core or vacuum saturating followed by slug and co-injection of heptane/crude oil (both cases were aged). The hump in the pressure drop curves is usually observed when the wetting-phase is injected [301]. The further the hump decreased, the more the wetting nature has shifted. Figure B.3 displays the pressure drop across the core for both brine and heptane injection, along with the brine saturation value at the end of the last round of heptane injection. The saturation history of the rock is also noted in the legend of the figure. The native rock has close to 30% irreducible water, while a drop to 20% irreducible water is observed for rocks exposed to crude. The rock experiencing the least resistance to heptane injection is the one that was exposed to crude using vacuum-saturation. This reduction in pressure is attributed to the decrease in capillary pressure and not an increase in oil mobility. This set of data asserts the findings from the imbibition tests, reflecting a reduced state of water-wetting. Rocks exposed to water before crude saturation show less change in their wetting nature as seen in the case of GB-J9-2.

B.4.3 Permeability Impairment

The impact of asphaltene deposition on rock conductivity is reported by quantifying both the absolute permeability loss and the shift in the relative permeability curves. Larger damage is reported for samples where asphaltene deposition is induced by injection compared to the vacuum-statured ones as shown in Fig. B.4. Comparing

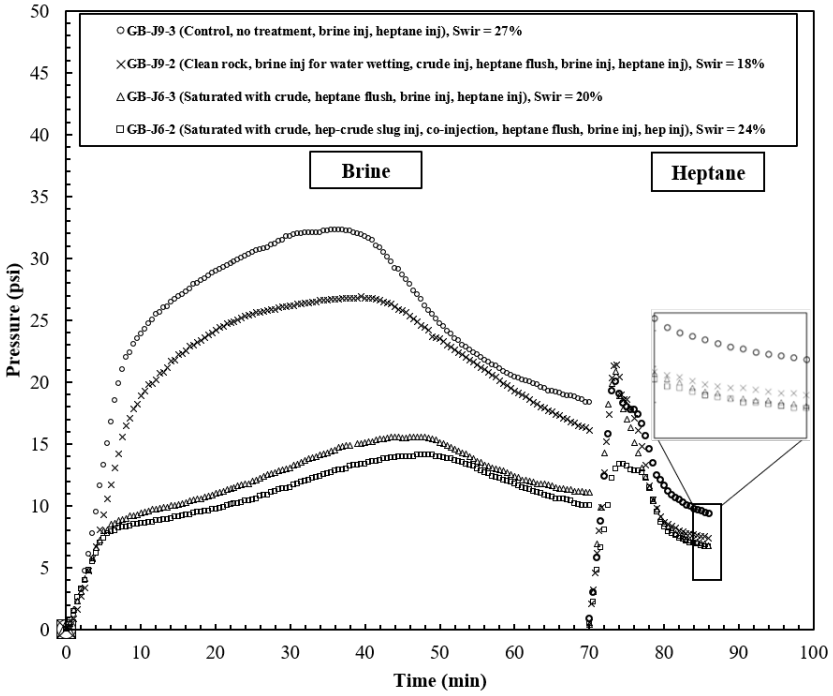

Figure B.2: Pressure drop across the core for both brine and heptane injection.

this result to the TOC distribution in vacuum-statured cores implies that asphaltene deposition in vacuum-saturated cores is more distributed in the pore body compared to the injected cores where more asphaltene is concentrated in the pore throats as illustrated in the back-injection results of James et al. (2018).

The relative permeability curves for one of the vacuum-saturated cores is compared to the native curves in Fig. B.5. A shift in the end-points of the curve clearly indicates a change in flow behavior. While a significant increase is observed in the critical oil saturation, the critical water saturation is not affected. In addition, the water curve is boosted and the oil curve is suppressed. A reduction in the saturation window that allows both phases to be mobile was observed for the altered curves. All these indicators support the conclusion that the distributed asphaltene deposit impairs relative permeability.

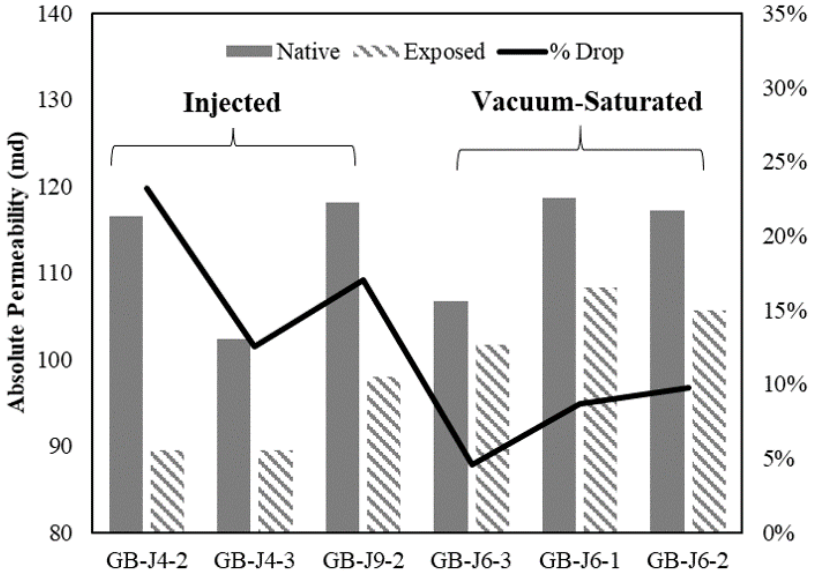

Figure B.3: Permeability damage for injected and vacuum-saturated cores

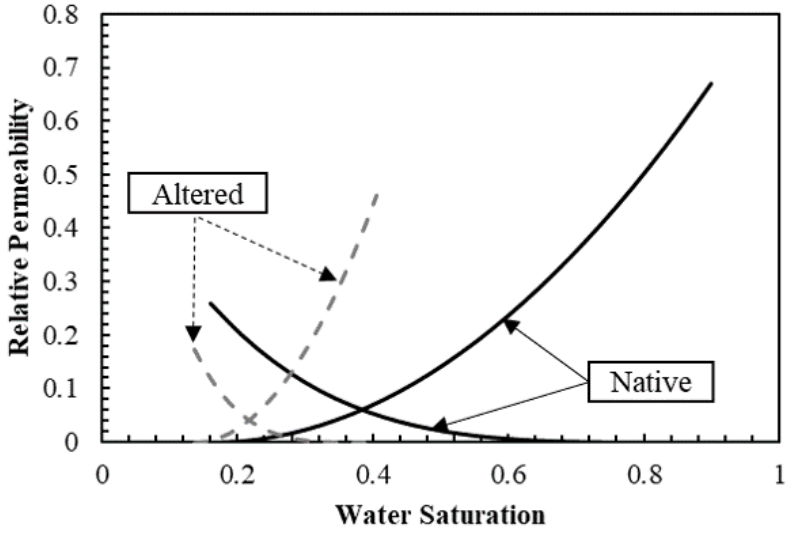

Figure B.4: The smoothed relative permeability for both clean and exposed cores.

B.4.4 Simulation Results

The oil saturation maps for both the native and the altered models at the end of the simulation time are presented in Fig. B.6. According to the simulation results, more than half of the wells productivity is lost due to the asphaltene deposition as presented in Fig. B.7. In addition, early break through is observed for the altered case. However, this could be intuitively predicted considering the residual oil saturation and the enhanced water mobility used in the relative permeability curves. The impact of the absolute permeability reduction on the well productivity is negligible compared to the relative permeability. The accompanying increase in the injection pressure with the asphaltene deposition, reported in Fig. B.7, highlights the detrimental impact of asphaltene deposition during water flooding. It is worth noting that we considered the relative permeability damage in the whole reservoir, not only near the wellbore. Recalling our experimental observations, asphaltenes are depositing throughout the core by just introducing the crude to the rock. This means that the flow of oil in porous media by itself would result in deposition. Herein, we trying to upscale this observation by adopting the damaged relative permeability for the whole reservoir.

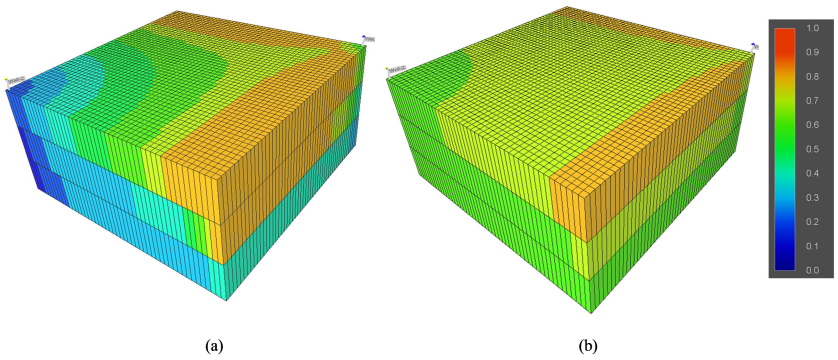

Figure B.5: The oil distribution map after 50 years simulation time a) native b) exposed. Higher residual oil saturation is observed for the exposed case which reflects the damage incorporated in the relative permeability.

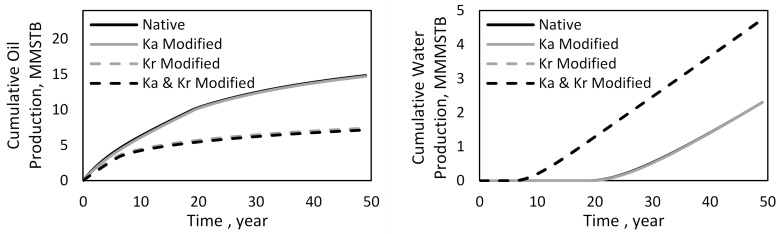

Figure B.6: The impact of the asphaltene deposit on the reservoir productivity- a) Cumulative oil production b) Cumulative water production. (Native case does not consider the asphaltene deposition, Ka case considers the damage occurred in the absolute permeability only, Kr case considers the damage occurred in the relative permeability only and Ka & Kr case considers the damage to both the absolute and relative permeability)

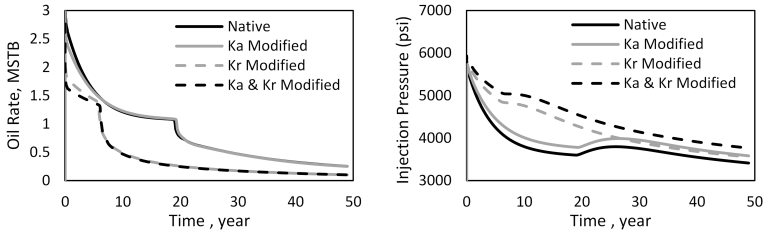

Figure B.7: The impact of asphaltene deposit on the reservoir productivity and injectivity a) the oil rate b) the injection pressure

B.5 Conclusions

In this study, the precipitation of asphaltenes in Grey Berea rock samples, and its impact on rock characteristics are studied. The following are our main findings:

- Permeability impairment is up to 25% for cores where the deposition is introduced by continuous injection and 15% for cores where the deposition is introduced by vacuum saturating the core. Given that vacuum saturation results in uniform deposition, meaningful relative permeability data must be collected using these samples and not using cores where a non-uniform deposit is achieved.

- A change in the wetting properties is evident, with the cores become more neutral or oil wet based on imbibition and injection tests, when exposed to crude and the precipitated asphaltenes. This was greatly dependent on the initial brine saturation in the rock, where those rocks exposed to brine show a state of mixed wetting. Obtaining relative permeability data from cores that do not have an initial water saturation can be misleading on the extent of wettability alteration achieved.

- A reduction in clay swelling is observed in rocks exposed to crude oil

- Relative permeability end-points are determined experimentally where a higher irreducible oil saturation is observed for the exposed cores. One major finding to note in this case is the reduction in the width of the saturation window where both water and oil mobility is possible.

- Incorporating the formation damage in a reservoir simulator anticipates productivity loss of more than half of the wells potential. In addition, both earlier breakthrough time and higher injection pressure are expected due to asphaltene precipitation in the reservoir. Our decoupling of the impact of absolute permeability reduction and relative permeability effects shows that the effect of changes in relative permeability are much more pronounced than the changes in absolute permeability.

Bibliography

[1] RM Lansangan and JL Smith. Viscosity, density, and composition measurements of co2/west texas oil systems. *SPE reservoir engineering*, 8(03):175–182, 1993.

[2] Tausif Ahmed, Hadi Nasrabadi, and Abbas Firoozabadi. Complex flow and composition path in co2 injection schemes from density effects. *Energy & Fuels*, 26(7):4590–4598, 2012.

[3] Mohammad Kariznovi, Hossein Nourozieh, and Jalal Abedi. Phase composition and saturated liquid properties in binary and ternary systems containing carbon dioxide, n-decane, and n-tetradecane. *The Journal of Chemical Thermodynamics*, 57:189–196, 2013.

[4] Hossein Nourozieh, Mohammad Kariznovi, and Jalal Abedi. Measurement and correlation of saturated liquid properties and gas solubility for decane, tetradecane and their binary mixtures saturated with carbon dioxide. *Fluid Phase Equilibria*, 337:246–254, 2013.

[5] Junfang Zhang, Zhejun Pan, Keyu Liu, and Nick Burke. Molecular simulation of co2 solubility and its effect on octane swelling. *Energy & Fuels*, 27(5):2741–2747, 2013.

[6] Bing Liu, Jiawei Li, Chao Qi, Xiaoqi Li, Tingyi Mai, and Jun Zhang. Mechanism of asphaltene aggregation induced by supercritical co 2: insights from molecular dynamics simulation. *RSC Advances*, 7(80):50786–50793, 2017.

[7] Toshimasa Takanohashi, Shinya Sato, Ikuo Saito, and Ryuzo Tanaka. Molecular dynamics simulation of the heat-induced relaxation of asphaltene aggregates. *Energy & fuels*, 17(1):135–139, 2003.

[8] Toshimasa Takanohashi, Shinya Sato, and Ryuzo Tanaka. Structural relaxation behaviors of three different asphaltenes using md calculations. *Petroleum science and technology*, 22(7-8):901–914, 2004.

[9] Alexandre N. M. Carauta, Peter R. Seidl, Erika C. A. N. Chrisman, Jlio C. G. Correia, Prscila de O. Menechini, Daniel M. Silva, Katia Z. Leal, Sonia M. C.

de Menezes, Wladimir F. de Souza, and Marco A. G. Teixeira. Modeling solvent effects on asphaltene dimers. *Energy & Fuels*, 19(4):1245–1251, 2005.

[10] B Aguilera-Mercado, C Herdes, J Murgich, and EA Mller. Mesoscopic simulation of aggregation of asphaltene and resin molecules in crude oils. *Energy & Fuels*, 20(1):327–338, 2006.

[11] Edo S Boek, Hemant K Ladva, John P Crawshaw, and Johan T Padding. Deposition of colloidal asphaltene in capillary flow: experiments and mesoscopic simulation. *Energy & fuels*, 22(2):805–813, 2008.

[12] Edo S Boek, Dmitry S Yakovlev, and Thomas F Headen. Quantitative molecular representation of asphaltenes and molecular dynamics simulation of their aggregation. *Energy & Fuels*, 23(3):1209–1219, 2009.

[13] Thomas F. Headen, Edo S. Boek, and Neal T. Skipper. Evidence for asphaltene nanoaggregation in toluene and heptane from molecular dynamics simulations. *Energy & Fuels*, 23(3):1220–1229, 2009.

[14] Thomas F. Headen and Edo S. Boek. Molecular dynamics simulations of asphaltene aggregation in supercritical carbon dioxide with and without limonene. *Energy & Fuels*, 25(2):503–508, 2011.

[15] Mohammad Sedghi, Lamia Goual, William Welch, and Jan Kubelka. Effect of asphaltene structure on association and aggregation using molecular dynamics. *The Journal of Physical Chemistry B*, 117(18):5765–5776, 2013.

[16] Julio F Jover, Erich A Mller, Andrew J Haslam, Amparo Galindo, George Jackson, Herv Toulhoat, and Carlos Nieto-Draghi. Aspects of asphaltene aggregation obtained from coarse-grained molecular modeling. *Energy & Fuels*, 29(2):556–566, 2015.

[17] Jiang Wang and Andrew L Ferguson. Mesoscale simulation of asphaltene aggregation. *The Journal of Physical Chemistry B*, 120(32):8016–8035, 2016.

[18] Mohammad Sedghi and Lamia Goual. Molecular dynamics simulations of asphaltene dispersion by limonene and pvac polymer during co 2 flooding. In *SPE International Conference and Exhibition on Formation Damage Control*. Society of Petroleum Engineers.

[19] T. F. Headen, E. S. Boek, G. Jackson, T. S. Totton, and E. A. Mller. Simulation of asphaltene aggregation through molecular dynamics: Insights and limitations. *Energy & Fuels*, 31(2):1108–1125, 2017.

[20] Salah Yaseen and G. Ali Mansoori. Molecular dynamics studies of interaction between asphaltenes and solvents. *Journal of Petroleum Science and Engineering*, 156:118–124, 2017.

[21] Timing Fang, Muhan Wang, Jiawei Li, Bing Liu, Yue Shen, Youguo Yan, and Jun Zhang. Study on the asphaltene precipitation in co2 flooding: A perspective from molecular dynamics simulation. *Industrial & Engineering Chemistry Research*, 2017.

[22] Ian C Bourg and Garrison Sposito. Molecular dynamics simulations of the electrical double layer on smectite surfaces contacting concentrated mixed electrolyte (naclcacl 2) solutions. *Journal of colloid and interface science*, 360(2):701–715, 2011.

[23] Philip C Myint and Abbas Firoozabadi. Thin liquid films in improved oil recovery from low-salinity brine. *Current Opinion in Colloid & Interface Science*, 20(2):105–114, 2015.

[24] Thomas Underwood, Valentina Erastova, Pablo Cubillas, and H Chris Greenwell. Molecular dynamic simulations of montmorilloniteorganic interactions under varying salinity: An insight into enhanced oil recovery. *The Journal of Physical Chemistry C*, 119(13):7282–7294, 2015.

[25] Thomas Underwood, Valentina Erastova, and H Chris Greenwell. Wetting effects and molecular adsorption at hydrated kaolinite clay mineral surfaces. *The Journal of Physical Chemistry C*, 120(21):11433–11449, 2016.

[26] Felipe Jimnez-ngeles and Abbas Firoozabadi. Tunable substrate wettability by thin water layer. *The Journal of Physical Chemistry C*, 120(43):24688–24696, 2016.

[27] Felipe Jimnez-ngeles and Abbas Firoozabadi. Contact angle, liquid film, and liquidliquid and liquidsolid interfaces in model oilbrinesubstrate systems. *The Journal of Physical Chemistry C*, 120(22):11910–11917, 2016.

[28] JA Greathouse, RT Cygan, JT Fredrich, and GR Jerauld. Adsorption of aqueous crude oil components on the basal surfaces of clay minerals: Molecular simulations including salinity and temperature effects. *The Journal of Physical Chemistry C*, 121(41):22773–22786, 2017.

[29] Huanhuan Tian and Moran Wang. Molecular dynamics for ion-tuned wettability in oil/brine/rock systems. *AIP Advances*, 7(12):125017, 2017.

[30] TR Zeitler, JA Greathouse, RT Cygan, JT Fredrich, and GR Jerauld. Molecular dynamics simulation of resin adsorption at kaolinite edge sites: Effect of surface deprotonation on interfacial structure. *The Journal of Physical Chemistry C*, 121(41):22787–22796, 2017.

[31] Zhehui Jin and Abbas Firoozabadi. Methane and carbon dioxide adsorption in clay-like slit pores by monte carlo simulations. *Fluid Phase Equilibria*, 360:456–465, 2013.

[32] Zhehui Jin and Abbas Firoozabadi. Effect of water on methane and carbon dioxide sorption in clay minerals by monte carlo simulations. *Fluid Phase Equilibria*, 382:10–20, 2014.

[33] Zhehui Jin and Abbas Firoozabadi. Flow of methane in shale nanopores at low and high pressure by molecular dynamics simulations. *The Journal of chemical physics*, 143(10):104315, 2015.

[34] Zhehui Jin and Abbas Firoozabadi. Phase behavior and flow in shale nanopores from molecular simulations. *Fluid Phase Equilibria*, 430:156–168, 2016.

[35] Zhehui Jin, Abbas Firoozabadi, et al. Thermodynamic modeling of phase behavior in shale media. *SPE Journal*, 21(01):190–207, 2016.

[36] Yinan Hu, Deepak Devegowda, Alberto Striolo, Tuan A Ho, Anh Phan, Faruk Civan, Richard F Sigal, et al. A pore scale study describing the dynamics of slickwater distribution in shale gas formations following hydraulic fracturing. In *SPE Unconventional Resources Conference-USA*. Society of Petroleum Engineers, 2013.

[37] Yinan Hu, Deepak Devegowda, Alberto Striolo, Anh Phan, Tuan A Ho, Faruk Civan, Richard F Sigal, et al. Microscopic dynamics of water and hydrocarbon in shale-kerogen pores of potentially mixed wettability. *Spe Journal*, 20(01):112–124, 2014.

[38] Bo Li, Khoa Bui, I Yucel Akkutlu, et al. Capillary pressure in nanopores: Deviation from young-laplace equation. In *SPE Europec featured at 79th EAGE Conference and Exhibition*. Society of Petroleum Engineers, 2017.

[39] Mohamed Mehana, Mashhad Fahes, and Liangliang Huang. Asphaltene aggregation in oil and gas mixtures: Insights from molecular simulation. *Energy & Fuels*, 2019.

[40] M Mehana, MM Fahes, et al. Investigation of double layer expansion in low-salinity waterflooding: Molecular simulation study. In *SPE Western Regional Meeting*. Society of Petroleum Engineers, 2018.

[41] Multi-scale computational materials science laboratory. `https://sites.google.com/site/lingroupfsu/`. Accessed: 2018-02-23.

[42] Mike P Allen and Dominic J Tildesley. *Computer simulation of liquids*. Oxford university press, 1989.

[43] Adri CT Van Duin, Siddharth Dasgupta, Francois Lorant, and William A Goddard. Reaxff: a reactive force field for hydrocarbons. *The Journal of Physical Chemistry A*, 105(41):9396–9409, 2001.

[44] Thomas A Halgren and Wolfgang Damm. Polarizable force fields. *Current opinion in structural biology*, 11(2):236–242, 2001.

[45] Jay W Ponder, Chuanjie Wu, Pengyu Ren, Vijay S Pande, John D Chodera, Michael J Schnieders, Imran Haque, David L Mobley, Daniel S Lambrecht, Robert A DiStasio Jr, et al. Current status of the amoeba polarizable force field. *The journal of physical chemistry B*, 114(8):2549–2564, 2010.

[46] Marcus G Martin and J Ilja Siepmann. Transferable potentials for phase equilibria. 1. united-atom description of n-alkanes. *The Journal of Physical Chemistry B*, 102(14):2569–2577, 1998.

[47] Siepmann. Trappe.

[48] William L Jorgensen, David S Maxwell, and Julian Tirado-Rives. Development and testing of the opls all-atom force field on conformational energetics and properties of organic liquids. *Journal of the American Chemical Society*, 118(45):11225–11236, 1996.

[49] Chris Oostenbrink, Alessandra Villa, Alan E Mark, and Wilfred F Van Gunsteren. A biomolecular force field based on the free enthalpy of hydration and solvation: the gromos force-field parameter sets 53a5 and 53a6. *Journal of computational chemistry*, 25(13):1656–1676, 2004.

[50] Randall T Cygan, Jian-Jie Liang, and Andrey G Kalinichev. Molecular models of hydroxide, oxyhydroxide, and clay phases and the development of a general force field. *The Journal of Physical Chemistry B*, 108(4):1255–1266, 2004.

[51] Herman JC Berendsen, James PM Postma, Wilfred F van Gunsteren, and Jan Hermans. Interaction models for water in relation to protein hydration. In *Intermolecular forces*, pages 331–342. Springer, 1981.

[52] Pekka Mark and Lennart Nilsson. Structure and dynamics of the tip3p, spc, and spc/e water models at 298 k. *The Journal of Physical Chemistry A*, 105(43):9954–9960, 2001.

[53] Rebecca Notman and Jamshed Anwar. Breaching the skin barrierinsights from molecular simulation of model membranes. *Advanced drug delivery reviews*, 65(2):237–250, 2013.

[54] Denis J Evans and Brad Lee Holian. The nose–hoover thermostat. *The Journal of chemical physics*, 83(8):4069–4074, 1985.

[55] Herman JC Berendsen, JPM van Postma, Wilfred F van Gunsteren, ARHJ DiNola, and JR Haak. Molecular dynamics with coupling to an external bath. *The Journal of chemical physics*, 81(8):3684–3690, 1984.

[56] Michele Parrinello and Aneesur Rahman. Polymorphic transitions in single crystals: A new molecular dynamics method. *Journal of Applied physics*, 52(12):7182–7190, 1981.

[57] David Van Der Spoel, Erik Lindahl, Berk Hess, Gerrit Groenhof, Alan E Mark, and Herman JC Berendsen. Gromacs: fast, flexible, and free. *Journal of computational chemistry*, 26(16):1701–1718, 2005.

[58] Daan Frenkel and Berend Smit. *Understanding molecular simulation: from algorithms to applications*, volume 1. Elsevier, 2001.

[59] S. Bandyopadhyay S. Bhattacharyya B.L. Tembe, S. Gosavi and D. Maity. Chapter 26 molecular dynamics simulations. Report, 2016.

[60] Aiichiro Nakano. Methods of computational physics. Report.

[61] Steve Plimpton. Fast parallel algorithms for short-range molecular dynamics. *Journal of computational physics*, 117(1):1–19, 1995.

[62] Berk Hess, Carsten Kutzner, David Van Der Spoel, and Erik Lindahl. Gromacs 4: algorithms for highly efficient, load-balanced, and scalable molecular simulation. *Journal of chemical theory and computation*, 4(3):435–447, 2008.

[63] Marcus D Hanwell, Donald E Curtis, David C Lonie, Tim Vandermeersch, Eva Zurek, and Geoffrey R Hutchison. Avogadro: an advanced semantic chemical editor, visualization, and analysis platform. *Journal of cheminformatics*, 4(1):17, 2012.

[64] Alexander Stukowski. Visualization and analysis of atomistic simulation data with ovitothe open visualization tool. *Modelling and Simulation in Materials Science and Engineering*, 18(1):015012, 2009.

[65] William Humphrey, Andrew Dalke, and Klaus Schulten. Vmd: visual molecular dynamics. *Journal of molecular graphics*, 14(1):33–38, 1996.

[66] Molecular simulation/radial distribution functions. `https://en.wikibooks.org/wiki/Molecular_Simulation/Radial_Distribution_Functions`. Accessed: 2018-03-11.

[67] Natalia V Lisitza, Denise E Freed, Pabitra N Sen, and Yi-Qiao Song. Study of asphaltene nanoaggregation by nuclear magnetic resonance (nmr). *Energy & Fuels*, 23(3):1189–1193, 2009.

[68] Huang Zeng, Yi-Qiao Song, David L Johnson, and Oliver C Mullins. Critical nanoaggregate concentration of asphaltenes by direct-current (dc) electrical conductivity. *Energy & fuels*, 23(3):1201–1208, 2009.

[69] Jolle Eyssautier, Pierre Levitz, Didier Espinat, Jacques Jestin, Jrmie Gummel, Isabelle Grillo, and Loc Barr. Insight into asphaltene nanoaggregate structure inferred by small angle neutron and x-ray scattering. *The Journal of Physical Chemistry B*, 115(21):6827–6837, 2011.

[70] Michael P Hoepfner and H Scott Fogler. Multiscale scattering investigations of asphaltene cluster breakup, nanoaggregate dissociation, and molecular ordering. *Langmuir*, 29(49):15423–15432, 2013.

[71] Thomas F Headen, Edo S Boek, Jrg Stellbrink, and Ulrich M Scheven. Small angle neutron scattering (sans and v-sans) study of asphaltene aggregates in crude oil. *Langmuir*, 25(1):422–428, 2008.

[72] Jolle Eyssautier, Didier Frot, and Loc Barr. Structure and dynamic properties of colloidal asphaltene aggregates. *Langmuir*, 28(33):11997–12004, 2012.

[73] S Karaborni, NM Van Os, K Esselink, and PAJ Hilbers. Molecular dynamics simulations of oil solubilization in surfactant solutions. *Langmuir*, 9:1175–1175, 1993.

[74] Aldert R Van Buuren, Siewert-Jan Marrink, and Herman JC Berendsen. A molecular dynamics study of the decane/water interface. *Journal of Physical Chemistry*, 97:9206–9206, 1993.

[75] D Dumont and D Bougeard. A molecular dynamics study of hydrocarbons adsorbed in silicalite. *Zeolites*, 15(7):650–655, 1995.

[76] Philippe Ungerer, Anne Boutin, and Alain H Fuchs. Direct calculation of bubble points by monte carlo simulation. *Molecular Physics*, 97(4):523–539, 1999.

[77] Kent A Bowker. Barnett shale gas production, fort worth basin: issues and discussion. *AAPG bulletin*, 91(4):523–533, 2007.

[78] Zhongmin Wang and Alan Krupnick. A retrospective review of shale gas development in the united states: What led to the boom? 2013.

[79] Mohamed Mehana and Jeff Callard. Reserve estimation with unified production analysis. In *Unconventional Resources Technology Conference, Houston, Texas, 23-25 July 2018*, pages 691–696. Society of Exploration Geophysicists, American Association of Petroleum , 2018.

[80] Farzam Javadpour. Nanopores and apparent permeability of gas flow in mudrocks (shales and siltstone). *Journal of Canadian Petroleum Technology*, 48(08):16–21, 2009.

[81] Yueming Cheng. Impact of water dynamics in fractures on the performance of hydraulically fractured wells in gas-shale reservoirs. *Journal of Canadian Petroleum Technology*, 51(02):143–151, 2012.

[82] Zhehui Jin and Abbas Firoozabadi. Thermodynamic modeling of phase behavior in shale media. *SPE Journal*, 21(01):190–207, 2016.

[83] Bahareh Nojabaei, Russell T Johns, and Lifu Chu. Effect of capillary pressure on phase behavior in tight rocks and shales. *SPE Reservoir Evaluation & Engineering*, 16(03):281–289, 2013.

[84] Mohamed Mehana and Mashhad Fahes. The impact of the geochemical coupling on the fate of fracturing fluid, reservoir characteristics and early well performance in shale reservoirs. In *SPE Kingdom of Saudi Arabia Annual Technical Symposium and Exhibition*. Society of Petroleum Engineers.

[85] Mohamed Mehana, Mohamed AL Salman, and Mashhad Fahes. The impact of salinity on water dynamics, hydrocarbon recovery and formation softening in shale: Experimental study. In *SPE Kingdom of Saudi Arabia Annual Technical Symposium and Exhibition*. Society of Petroleum Engineers.

[86] Philippe Ungerer, Julien Collell, and Marianna Yiannourakou. Molecular modeling of the volumetric and thermodynamic properties of kerogen: Influence of organic type and maturity. *Energy & Fuels*, 29(1):91–105, 2014.

[87] Yinan Hu, Deepak Devegowda, Alberto Striolo, Anh Phan, Tuan A Ho, Faruk Civan, and Richard Sigal. The dynamics of hydraulic fracture water confined in nano-pores in shale reservoirs. *Journal of Unconventional Oil and Gas Resources*, 9:31–39, 2015.

[88] Shu Yang, Hassan Dehghanpour, Mojtaba Binazadeh, and Pingchuan Dong. A molecular dynamics explanation for fast imbibition of oil in organic tight rocks. *Fuel*, 190:409–419, 2017.

[89] Philippe Ungerer, Bernard Tavitian, and Anne Boutin. *Applications of molecular simulation in the oil and gas industry: Monte Carlo methods*. Editions Technip, 2005.

[90] P Ungerer, C Nieto-Draghi, V Lachet, A Wender, A Di Lella, A Boutin, B Rousseau, and Alain H Fuchs. Molecular simulation applied to fluid properties in the oil and gas industry. *Molecular Simulation*, 33(4-5):287–304, 2007.

[91] Johannes Diderik Van der Waals, Richard Threfall, John F Adair, and Friedrich Roth. *The continuity of the liquid and gaseous states*. publisher not identified, 1873.

[92] Abbas Firoozabadi. *Thermodynamics and Applications of Hydrocarbon Energy Production*. McGraw Hill Professional, 2015.

[93] Tereza Jindrov, Ji Mikyka, and Abbas Firoozabadi. Phase behavior modeling of bitumen and light normal alkanes and co2 by pr-eos and cpa-eos. *Energy & Fuels*, 30(1):515–525, 2015.

[94] Joachim Gross and Gabriele Sadowski. Perturbed-chain saft: An equation of state based on a perturbation theory for chain molecules. *Industrial and Engineering Chemistry Research*, 40(4):1244–1260, 2001.

[95] Joao AP Coutinho, Georgios M Kontogeorgis, and Erling H Stenby. Binary interaction parameters for nonpolar systems with cubic equations of state: a theoretical approach 1. co2/hydrocarbons using srk equation of state. *Fluid phase equilibria*, 102(1):31–60, 1994.

[96] Hassan Dashtian, Sahar Bakhshian, Sassan Hajirezaie, Jean-Philippe Nicot, and Seyyed Abolfazl Hosseini. Convection-diffusion-reaction of co2-enriched brine in porous media: A pore-scale study. *Computers & Geosciences*, 125:19–29, 2019.

[97] Mohamed Mehana, Jocin Abraham, and Mashhad Fahes. The impact of asphaltene deposition on fluid flow in sandstone. *Journal of Petroleum Science and Engineering*, 174:676–681, 2019.

[98] Wei Yu, HamidReza Lashgari, Kamy Sepehrnoori, et al. Simulation study of co2 huff-n-puff process in bakken tight oil reservoirs. In *SPE Western North American and rocky mountain joint meeting*. Society of Petroleum Engineers, 2014.

[99] Prasanna G Krishnamurthy, Siddharth Senthilnathan, Hongkyu Yoon, Daan Thomassen, Tip Meckel, and David DiCarlo. Comparison of darcy's law and invasion percolation simulations with buoyancy-driven co2-brine multiphase flow in a heterogeneous sandstone core. *Journal of Petroleum Science and Engineering*, 155:54–62, 2017.

[100] J. Johnston. Weeks island gravity stable co2 pilot. In *SPE Enhanced Oil Recovery Symposium*. Society of Petroleum Engineers.

[101] Mostafa Lashkarbolooki, Ahmad Vaezian, Ali Zeinolabedini Hezave, Shahab Ayatollahi, and Masoud Riazi. Experimental investigation of the influence of supercritical carbon dioxide and supercritical nitrogen injection on tertiary live-oil recovery. *The Journal of Supercritical Fluids*, 117:260–269, 2016.

[102] Abdulnour Y Toukmaji and John A Board. Ewald summation techniques in perspective: a survey. *Computer physics communications*, 95(2-3):73–92, 1996.

[103] William L Jorgensen, David S Maxwell, and Julian Tirado-Rives. Development and testing of the opls all-atom force field on conformational energetics and properties of organic liquids. *Journal of the American Chemical Society*, 118(45):11225–11236, 1996.

[104] Randall T Cygan, Vyacheslav N Romanov, and Evgeniy M Myshakin. Molecular simulation of carbon dioxide capture by montmorillonite using an accurate and flexible force field. *The Journal of Physical Chemistry C*, 116(24):13079–13091, 2012.

[105] Ding-Yu Peng and Donald B Robinson. A new two-constant equation of state. *Ind. Eng. Chem. Fundam*, 15(1):59–64, 1976.

[106] Hossein Nourozieh, Mohammad Kariznovi, and Jalal Abedi. Measurements and predictions of density and carbon dioxide solubility in binary mixtures of ethanol and n-decane. *The Journal of Chemical Thermodynamics*, 58:377–384, 2013.

[107] Juan M Milanesio, John C Hassler, and Erdogan Kiran. Volumetric properties of propane, n-octane, and their binary mixtures at high pressures. *Industrial & Engineering Chemistry Research*, 52(19):6592–6609, 2013.

[108] V Adrian Parsegian. *Van der Waals forces: a handbook for biologists, chemists, engineers, and physicists*. Cambridge University Press, 2005.

[109] Eduardo Buenrostro-Gonzalez, Henning Groenzin, Carlos Lira-Galeana, and Oliver C Mullins. The overriding chemical principles that define asphaltenes. *Energy & Fuels*, 15(4):972–978, 2001.

[110] Colin E Snape and Keith D Bartle. Definition of fossil fuel-derived asphaltenes in terms of average structural properties. *Fuel*, 63(7):883–887, 1984.

[111] Henning Groenzin and Oliver C Mullins. Molecular size and structure of asphaltenes from various sources. *Energy & Fuels*, 14(3):677–684, 2000.

[112] Oliver C Mullins and Eric Y Sheu. *Structures and dynamics of asphaltenes*. Springer Science & Business Media, 2013.

[113] Sophie Badre, Cristiane Carla Goncalves, Koyo Norinaga, Gale Gustavson, and Oliver C Mullins. Molecular size and weight of asphaltene and asphaltene solubility fractions from coals, crude oils and bitumen. *Fuel*, 85(1):1–11, 2006.

[114] Eric Y Sheu. Petroleum asphaltene properties, characterization, and issues. *Energy & Fuels*, 16(1):74–82, 2002.

[115] Philippe Ungerer, David Rigby, Benoit Leblanc, and Marianna Yiannourakou. Sensitivity of the aggregation behaviour of asphaltenes to molecular weight and structure using molecular dynamics. *Molecular Simulation*, 40(1-3):115–122, 2014.

[116] Tetyana Kuznicki, Jacob H Masliyah, and Subir Bhattacharjee. Aggregation and partitioning of model asphaltenes at toluene– water interfaces: Molecular dynamics simulations. *Energy & Fuels*, 23(10):5027–5035, 2009.

[117] F Gozalpour, SR Ren, and B Tohidi. Co2 eor and storage in oil reservoir. *Oil & gas science and technology*, 60(3):537–546, 2005.

[118] Shawket Ghedan. Global laboratory experience of co2-eor flooding. In *SPE/EAGE Reservoir Characterization & Simulation Conference*.

[119] Robert Michael Enick, David Kenneth Olsen, James Robert Ammer, and William Schuller. Mobility and conformance control for co2 eor via thickeners, foams, and gels–a literature review of 40 years of research and pilot tests. In *SPE improved oil recovery symposium*. Society of Petroleum Engineers.

[120] Eduardo Jose Manrique, Charles Philip Thomas, Ravi Ravikiran, Mehdi Izadi Kamouei, Michael Lantz, Jorge Luis Romero, and Vladimir Alvarado. Eor: current status and opportunities. In *SPE improved oil recovery symposium*. Society of Petroleum Engineers.

[121] Mohamed Mehana, Mashhad Fahes, and Liangliang Huang. System density of oil-gas mixtures: Insights from molecular simulations. In *SPE Annual Technical Conference and Exhibition*. Society of Petroleum Engineers.

[122] Mohamed Mehana, Mashhad Fahes, and Liangliang Huang. The density of oil/gas mixtures: Insights from molecular simulations. *SPE Journal*, 2018.

[123] Bei Liu and Berend Smit. Comparative molecular simulation study of co2/n2 and ch4/n2 separation in zeolites and metal– organic frameworks. *Langmuir*, 25(10):5918–5926, 2009.

[124] Ravichandar Babarao and Jianwen Jiang. Diffusion and separation of co2 and ch4 in silicalite, c168 schwarzite, and irmof-1: a comparative study from molecular dynamics simulation. *Langmuir*, 24(10):5474–5484, 2008.

[125] Youguo Yan, Zihan Dong, Yingnan Zhang, Pan Wang, Timing Fang, and Jun Zhang. Co2 activating hydrocarbon transport across nanopore throat: insights from molecular dynamics simulation. *Physical Chemistry Chemical Physics*, 2017.

[126] Doris L Gonzalez, Francisco M Vargas, George J Hirasaki, and Walter G Chapman. Modeling study of co2-induced asphaltene precipitation. *Energy & Fuels*, 22(2):757–762, 2007.

[127] Peyman Zanganeh, Shahab Ayatollahi, Abdolmohammad Alamdari, Ali Zolghadr, Hossein Dashti, and Shahin Kord. Asphaltene deposition during co2 injection and pressure depletion: A visual study. *Energy & Fuels*, 26(2):1412–1419, 2012.

[128] Sylvain Verdier, Herv Carrier, Simon I Andersen, and Jean-Luc Daridon. Study of pressure and temperature effects on asphaltene stability in presence of co2. *Energy & fuels*, 20(4):1584–1590, 2006.

[129] Taraneh Jafari Behbahani, Cyrus Ghotbi, Vahid Taghikhani, and Abbas Shahrabadi. Investigation on asphaltene deposition mechanisms during co2 flooding processes in porous media: a novel experimental study and a modified model based on multilayer theory for asphaltene adsorption. *Energy & Fuels*, 26(8):5080–5091, 2012.

[130] Taraneh Jafari Behbahani, Cyrus Ghotbi, Vahid Taghikhani, and Abbas Shahrabadi. Asphaltene deposition under dynamic conditions in porous media: theoretical and experimental investigation. *Energy & Fuels*, 27(2):622–639, 2013.

[131] Benmadi Milad and Roger Slatt. Impact of lithofacies variations and structural changes on natural fracture distributions. *Interpretation*, 6(4):T873–T887, 2018.

[132] Jocin James Abraham, Mohamed Mehana, and Mashhad Fahes. Investigating the uniformity of in-situ asphaltene deposits in sandstone rocks. In *SPE Europec featured at 80th EAGE Conference and Exhibition*. Society of Petroleum Engineers, 2018.

[133] RK Srivastava, SS Huang, and Mingzhe Dong. Asphaltene deposition during co2 flooding. *SPE production & facilities*, 14(04):235–245, 1999.

[134] Steve Soo-Khoon Sim, Komei Okatsu, Katsumo Takabayashi, and Douglas Blake Fisher. Asphaltene-induced formation damage: Effect of asphaltene particle size and core permeability. In *SPE Annual Technical Conference and Exhibition*. Society of Petroleum Engineers.

[135] Roland Tenjoh Okwen. Formation damage by co2 asphaltene precipitation. In *SPE International Symposium and Exhibition on Formation damage control*. Society of Petroleum Engineers.

[136] E Rogel. Molecular thermodynamic approach to the formation of mixed asphaltene– resin aggregates. *Energy & Fuels*, 22(6):3922–3929, 2008.

[137] Evan Lowry, Mohammad Sedghi, and Lamia Goual. Novel dispersant for formation damage prevention in co2: A molecular dynamics study. *Energy & Fuels*, 30(9):7187–7195, 2016.

[138] Jeramie J Adams. Asphaltene adsorption, a literature review. *Energy & Fuels*, 28(5):2831–2856, 2014.

[139] Olga Len, Eliasara Contreras, Estrella Rogel, Gilberto Dambakli, Scrates Acevedo, Lante Carbognani, and Joussef Espidel. Adsorption of native resins on asphaltene particles: a correlation between adsorption and activity. *Langmuir*, 18(13):5106–5112, 2002.

[140] Oliver C Mullins, Soraya S Betancourt, Myrt E Cribbs, Francois X Dubost, Jefferson L Creek, A Ballard Andrews, and Lalitha Venkataramanan. The colloidal structure of crude oil and the structure of oil reservoirs. *Energy & Fuels*, 21(5):2785–2794, 2007.

[141] Mohammad Sedghi and Lamia Goual. Role of resins on asphaltene stability. *Energy & Fuels*, 24(4):2275–2280, 2009.

[142] Y Bouhadda, D Bormann, E Sheu, D Bendedouch, A Krallafa, and M Daaou. Characterization of algerian hassi-messaoud asphaltene structure using raman spectrometry and x-ray diffraction. *Fuel*, 86(12-13):1855–1864, 2007.

[143] Teh Fu Yen, J Gordon Erdman, and Sidney S Pollack. Investigation of the structure of petroleum asphaltenes by x-ray diffraction. *Analytical chemistry*, 33(11):1587–1594, 1961.

[144] Mohammad Sedghi, Lamia Goual, William Welch, and Jan Kubelka. Effect of asphaltene structure on association and aggregation using molecular dynamics. *The Journal of Physical Chemistry B*, 117(18):5765–5776, 2013.

[145] Sander Pronk, Szilrd Pll, Roland Schulz, Per Larsson, Pr Bjelkmar, Rossen Apostolov, Michael R Shirts, Jeremy C Smith, Peter M Kasson, and David van der Spoel. Gromacs 4.5: a high-throughput and highly parallel open source molecular simulation toolkit. *Bioinformatics*, 29(7):845–854, 2013.

[146] Ulrich Essmann, Lalith Perera, Max L Berkowitz, Tom Darden, Hsing Lee, and Lee G Pedersen. A smooth particle mesh ewald method. *The Journal of chemical physics*, 103(19):8577–8593, 1995.

[147] Shuichi Nos. A unified formulation of the constant temperature molecular dynamics methods. *The Journal of chemical physics*, 81(1):511–519, 1984.

[148] Michele Parrinello and Aneesur Rahman. Polymorphic transitions in single crystals: A new molecular dynamics method. *Journal of Applied physics*, 52(12):7182–7190, 1981.

[149] Nathan Schmid, Andreas P Eichenberger, Alexandra Choutko, Sereina Riniker, Moritz Winger, Alan E Mark, and Wilfred F van Gunsteren. Definition and testing of the gromos force-field versions 54a7 and 54b7. *European biophysics journal*, 40(7):843, 2011.

[150] Lukas D Schuler, Xavier Daura, and Wilfred F Van Gunsteren. An improved gromos96 force field for aliphatic hydrocarbons in the condensed phase. *Journal of Computational Chemistry*, 22(11):1205–1218, 2001.

[151] Shirley WI Siu, Kristyna Pluhackova, and Rainer A Bckmann. Optimization of the opls-aa force field for long hydrocarbons. *Journal of Chemical Theory and Computation*, 8(4):1459–1470, 2012.

[152] Jiang Wang and Andrew L Ferguson. Mesoscale simulation of asphaltene aggregation. *The Journal of Physical Chemistry B*, 120(32):8016–8035, 2016.

[153] Alpeshkumar K Malde, Le Zuo, Matthew Breeze, Martin Stroet, David Poger, Pramod C Nair, Chris Oostenbrink, and Alan E Mark. An automated force field topology builder (atb) and repository: version 1.0. *Journal of chemical theory and computation*, 7(12):4026–4037, 2011.

[154] Michael P Allen and Dominic J Tildesley. *Computer simulation of liquids*. Oxford university press, 2017.

[155] M Uddin, D Coombe, and J Ivory. Molecular dynamics analysis of compositional effects in hydrocarbon systems property calculations. *Chemical Engineering Journal*, 302:503–515, 2016.

[156] Huang Zeng, Yi-Qiao Song, David L Johnson, and Oliver C Mullins. Critical nanoaggregate concentration of asphaltenes by direct-current (dc) electrical conductivity. *Energy & fuels*, 23(3):1201–1208, 2009.

[157] Simon I Andersen. Effect of precipitation temperature on the composition of n-heptane asphaltenes. *Fuel science & technology international*, 12(1):51–74, 1994.

[158] Paul Vledder, Ivan Ernesto Gonzalez, Julio Cesar Carrera Fonseca, Terence Wells, and Dick Jacob Ligthelm. Low salinity water flooding: proof of wettability alteration on a field wide scale. In *SPE Improved Oil Recovery Symposium*. Society of Petroleum Engineers.

[159] Tor Austad, Alireza RezaeiDoust, and Tina Puntervold. Chemical mechanism of low salinity water flooding in sandstone reservoirs. In *SPE improved oil recovery symposium*. Society of Petroleum Engineers.

[160] PL McGuire, JR Chatham, FK Paskvan, DM Sommer, and FH Carini. Low salinity oil recovery: An exciting new eor opportunity for alaska's north slope. In *SPE Western Regional Meeting*. Society of Petroleum Engineers.

[161] Adeel Zahid, Alexander A Shapiro, and Arne Skauge. Experimental studies of low salinity water flooding carbonate: A new promising approach. In *SPE EOR Conference at Oil and Gas West Asia*. Society of Petroleum Engineers.

[162] Mohamed Mehana and Ilham El-monier. Numerical investigation of the osmatic flow impact on the load recovery and early well performance. *Journal of Petroleum Engineering and Technology*, 5(03), 2015.

[163] Mohamed Mehana, Mohamed Alsalman, and Mashhad Fahes. The impact of salinity and mineralogy on slick water spontaneous imbibition and formation strength in shale. *Energy & Fuels*, 2018.

[164] Jim Seccombe, Arnaud Lager, Gary Jerauld, Bharat Jhaveri, Todd Buikema, Sierra Bassler, John Denis, Kevin Webb, Andrew Cockin, and Esther Fueg. Demonstration of low-salinity eor at interwell scale, endicott field, alaska. In *SPE Improved Oil Recovery Symposium*. Society of Petroleum Engineers.

[165] Kjetil Skrettingland, Torleif Holt, Medad T Tweheyo, and Ingun Skjevrak. Snorre low-salinity-water injection–coreflooding experiments and single-well field pilot. *SPE Reservoir Evaluation & Engineering*, 14(02):182–192, 2011.

[166] Hassan Mahani, Tibi Sorop, Dick Jacob Ligthelm, David Brooks, Paul Vledder, Fadwa Mozahem, and Younes Ali. Analysis of field responses to low-salinity waterflooding in secondary and tertiary mode in syria. In *SPE EUROPEC/EAGE Annual Conference and Exhibition*. Society of Petroleum Engineers.

[167] Dick Jacob Ligthelm, Jan Gronsveld, Jan Hofman, Niels Brussee, Fons Marcelis, and Hilbert van der Linde. Novel waterflooding strategy by manipulation of injection brine composition. In *EUROPEC/EAGE conference and exhibition*. Society of Petroleum Engineers.

[168] Ramez A Nasralla and Hisham A Nasr-El-Din. Double-layer expansion: is it a primary mechanism of improved oil recovery by low-salinity waterflooding? *SPE Reservoir Evaluation & Engineering*, 17(01):49–59, 2014.

[169] Matthew D Jackson, Dawoud Al-Mahrouqi, and Jan Vinogradov. Zeta potential in oil-water-carbonate systems and its impact on oil recovery during controlled salinity water-flooding. *Scientific reports*, 6:37363, 2016.

[170] David C Grahame. The electrical double layer and the theory of electrocapillarity. *Chemical reviews*, 41(3):441–501, 1947.

[171] Evert Johannes Willem Verwey, J Th G Overbeek, and Jan Theodoor Gerard Overbeek. *Theory of the stability of lyophobic colloids*. Courier Corporation, 1999.

[172] Pallab Ghosh. Dlvo theory and non-dlvo forces. *Nptel. ac. in*, pages 1–17, 2012.

[173] D Grasso, K Subramaniam, M Butkus, K Strevett, and J Bergendahl. A review of non-dlvo interactions in environmental colloidal systems. *Reviews in Environmental Science and Biotechnology*, 1(1):17–38, 2002.

[174] CJ Van Oss, RF Giese, and Patricia M Costanzo. Dlvo and non-dlvo interactions in hectorite. *Clays Clay Miner*, 38(2):151–159, 1990.

[175] Hongna Ding and Sheik Rahman. Experimental and theoretical study of wettability alteration during low salinity water flooding-an state of the art review. *Colloids and Surfaces A: Physicochemical and Engineering Aspects*, 520:622–639, 2017.

[176] GARRISON Sposito and DOMENICO Grasso. Electrical double layer structure, forces, and fields at the clay-water interface. *Surfactant science series*, pages 207–250, 1999.

[177] Joseph D McLean and Peter K Kilpatrick. Effects of asphaltene solvency on stability of water-in-crude-oil emulsions. *Journal of Colloid and Interface Science*, 189(2):242–253, 1997.

[178] Pat V Brady and Jim L Krumhansl. Surface complexation modeling for waterflooding of sandstones. *SPE Journal*, 18(02):214–218, 2013.

[179] Patrick V Brady, Norman R Morrow, Andrew Fogden, Vivianne Deniz, and Nina Loahardjo. Electrostatics and the low salinity effect in sandstone reservoirs. *Energy & Fuels*, 29(2):666–677, 2015.

[180] Quan Xie, Patrick V Brady, Ehsan Pooryousefy, Daiyu Zhou, Yongbing Liu, and Ali Saeedi. The low salinity effect at high temperatures. *Fuel*, 200:419–426, 2017.

[181] Yongqiang Chen, Quan Xie, Ahmad Sari, Patrick V Brady, and Ali Saeedi. Oil/water/rock wettability: Influencing factors and implications for low salinity water flooding in carbonate reservoirs. *Fuel*, 215:171–177, 2018.

[182] Hassan Mahani, Arsene Levy Keya, Steffen Berg, and Ramez Nasralla. The effect of salinity, rock type and ph on the electrokinetics of carbonate-brine interface and surface complexation modeling. In *SPE Reservoir Characterisation and Simulation Conference and Exhibition*. Society of Petroleum Engineers.

[183] Hassan Mahani, Arsene Levy Keya, Steffen Berg, and Ramez Nasralla. Electrokinetics of carbonate/brine interface in low-salinity waterflooding: effect of brine salinity, composition, rock type, and ph on ζ-potential and a surface-complexation model. *SPE Journal*, 22(01):53–68, 2017.

[184] Samuel Erzuah, Ingebret Fjelde, and Aruoture Voke Omekeh. Wettability estimation by surface complexation simulations. In *SPE Europec featured at 79th EAGE Conference and Exhibition*. Society of Petroleum Engineers.

[185] Aboulghasem Kazemi Nia Korrani, Wensi Fu, Alireza Sanaei, and Kamy Sepehrnoori. Mechanistic modeling of modified salinity waterflooding in carbonate reservoirs. In *SPE Annual Technical Conference and Exhibition*. Society of Petroleum Engineers.

[186] Jiazhong Wu, Fanghui Liu, Hui Yang, Shijing Xu, Quan Xie, Minghui Zhang, Ting Chen, Guangxin Hu, and Jinben Wang. Effect of specific functional groups on oil adhesion from mica substrate: Implications for low salinity effect. *Journal of Industrial and Engineering Chemistry*, 56:342–349, 2017.

[187] Ali A Yousef, Salah Hamad Al-Saleh, Abdulaziz Al-Kaabi, and Mohammed Saleh Al-Jawfi. Laboratory investigation of the impact of injection-water salinity and ionic content on oil recovery from carbonate reservoirs. *SPE Reservoir Evaluation & Engineering*, 14(05):578–593, 2011.

[188] Philip C Myint and Abbas Firoozabadi. Thermodynamics of flat thin liquid films. *AIChE Journal*, 61(9):3104–3115, 2015.

[189] Philip C Myint and Abbas Firoozabadi. Thermodynamics of flat thin wetting films with applications to low-salinity waterflooding. In *SPE Annual Technical Conference and Exhibition*. Society of Petroleum Engineers.

[190] Robert T Downs and Michelle Hall-Wallace. The american mineralogist crystal structure database. *American Mineralogist*, 88(1):247–250, 2003.

[191] Craig M Tenney and Randall T Cygan. Molecular simulation of carbon dioxide, brine, and clay mineral interactions and determination of contact angles. *Environmental science & technology*, 48(3):2035–2042, 2014.

[192] Randall T Cygan, Jian-Jie Liang, and Andrey G Kalinichev. Molecular models of hydroxide, oxyhydroxide, and clay phases and the development of a general force field. *The Journal of Physical Chemistry B*, 108(4):1255–1266, 2004.

[193] Biqiong Chen, Julian RG Evans, H Christopher Greenwell, Pascal Boulet, Peter V Coveney, Allen A Bowden, and Andrew Whiting. A critical appraisal of polymerclay nanocomposites. *Chemical Society Reviews*, 37(3):568–594, 2008.

[194] RL Anderson, I Ratcliffe, HC Greenwell, PA Williams, S Cliffe, and PV Coveney. Clay swellinga challenge in the oilfield. *Earth-Science Reviews*, 98(3):201–216, 2010.

[195] H Chris Greenwell, William Jones, Peter V Coveney, and Stephen Stackhouse. On the application of computer simulation techniques to anionic and cationic clays: A materials chemistry perspective. *Journal of Materials Chemistry*, 16(8):708–723, 2006.

[196] Benjamin Rotenberg, Virginie Marry, Rodolphe Vuilleumier, Natalie Malikova, Christian Simon, and Pierre Turq. Water and ions in clays: Unraveling the interlayer/micropore exchange using molecular dynamics. *Geochimica et Cosmochimica Acta*, 71(21):5089–5101, 2007.

[197] HJC Berendsen, JR Grigera, and TP Straatsma. The missing term in effective pair potentials. *Journal of Physical Chemistry*, 91(24):6269–6271, 1987.

[198] Steve Plimpton, Roy Pollock, and Mark Stevens. Particle-mesh ewald and rrespa for parallel molecular dynamics simulations. In *PPSC*.

[199] Eckhard Spohr. Molecular simulation of the electrochemical double layer. *Electrochimica Acta*, 44(11):1697–1705, 1999.

[200] Robert J Hunter. *Zeta potential in colloid science: principles and applications*, volume 2. Academic press, 2013.

[201] Milan Pedota, Michael L Machesky, and David J Wesolowski. Molecular origins of the zeta potential. *Langmuir*, 32(40):10189–10198, 2016.

[202] Susan Perkin, Ronit Goldberg, Liraz Chai, Nir Kampf, and Jacob Klein. Dynamic properties of confined hydration layers. *Faraday discussions*, 141:399–413, 2009.

[203] M Pedota, Peter T Cummings, and David J Wesolowski. Electric double layer at the rutile (110) surface. 3. inhomogeneous viscosity and diffusivity measurement by computer simulations. *The Journal of Physical Chemistry C*, 111(7):3071–3079, 2007.

[204] O Stern. *Electrochem*, 30(508), 1924.

[205] Z. Nagy. Colloid chemistry. in lecture 6.

[206] GJ Hirasaki. Wettability: fundamentals and surface forces. *SPE Formation Evaluation*, 6(02):217–226, 1991.

[207] Philip H Nelson. Pore-throat sizes in sandstones, tight sandstones, and shales. *AAPG bulletin*, 93(3):329–340, 2009.

[208] Tiziana Missana and Andrs Adell. On the applicability of dlvo theory to the prediction of clay colloids stability. *Journal of Colloid and Interface Science*, 230(1):150–156, 2000.

[209] Hans-Jrgen Butt. Measuring electrostatic, van der waals, and hydration forces in electrolyte solutions with an atomic force microscope. *Biophysical Journal*, 60(6):1438–1444, 1991.

[210] Gregor Cevc. Hydration force and the interfacial structure of the polar surface. *Journal of the Chemical Society, Faraday Transactions*, 87(17):2733–2739, 1991.

[211] Miroslav Colic, George V Franks, Matthew L Fisher, and Fred F Lange. Effect of counterion size on short range repulsive forces at high ionic strengths. *Langmuir*, 13(12):3129–3135, 1997.

[212] BW Ninham. On progress in forces since the dlvo theory. *Advances in Colloid and Interface Science*, 83(1-3):1–17, 1999.

[213] Evgenia V Lebedeva, Andrew Fogden, Tim J Senden, and Mark A Knackstedt. Kaolinite wettabilitythe effect of salinity, ph and calcium. *Society of Core Analysts*, 2010.

[214] J-L Bantignies, C Cartier Dit Moulin, and Herve Dexpert. Wettability contrasts in kaolinite and illite clays: characterization by infrared and x-ray absorption spectroscopies. *Le Journal de Physique IV*, 7(C2):C2–867–C2–869, 1997.

[215] Caili Dai, Kai Wang, Yifei Liu, Hui Li, Ziyang Wei, and Mingwei Zhao. Reutilization of fracturing flowback fluids in surfactant flooding for enhanced oil recovery. *Energy & Fuels*, 29(4):2304–2311, 2015.

[216] Yinghao Shen, Hongkui Ge, Mianmo Meng, Zhenxue Jiang, and Xinyu Yang. Effect of water imbibition on shale permeability and its influence on gas production. *Energy & Fuels*, 2017.

[217] Lin Hun, Zhang Shicheng, Wang Fei, Pan Ziqing, Mou Jianye, Zhou Tong, and Ren Zongxiao. Experimental investigation on imbibition-front progression in shale based on nuclear magnetic resonance. *Energy & Fuels*, 30(11):9097–9105, 2016.

[218] Fengpeng Lai, Zhiping Li, Qing Wei, Tiantian Zhang, and Qianhui Zhao. Experimental investigation of spontaneous imbibition in a tight reservoir with nuclear magnetic resonance testing. *Energy & Fuels*, 30(11):8932–8940, 2016.

[219] Yueming Cheng. Impact of water dynamics in fractures on the performance of hydraulically fractured wells in gas-shale reservoirs. *Journal of Canadian Petroleum Technology*, 51(02):143–151, 2012.

[220] Terry Engelder, Lawrence M Cathles, and L Taras Bryndzia. The fate of residual treatment water in gas shale. *Journal of Unconventional Oil and Gas Resources*, 7:33–48, 2014.

[221] Mojtaba Binazadeh, Mingxiang Xu, Ashkan Zolfaghari, and Hassan Dehghanpour. Effect of electrostatic interactions on water uptake of gas shales: the interplay of solution ionic strength and electrostatic double layer. *Energy & Fuels*, 30(2):992–1001, 2016.

[222] Aadish Gupta, Mingxiang Xu, Hassan Dehghanpour, and Doug Bearinger. Experimental investigation for microscale stimulation of shales by water imbibition during the shut-in periods. In *SPE Unconventional Resources Conference*. Society of Petroleum Engineers.

[223] Jianchao Cai, Edmund Perfect, Chu-Lin Cheng, and Xiangyun Hu. Generalized modeling of spontaneous imbibition based on hagenpoiseuille flow in tortuous capillaries with variably shaped apertures. *Langmuir*, 30(18):5142–5151, 2014.

[224] Mohamed Mehana and Ilham El-monier. Shale characteristics impact on nuclear magnetic resonance (nmr) fluid typing methods and correlations. *Petroleum*, 2(2):138–147, 2016.

[225] George Everette King. Thirty years of gas shale fracturing: What have we learned? In *SPE Annual Technical Conference and Exhibition*. Society of Petroleum Engineers.

[226] Perapon Fakcharoenphol, Mehmet Ali Torcuk, Jon Wallace, Antoine Bertoncello, Hossein Kazemi, Yu-Shu Wu, and Matt Honarpour. Managing shut-in time to enhance gas flow rate in hydraulic fractured shale reservoirs: a simulation study. In *SPE Annual Technical Conference and Exhibition*. Society of Petroleum Engineers.

[227] Kaiyrzhan Makhanov, Hassan Dehghanpour, and Ergun Kuru. An experimental study of spontaneous imbibition in horn river shales. In *SPE Canadian unconventional resources conference*. Society of Petroleum Engineers.

[228] H Dehghanpour, HA Zubair, A Chhabra, and A Ullah. Liquid intake of organic shales. *Energy & Fuels*, 26(9):5750–5758, 2012.

[229] H Dehghanpour, Q Lan, Y Saeed, H Fei, and Z Qi. Spontaneous imbibition of brine and oil in gas shales: effect of water adsorption and resulting microfractures. *Energy & Fuels*, 27(6):3039–3049, 2013.

[230] Qiyan Yan, Christina Lemanski, Zuleima T Karpyn, and LF Ayala. Experimental investigation of shale gas production impairment due to fracturing fluid migration during shut-in time. *Journal of Natural Gas Science and Engineering*, 24:99–105, 2015.

[231] Ola M Akrad, Jennifer Lynne Miskimins, and Manika Prasad. The effects of fracturing fluids on shale rock mechanical properties and proppant embedment. In *SPE Annual Technical Conference and Exhibition*. Society of Petroleum Engineers.

[232] Z Zhou, H Abass, X Li, D Bearinger, and W Frank. Mechanisms of imbibition during hydraulic fracturing in shale formations. *Journal of Petroleum Science and Engineering*, 141:125–132, 2016.

[233] H Roshan, S Ehsani, CE Marjo, MS Andersen, and RI Acworth. Mechanisms of water adsorption into partially saturated fractured shales: An experimental study. *Fuel*, 159:628–637, 2015.

[234] Duc Huu Le, Hai Nam Hoang, and Jagannathan Mahadevan. Impact of capillary suction on fracture face skin evolution in waterblocked wells. In *SPE Hydraulic Fracturing Technology Conference*. Society of Petroleum Engineers.

[235] Junjian Wang and Sheik S Rahman. An investigation of fluid leak-off due to osmotic and capillary effects and its impact on micro-fracture generation during hydraulic fracturing stimulation of gas shale. In *EUROPEC*. Society of Petroleum Engineers.

[236] Perapon Fakcharoenphol, Basak Kurtoglu, Hossein Kazemi, Sarinya Charoenwongsa, and Yu-Shu Wu. The effect of osmotic pressure on improve oil recovery from fractured shale formations. In *SPE unconventional resources conference*. Society of Petroleum Engineers.

[237] Mohamed Mehana. *On The Fate Of The Fracturing Fluid And Its Impact On Load Recovery And Well Performance*. Thesis, 2016.

[238] Xiaopeng Li, Hazim Abass, Tadesse W Teklu, and Qi Cui. A shale matrix imbibition model-interplay between capillary pressure and osmotic pressure. In *SPE Annual Technical Conference and Exhibition*. Society of Petroleum Engineers.

[239] Philip C Myint and Abbas Firoozabadi. Thin liquid films in improved oil recovery from low-salinity brine. *Current Opinion in Colloid & Interface Science*, 20(2):105–114, 2015.

[240] Asghar Gandomkar and Mohammad Reza Rahimpour. Investigation of low-salinity waterflooding in secondary and tertiary enhanced oil recovery in limestone reservoirs. *Energy & Fuels*, 29(12):7781–7792, 2015.

[241] Jiazhong Wu, Fanghui Liu, Gang Chen, Xu Wu, Desheng Ma, Qingjie Liu, Shijing Xu, Shizhe Huang, Ting Chen, and Wei Zhang. Effect of ionic strength on the interfacial forces between oil/brine/rock interfaces: A chemical force microscopy study. *Energy & Fuels*, 30(1):273–280, 2016.

[242] Lihu Zhang, Xiancai Lu, Xiandong Liu, Kan Yang, and Huiqun Zhou. Surface wettability of basal surfaces of clay minerals: insights from molecular dynamics simulation. *Energy & Fuels*, 30(1):149–160, 2016.

[243] Toms E Chvez-Miyauchi, Abbas Firoozabadi, and Gerald G Fuller. Nonmonotonic elasticity of the crude oilbrine interface in relation to improved oil recovery. *Langmuir*, 32(9):2192–2198, 2016.

[244] Seyma Aslan, Nariman Fathi Najafabadi, and Abbas Firoozabadi. Nonmonotonicity of the contact angle from nacl and mgcl2 concentrations in two petroleum fluids on atomistically smooth surfaces. *Energy & Fuels*, 30(4):2858–2864, 2016.

[245] MK Valluri, JO Alvarez, and DS Schechter. Study of the rock/fluid interactions of sodium and calcium brines with ultra-tight rock surfaces and their impact on improving oil recovery by spontaneous imbibition. In *SPE Low Perm Symposium*. Society of Petroleum Engineers.

[246] Ebrahim Ghanbari and Hassan Dehghanpour. Impact of rock fabric on water imbibition and salt diffusion in gas shales. *International Journal of Coal Geology*, 138:55–67, 2015.

[247] Matthew D Jackson, Dawoud Al-Mahrouqi, and Jan Vinogradov. Zeta potential in oil-water-carbonate systems and its impact on oil recovery during controlled salinity water-flooding. *Scientific reports*, 6:37363, 2016.

[248] Yinan Hu, Deepak Devegowda, Alberto Striolo, Anh Phan, Tuan A Ho, Faruk Civan, and Richard Sigal. The dynamics of hydraulic fracture water confined in nano-pores in shale reservoirs. *Journal of Unconventional Oil and Gas Resources*, 9:31–39, 2015.

[249] Shu Yang, Hassan Dehghanpour, Mojtaba Binazadeh, and Pingchuan Dong. A molecular dynamics explanation for fast imbibition of oil in organic tight rocks. *Fuel*, 190:409–419, 2017.

[250] Shaina Kelly. Experimental investigation of the influence of molecular surface interactions on imbibition in shale nano-pore proxies. In *SPE Annual Technical Conference and Exhibition*. Society of Petroleum Engineers.

[251] Qinhong Hu, Robert P Ewing, and Stefan Dultz. Low pore connectivity in natural rock. *Journal of contaminant hydrology*, 133:76–83, 2012.

[252] Hong-Kui Ge, Liu Yang, Ying-Hao Shen, Kai Ren, Fan-Bao Meng, Wen-Ming Ji, and Shan Wu. Experimental investigation of shale imbibition capacity and the factors influencing loss of hydraulic fracturing fluids. *Petroleum Science*, 12(4):636–650, 2015.

[253] JM Schembre and AR Kovscek. Estimation of dynamic relative permeability and capillary pressure from countercurrent imbibition experiments. *Transport in porous media*, 65(1):31–51, 2006.

[254] Dag Chun Standnes. Estimation of imbibition capillary pressure curves from spontaneous imbibition data. *Energy & Fuels*, 24(2):1081–1087, 2009.

[255] LL Handy. Determination of effective capillary pressures for porous media from imbibition data. *Trans., AIME*, 219:75, 1960.

[256] Olalekan Adisa Olafuyi, Yildiray Cinar, Mark Alexander Knackstedt, and Wolf Val Pinczewski. Spontaneous imbibition in small cores. In *Asia Pacific Oil and Gas Conference and Exhibition*. Society of Petroleum Engineers.

[257] Faruk Civan. *Reservoir formation damage*. Gulf Professional Publishing, 2015.

[258] RM Pashley and JP Quirk. The effect of cation valency on dlvo and hydration forces between macroscopic sheets of muscovite mica in relation to clay swelling. *Colloids and surfaces*, 9(1):1–17, 1984.

[259] Emiel JM Hensen and Berend Smit. Why clays swell. *The Journal of Physical Chemistry B*, 106(49):12664–12667, 2002.

[260] Xiaopeng Li*, Tadesse W Teklu, Hazim Abass, and Qi Cui. The impact of water salinity/surfactant on spontaneous imbibition through capillarity and osmosis for unconventional ior. In *Unconventional Resources Technology Conference, San Antonio, Texas, 2016*, pages 3058–3076. Society of Exploration Geophysicists, American Association of Petroleum Geologists, Society of Petroleum Engineers.

[261] Chao Fang and Rui Qiao. Surface hydration drives rapid water imbibition into strongly hydrophilic nanopores. *Physical Chemistry Chemical Physics*, 2017.

[262] Patrick V Brady and Geoffrey Thyne. Functional wettability in carbonate reservoirs. *Energy & Fuels*, 30(11):9217–9225, 2016.

[263] Achinta Bera, Keka Ojha, T Kumar, and Ajay Mandal. Mechanistic study of wettability alteration of quartz surface induced by nonionic surfactants and interaction between crude oil and quartz in the presence of sodium chloride salt. *Energy & Fuels*, 26(6):3634–3643, 2012.

[264] Junjing Zhang, Ding Zhu, and Alfred Daniel Hill. Water-induced fracture conductivity damage in shale formations. In *SPE Hydraulic Fracturing Technology Conference*. Society of Petroleum Engineers.

[265] Shuhua Lin and Bitao Lai. Experimental investigation of water saturation effects on barnett shale's geomechanical behaviors. In *SPE Annual Technical Conference and Exhibition*. Society of Petroleum Engineers.

[266] Junjing Zhang. Fracture conductivity damage by water in shale formations. In *SPE Annual Technical Conference and Exhibition*. Society of Petroleum Engineers.

[267] Qiao Lyu, Pathegama Gamage Ranjith, Xinping Long, and Bin Ji. Experimental investigation of mechanical properties of black shales after co2-water-rock interaction. *Materials*, 9(8):663, 2016.

[268] MO Denekas, CC Mattax, and GT Davis. Effects of crude oil components on rock wettability. *Society of Petroleum Engineers Journal*, 1959.

[269] Henning Groenzin, Oliver C. Mullins, Semih Eser, Jonathan Mathews, Ming-Gang Yang, and Daniel Jones. Molecular size of asphaltene solubility fractions. *Energy & Fuels*, 17(2):498–503, 2003.

[270] Otto P Strausz, Thomas W Mojelsky, and Elizabeth M Lown. The molecular structure of asphaltene: an unfolding story. *Fuel*, 71(12):1355–1363, 1992.

[271] Eduardo Buenrostro-Gonzalez, Henning Groenzin, Carlos Lira-Galeana, and Oliver C. Mullins. The overriding chemical principles that define asphaltenes. *Energy & Fuels*, 15(4):972–978, 2001.

[272] David L Mitchell and James G Speight. The solubility of asphaltenes in hydrocarbon solvents. *Fuel*, 52(2):149–152, 1973.

[273] James G Speight, Robert B Long, and Theodore D Trowbridge. Factors influencing the separation of asphaltenes from heavy petroleum feedstocks. *Fuel*, 63(5):616–620, 1984.

[274] James G Speight, Robert B Long, Theodore D Trowbridge, and N Linden. On the definition of asphaltenes. *Am. Chem. Soc., Div. Pet. Chem., Prepr*, 27(3):268–275, 1982.

[275] Jinhyung Cho, Tae Hong Kim, and Kun Sang Lee. Compositional modeling of hybrid co 2 eor with intermediate hydrocarbon solvents to analyze the effect of toluene on asphaltene deposition. *Journal of Petroleum Science and Engineering*, 146:940–948, 2016.

[276] KJ Leontaritis and GA Mansoori. Asphaltene flocculation during oil production and processing: A thermodynamic collodial model. In *SPE International Symposium on Oilfield Chemistry*. Society of Petroleum Engineers.

[277] I Kocabas. Characterization of asphaltene precipitation effect on reducing carbonate rock permeability. In *Middle East Oil Show*. Society of Petroleum Engineers.

[278] Abdulrazag Y. Zekri and Shedid Ali Shedid. The effect of fracture characteristics on reduction of permeability by asphaltene precipitation in carbonate formation. *Journal of Petroleum Science and Engineering*, 42(2):171–182, 2004.

[279] Shedid A. Shedid. An ultrasonic irradiation technique for treatment of asphaltene deposition. *Journal of Petroleum Science and Engineering*, 42(1):57–70, 2004.

[280] L Minssieux. Core damage from crude asphaltene deposition. In *International Symposium on Oilfield Chemistry*. Society of Petroleum Engineers.

[281] Aly Hamouda and Omid Karoussi. Effect of temperature, wettability and relative permeability on oil recovery from oil-wet chalk. *Energies*, 1(1):19–34, 2008.

[282] Taraneh Jafari Behbahani, Cyrus Ghotbi, Vahid Taghikhani, and Abbas Shahrabadi. Asphaltene deposition under dynamic conditions in porous media: theoretical and experimental investigation. *Energy & Fuels*, 27(2):622–639, 2013.

[283] Shahin Kord, Rohaldin Miri, Shahab Ayatollahi, and Mehdi Escrochi. Asphaltene deposition in carbonate rocks: experimental investigation and numerical simulation. *Energy & Fuels*, 26(10):6186–6199, 2012.

[284] Reyadh A. Almehaideb. Asphaltene precipitation and deposition in the near wellbore region: a modeling approach. *Journal of Petroleum Science and Engineering*, 42(2-4):157–170, 2004.

[285] M. Shirdel, D. Paes, P. Ribeiro, and K. Sepehrnoori. Evaluation and comparison of different models for asphaltene particle deposition in flow streams. *Journal of Petroleum Science and Engineering*, 84-85:57–71, 2012.

[286] Saeedeh Mohebbinia, Kamy Sepehrnoori, Russell T. Johns, and Aboulghasem Kazemi Nia Korrani. Simulation of asphaltene precipitation during gas injection using pc-saft eos. *Journal of Petroleum Science and Engineering*, 158:693–706, 2017.

[287] Hamid Reza Ansari and Amin Gholami. Robust method based on optimized support vector regression for modeling of asphaltene precipitation. *Journal of Petroleum Science and Engineering*, 135:201–205, 2015.

[288] M. Haghshenasfard and K. Hooman. Cfd modeling of asphaltene deposition rate from crude oil. *Journal of Petroleum Science and Engineering*, 128:24–32, 2015.

[289] Hadi Seyyedbagheri and Behruz Mirzayi. Cfd modeling of high inertia asphaltene aggregates deposition in 3d turbulent oil production wells. *Journal of Petroleum Science and Engineering*, 150:257–264, 2017.

[290] Salah Yaseen and G Ali Mansoori. Molecular dynamics studies of interaction between asphaltenes and solvents. *Journal of Petroleum Science and Engineering*, 2017.

[291] William G Anderson. Wettability literature survey-part 1: rock/oil/brine interactions and the effects of core handling on wettability. *Journal of petroleum technology*, 38(10):1,125–1,144, 1986.

[292] William G Anderson. Wettability literature survey part 5: the effects of wettability on relative permeability. *Journal of Petroleum Technology*, 39(11):1,453–1,468, 1987.

[293] Rashid SH Al-Maamari and Jill S Buckley. Asphaltene precipitation and alteration of wetting: Can wettability change during oil production? In *SPE/DOE Improved Oil Recovery Symposium*. Society of Petroleum Engineers.

[294] Takaaki Uetani. Wettability alteration by asphaltene deposition: A field example. In *Abu Dhabi International Petroleum Exhibition and Conference*. Society of Petroleum Engineers.

[295] B Mirzayi, M Vafaie-Sefti, SA Mousavi-Dehghani, M Fasih, and GA Mansoori. The effects of asphaltene deposition on unconsolidated porous media properties during miscible natural gas flooding. *Petroleum Science and Technology*, 26(2):231–243, 2008.

[296] JM Wolcott, F Groves, and H Lee. The influence of crude-oil composition on mineral adsorption and wettability adsorption. *SPE*, page 25194, 1996.

[297] V Hematfar, BB Maini, and Z Chen. Experimental investigation of the impact of asphaltene adsorption on two phase flow in porous media. In *SPE European Formation Damage Conference & Exhibition*. Society of Petroleum Engineers.

[298] Shedid A Shedid. Influences of asphaltene precipitation on capillary pressure and pore size distribution of carbonate reservoirs. *Petroleum science and technology*, 19(5-6):503–519, 2001.

[299] Zarrin Nasri and Bahram Dabir. Effects of asphaltene deposition on oil reservoir characteristics including two-phase flow. *Journal of the Japan Petroleum Institute*, 52(1):1–9, 2009.

[300] Lamia Goual and Abbas Firoozabadi. Effect of resins and dbsa on asphaltene precipitation from petroleum fluids. *AIChE journal*, 50(2):470–479, 2004.

[301] Mohamed Mehana, Mashhad Fahes, et al. On the pressure response during unsteady state fluid displacement experiments. In *Abu Dhabi International Petroleum Exhibition & Conference*. Society of Petroleum Engineers, 2018.